学位論文

Experimental Search for Hidden-Photon Cold Dark Matter Signatures in the $O(10)$ keV mass range with XMASS-I

(XMASS-I検出器を用いた数10 keV質量領域の
hidden-photon cold dark matterの探索)

平成28年1月博士（理学）申請
東京大学大学院理学系研究科
物理学専攻
高知尾　理

Abstract

A search for hidden-photon cold dark-matters (HPDMs) in the mass region between 50 keV_{ee} and 120 keV_{ee} was performed by XMASS-I liquid xenon scintillation detector. A hidden-photon can interact with an electron in the liquid xenon in an analogous fashion to photoelectric effect thorough kinetic mixing and deposit the energy corresponding to its rest mass. XMASS detector was designed to search nuclear recoil signals with Weakly interacting massive particles (WIMPs) but also has high sensitivity for electron recoil signals with hidden-photons. After some background reduction, we achieved a lower background at a level of 5×10^{-4} $kg^{-1}day^{-1}keV_{ee}{}^{-1}$ while a signal efficiency of the signal MC of 80 keV/c^2 hidden-photon was 99.3% using 252.9 days and 327.8 kg fiducial volume data. Since we found no significant excess, we set an upper limit on the kinetic mixing with $\kappa < 1.7\times10^{-13}$ for the mass of 80 keV/c^2 at 90% confidence level. This value is more than two times better than the previous result by the data taken by the XMASS commissioning phase and the most stringent in the direct detection experiments to date.

Acknowledgements

I would like to express my great appreciation to my supervisor, Professor Yasuhiro Kishimoto for guiding and encouraging me throughout my graduate cource.
I would like to express my gratitude to Prof. Y. Suzuki, the spokesperson of the XMASS experiment, for introducing me to XMASS experiment.
I would like to express my gratitude to Prof. S.Moriyama. He has guided me in many occasions. I learned many things related to physics and experiments from him.
I would thank to XMASS collaboration who worked with me, K.Abe, K.Hiraide, K.Ichimura, K.Kobayashi, M.Kobayashi, Prof. M.Nakahata, T.Norita, H.Ogawa, K.Sato, H.Sekiya, A.Takeda, Prof. M.Yamashita, B.S.Ynag, N.Y.Kim, Y.D.Kim, Prof. S. Tasaka, Prof. K.Fushimi, G.Kanzaki, J.Liu, Prof. K.Martens, B.D.Xu, R.Fujita, K.Hosokawa, Prof. K.Miuchi, Y.Onishi, N.Oka, Prof. Y.Takeuchi, Prof. Y.H.Kim, J.S.Lee, K.B.Lee, M.K.Lee, Prof. Y.Fukuda, Prof. Y.Itow, R.Kegasa, K.Kobayashi, K.Kanzawa, Prof. K.Masuda, H.Takiya, Prof. Nishijima, M.Miyasaka, and Prof. S.Nakamura.
I am also deeply appreciate to my friends who supported me all the time, R.Akutsu, Y.Nakano, Y.Okajima, A.Ori, Y.Sonoda, Y.Suda, and other many students.
I would like to extend my gratitude to all the people who supported and encouraged me during my time in graduated school. Finally, I wish to express my deep gratitude to my family.

Contents

Chapter 1

Introduction

Many gravitational observations indicate the presence of dark matter in the universe. The latest result of the Planck satellite indicates 68.3% dark energy, 26.8% dark matter, and 4.9% ordinary matter as the mass energy components of the universe [1]. On the other hand, the introduction of new particles in order to compensate the incompleteness of standard model of elementary particles may solve the both of the problems of dark matter and the standard model. Many kinds of theories have been proposed and a lot of observations and experiments have been designed and implemented. Nevertheless, dark matter has not be directly observed so far. Dark matter is one of the most important and attractive topics in physics today.

The most motivating candidate for dark matter is Weakly Interactive Massive Particles (WIMPs). The WIMPs form a class of heavy particles (GeV-TeV) and interact slightly with matters. The one attractive candidate is neutralino expected from super symmetric extensions of the standard model. A lot of experiments were proposed to detect a signal of nuclear recoil of target nucleus with WIMPs and many efforts to increase the sensitivity have been devoted in the past.

Although not change the fact that WIMPs are the most attractive solution, we always need to imagine the other possibilities because the nature of dark matter is unknown and still not detected. Weakly Interactive Slim Particles (WISPs) is another motivating candidates. WISPs is basically lighter than WIMPs and axion and hidden-photon belong to this class. These particles can be coupled to photon with kinetic mixing, and we have possibilities to detect them by detection of photo-electric like effects or converted photons.

We focused on "hidden-photon dark matters (HPDMs)" in this thesis. Although the possibility of thermally produced hidden-photons in the early universe consisting the dark matter is almost rejected [2], HPDMs can also be generated non-thermally in the condensate after the inflation like axion case (vacuum misalignment mechanism). This process is generating a lot of attention recently.

XMASS experiment was in origin launched to detect WIMPs [3]. We are now trying to increase the sensitivity for the original purpose. Meanwhile, XMASS detector also have high sensitivity to electron recoil signals. The background level of electron recoils from several tens of keV to several hundreds of keV in the fiducial volume is the lowest in the world. We are planning to enlarge the detector in the near future. This means the XMASS detector have possibilities to achieve distinction especially in the physics of this energy range. We take advantage of this feature to search for electron recoil signals by HPDMs with high sensitivity. These are the motivations for this thesis.

In this thesis, we introduce some popular dark matter models and some representative experiments in Chap. 2, and explain about hidden-photons and hidden-photon dark matter theory in Chap. 3 and Chap. 4, respectively. How to search for HPDMs by using axio-electric effect is described in Chap.5. An overview of the XMASS experiment is in Chap. 6, a summary of the detector calibration is in Chap. 7, our well-understood backgrounds for the HPDM search are described in Chap. 8, and a detector refurbishment implemented from May 2013 to Nov. 2014 to reduce the backgrounds is shortly explained in Chap. 9. The analysis for HPDMs using data taken by the XMASS detector after the refurbishment is explained in Chap. 10. Finally, the result and discussion are described in Chap.11, and the conclusion of this thesis is summarized in Chap. 12.

Chapter 2

Dark Matter

2.1 Evidence for dark matter

There is persuasive evidence for the existence of dark matter in the Universe. The first prediction of the existence of dark matter was come from the observation of the Coma Clusters conducted by Fritz Zwicky *et al.* in 1933 [4]. They suggested that the galaxies of the clusters have too large velocity dispersion for the cluster to be bound together by only the visible matters. In 1970s, the problem appeared again from the measurement of galactic rotation curves by Vera Rubin [5]. One of the recent result is come from the observation of the rotation curve for the spiral galaxy NGC6503 [6]. The rotational velocity v of an object on a stable Keplerian orbit with radius r around a galaxy scales like

$$v(r) = \sqrt{G\frac{M(r)}{r}}, \tag{2.1}$$

where G is the gravitational constant, r is the radial distance from the center of the galaxy, and $M(r)$ is the total mass within the radius r. The luminous matters are aggregated in about 5 kpc from the center of the galaxy. If $M(r)$ is nearly constant at further than 5 kpc, the rotational velocity should drop at large r. However, the velocity stays flat even outside the luminescent matters. The rotation curve for NGC6503 is shown in Fig. 2.1.

The abundance of dark matter in our universe is estimated by the fluctuations of cosmic microwave background (CMB). The spectrum of temperature fluctuations in CMB depends on the baryon density ($\Omega_b h^2$) , the cold dark matter density ($\Omega_{DM} h^2$) of the universe, and the other cosmological parameters. The baryon density and the cold dark matter density can be determined by fitting for the observed data of temperature fluctuations. The latest observational data of Planck satellite [7] indicates $\Omega_b h^2 = 0.022068 \pm 0.001$ and $\Omega_{DM} h^2 = 0.12029 \pm 0.001$ for the best fit, where h is the hubble constant divided by 100 $\mathrm{kms}^{-1}\mathrm{Mpc}^{-1}$, $h = 0.67$ for the best fit.

For detection and understanding of dark matter, it is also important to know the density of dark matter around the earth. The local halo density ρ_0 and dark matter velocity distribution v_0 are needed to calculate the event rate of dark matter detection with a detector. ρ_0 and v_0 can be estimated by the rotation curve of our Galaxy in a isothermal halo model. Assuming that our galaxy is an ordinary spiral galaxy like NGC6503, the rotation velocity of our galaxy increases linearly from the center and become roughly 220 km/s in the solar neighborhood and remains roughly flat all the

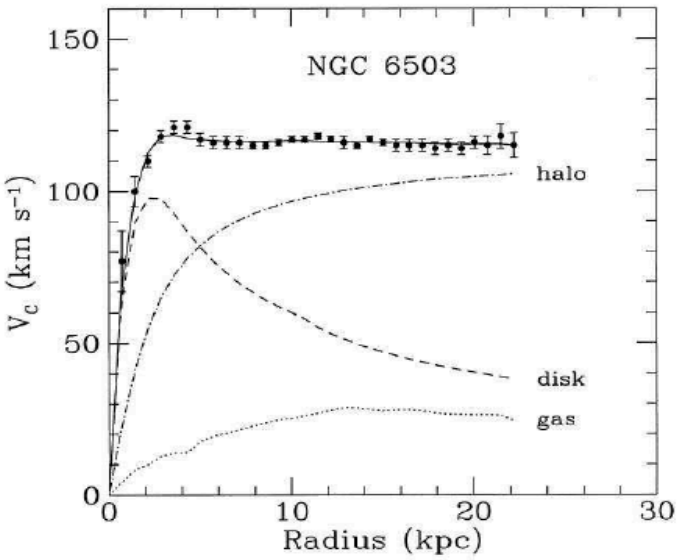

Figure 2.1: Galactic rotation curve for NGC6503. The points with error bars indicate the measured rotation velocity as a function of distance from the galactic center. The figure shows the dark matter halo contribution is needed to match the data in addition to the disk and gas contribution [6].

way out to 25 kpc [8]. The rotation curve for our Galaxy is shown in Fig. 2.2. The density distribution of dark matter can be described as

$$\rho(r) = \frac{\rho_0}{1 + r^2/r_0^2}, \tag{2.2}$$

if the isothermal halo model is assumed, where, ρ_0 and v_0 are fitting parameters. Using the observed rotation velocity around the sun, the density of dark matter can be estimated that [9]

$$\rho_0 \sim 0.3 \text{ GeVc}^{-2}\text{cm}^{-3}, \tag{2.3}$$

with an uncertainty of factor two. Recently N-body simulations derived somewhat higher local density, e.g. $\rho_0 = 0.39$ GeVc^{-2}cm^{-3} [10] and $\rho_0 = 0.37$ GeVc^{-2}cm^{-3} [11]. However, more conventional value 0.3 GeVc^{-2}cm^{-3} was used in this thesis.

2.2 Candidates for dark matter

Dark matter needs to satisfy some conditions. 1) Dark matter needs to be sufficiently stable state on cosmological timescale in order to be present in the present universe. 2) Dark matter should interact sufficiently weakly with baryonic matter and radiation. 3) The relic abundance should be consistent with our universe.

Neutrinos might be only subdominant dark matter candidate, $\Omega h^2 < 0.0062$ [12]. Besides, while the analyses of structure formation in the universe suggest "cool" or "cold" dark matter is preferred, neutrinos are relativistic particles (hot dark-matter) and inconsistent with the results. MAssive Compact Halo Object (MACHO) is a general name for non-luminescent astronomical body, such as brown dwarf, neutron star,

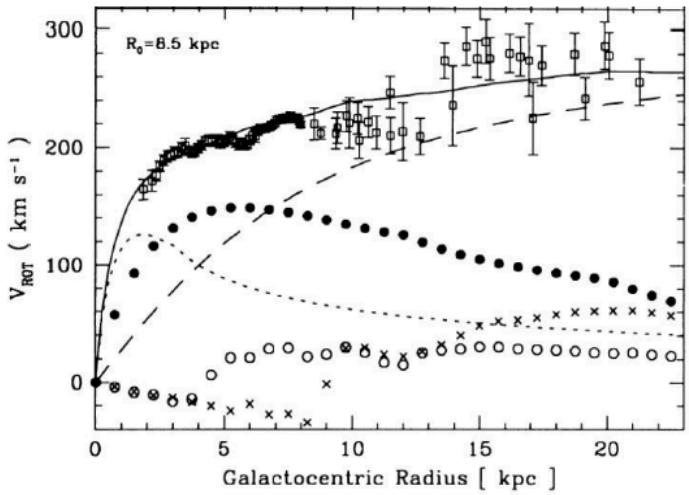

Figure 2.2: Rotation curve for our Galaxy adopted from [8]. The each line represents the contribution from the bulge (dotted), the disk (filled circles), the HI layer (crosses), the H_2 layer (circles), and from the dark halo (dashed). The solid line represents the sum of the contributions.

black hole, and was one of the dark matter candidates. However, the observation by gravitational lens showed MACHO can not explain the major part of dark matter [13]. If dark matter is constituted by elementary particles, it is very important whether the dark matter particles were produced thermally or non-thermally. Because thermal relics and non-thermal relics have a different relationship between their relic abundance Ω and their properties such as mass and couplings. Of course, the method to detect the particles should be adapted to the relationships. A representative candidate for the thermally produced dark matter is Weakly Interactive Massive Particles (WIMPs), and a candidate for the non-thermally produced dark matter is axions and hidden-photons.

For the thermally produced dark matter, the thermal relic is assumed to be in local thermodynamic equilibrium in the early universe. If we define the variables $Y \equiv n_\chi/s$ and $x = M_\chi/T$, where n_χ is the number density of WIMPs, s is the entropy density, M_χ is the mass of the WIMPs, and T is the temperature,

$$\begin{aligned} Y &\sim constant \qquad (x \ll 1) \\ Y &\propto exp(-x) \qquad (x \gg 1). \end{aligned} \tag{2.4}$$

As long as the interaction rate (Γ) is larger than the expansion rate of the universe (H), a particle tracks its equilibrium abundance. When the expansion rate exceeds the interaction rate ($H > \Gamma$), the number density of the particles in the universe (Y) becomes constant value (thermal freeze out).

2.2.1 WIMPs of neutralino

WIMPs might be created thermally and the mass is approximately between 10 GeV and 1 TeV and the coupling size is similar to the weak interaction. The most convincing candidate for WIMPs is Lightest Supersymmetric Particle (LSP) with R-parity

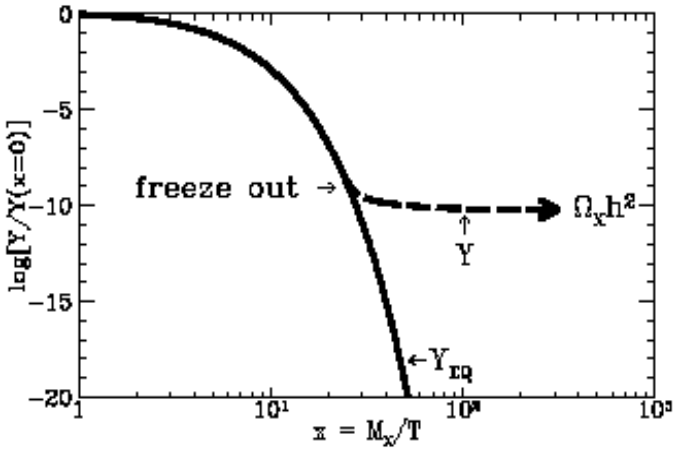

Figure 2.3: Freeze out process of thermally produced dark-matter. This figure was adopted from [14].

expected from the supersymmetric theory, which is extension of the standard model. The LSP is stable in the models with R-parity conservation. From a constraint that dark matter must be electrically natural and non-colored, the LSP could be the lightest neutralino, the gravitino, or the lightest sneutrino. Sneutrino dark matter is ruled out in the Minimal Supersymmetric Standard Model (MSSM) by direct detection experiments. Gravitino dark matter is the fermion supersymmetric partner to the graviton and a candidate whose scale of supersymmetric breaking is low ($\sim$ 100 TeV). Gravitino is very light ($\sim$ eV) and have very weak interaction rate. It is almost impossible to directly detect gravitino for this reason. Additionally, the relic abundance of gravitino dark matter is too small assuming that they were produced thermally from the thermal bath in the early universe. Neutralino dark matter is a linear combination of photino ($\tilde{\gamma}$), zino($\tilde{Z}$), and higgsinos($\tilde{H^0_{u1}}, \tilde{H^0_{d2}}$). The photino and zino can be described as

$$\begin{aligned} \tilde{\gamma} &= con\theta_W \tilde{B} + sin\theta_W \tilde{W}_3 \\ \tilde{\mathrm{Z}} &= -sin\theta_W \tilde{B} + cos\theta_W \tilde{W}_3. \end{aligned} \tag{2.5}$$

$\tilde{B}$ and $\tilde{W}_3$ are fermion supersymmetric partners of gauge bosons. So the neutralino($\tilde{\chi^0_n}$) can be described as

$$\tilde{\chi^0_n} = N_1\tilde{B} + N_2\tilde{W}_3 + N_3\tilde{H^0_{u1}} + N_4\tilde{H^0_{d2}}. \tag{2.6}$$

Magnitudes of N_1,N_2,N_3, and N_4 decide on nature of neutralinos. The lightest neutralino in the four neutralinos are a good candidate for dark matter because they can explain the present thermal relic in a good accuracy.

Detection methods for WIMPs

Detection methods for WIMPs can be divided into indirect detections and direct ones. The former include an observation of decay products of dark matter and annihilations, and the later usually means an observation of recoiled nuclei by dark matter in a terrestrial experiment. Elastic scattering and inelastic scattering can be considered. Spin-independent(SI) and spin-dependent(SD) interactions are possible. There are many kind of experiments in the world today.

Figure 2.4 shows the present sensitivity for the cross sections of WIMP-nucleon scattering (SI). Some explanations for each of the constraints are illustrated below.

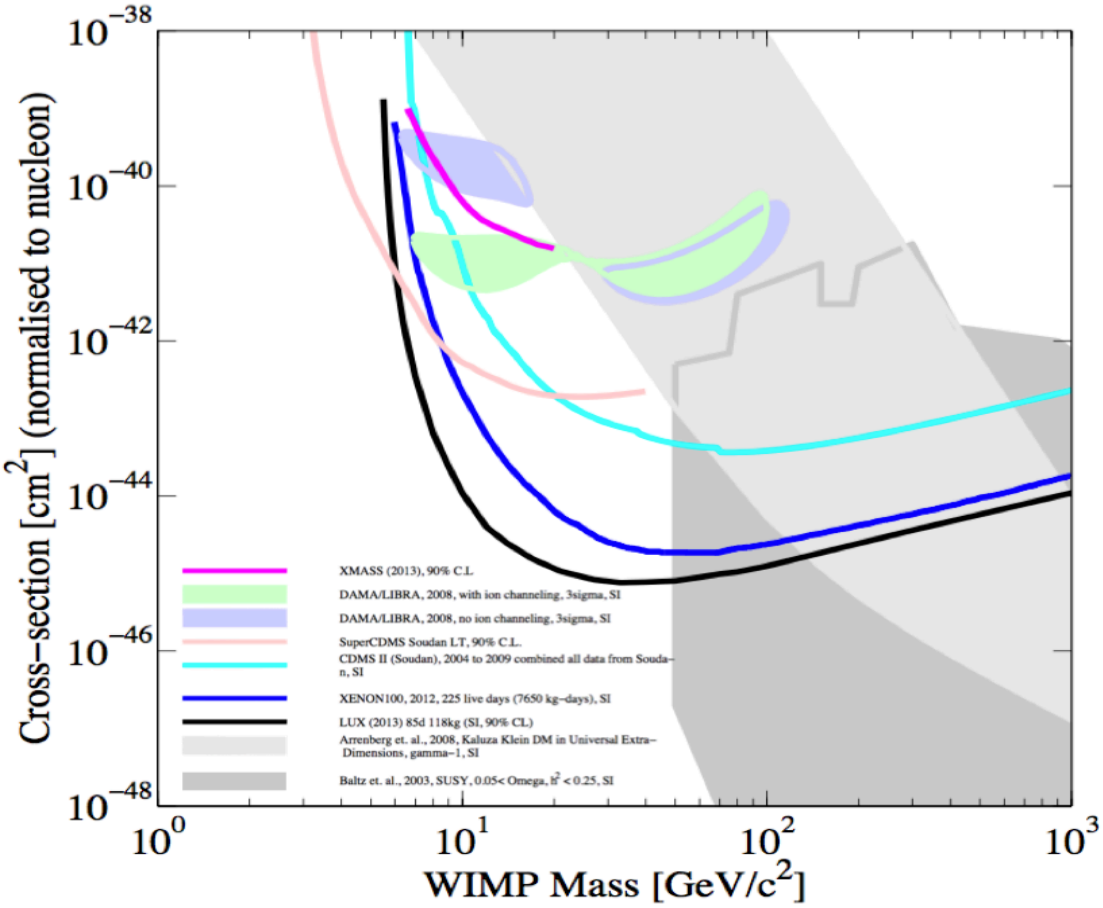

Figure 2.4: Upper limit on the spin independent cross section. The allowed region at 3 σ by DAMA and the upper limits by CDMSII, XENON100, and LUX. The results of low mass WIMPs search by XMASS and superCDMS are also shown. This figure was generated by "Dark Matter Limit Plot Generator [15]".

DAMA/LIBLA

DAMA/LIBLA group in the I.N.F.N. in Italy used 233 kg NaI and implemented an observation of dark matter. They achieved 2 keV threshold and continued 13 years physical run. Total exposure was 1.17 ton·year. They reported the annual modulation of the signals is 8.9 σ assuming an independent halo model. The modulation amplitude is 0.0116+/-0.0013 cpd/kg/day in the (2 - 6) keV energy. The measured phase and period is 146+/-7 days and 0.999+/-0.002 year, respectively [16]. However some more sensitive experiments such as LUX and XENON have never reproduced the results so far.

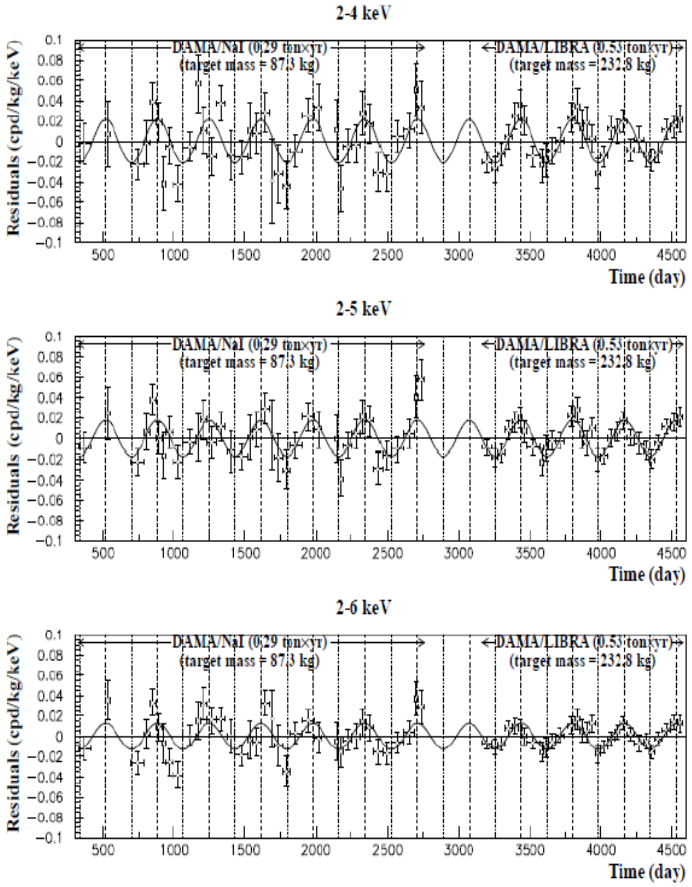

Figure 2.5: Residual rates measured by DAMA/LIBRA experiment [16]

CDMS

The Cryogenic Dark Matter Search (CDMS II) is a series of experiments designed to detect WIMPs located at the Soudan Underground Laboratory in Minnesota. They used a super conducting detector composed of an array of 30 detectors of 19 Ge and 11 Si in operation below 50 mK. The CDMS detectors can get information about what kind of particle caused the event by measuring the ionization and phonons produced by each interaction. The timing information due to phonon pulses is also used for better reduction of surface background. They observed two events in the signal region with estimated background of 0.9 events, but considered these events were leakage surface events. The CDMS Collaboration set an upper limit for the WIMP-nucleon

spin-independent cross-section of 3.8 $\times 10^{-44}$ cm^2 with 90% C.L. for a WIMP mass of 70 GeV/c^2 [17].

SuperCDMS is an upgrade to the CDMS II with new detector hardwares and search for low mass WIMPs. An exposure of 577 kg·days was analyzed for WIMPs with mass < 30 GeV, with the signal region blinded. Eleven events were observed after unblinding. They set an upper limit on the spin-independent cross-section of 1.2 $\times$ 10^{-42} cm^2 at 8 GeV/c^2 [18].

XENON10/XENON100

The XENON collaboration operates a dual phase Xe time projection chamber (TPC)

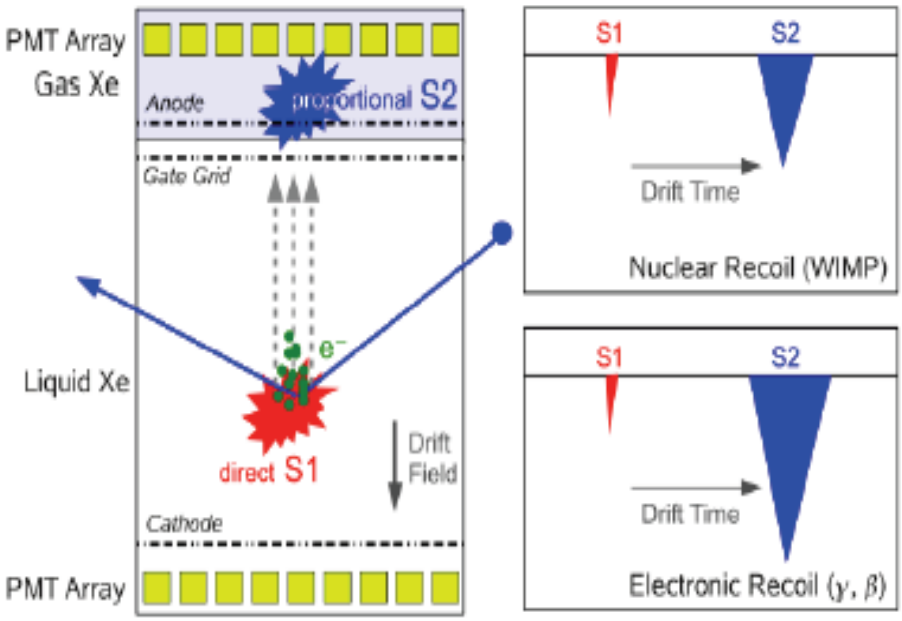

Figure 2.6: Schematic of the particle interaction inside a double phase Xe TPC [19]

with liquid and gas phase at the Gran Sasso laboratory of the I.N.F.N.. The basic idea is analytically separating electron recoil events from nuclear recoil events which may include WIMP signals using the difference of scintillation lights. Primary scintillation lights produced in the liquid phase are called "S1" and secondary electro-luminescence signals are called "S2".

The XENON10 collaboration applied a blind analysis of 58.6 live days of data, acquired between October 6, 2006 and February 14, 2007, and using a fiducial mass of 5.4 kg , and set an upper limit on the WIMP-nucleon spin-independent cross-section of 8.8×10^{-44}cm^2 with 90% C.L. for a WIMP mass of 100 GeV/c^2 [20].

The XENON100 collaboration applied a Profile Likelihood analysis of 224.6 live days of data, acquired between, 2011 and 2012, and using a fiducial mass of 34 kg , and set an upper limit on the WIMP-nucleon spin-independent cross-section of 2×10^{-45} cm^2 with 90% C.L. for a WIMP mass of 55 GeV/c^2 [21].

LUX

The LUX detector (Large Underground Xenon) is a 370 kg dual phase Xe TPC similar to the XENON100 operating in the new Stanford Underground Research Facility in US. They applied a Profile Likelihood analysis of 85.3 live days of data, acquired during 2013, and using a fiducial mass of 118 kg , and set an upper limit on the WIMP-nucleon spin-independent cross-section of 7.6×10^{-46} cm^2 with 90% C.L. for a WIMP mass of 33 GeV/c^2 [22]. This is the best limit of the spin-independent WIMP-nucleon elastic scattering so far.

XMASS
The XMASS is a large single-phase liquid-xenon detector located underground (2700 m water equivalent) on the Kamioka Observatory of the Institute for Cosmic Ray Research (ICRR) in Japan. XMASS has a plan for three phases of experiments; the 100 kg prototype detector, the 1 ton class detector, and the 20 ton class detector. The construction of 800 kg detector (XMASS-I) started in 2007. Data taking of a commissioning phase for the dark matter search started in October 2010 and finished in May 2012. After this run, a detector refurbishment work started in 2012 to reduce radioactive backgrounds inside the detector. Several experimental results have been published using the data taken during the commissioning phase for a low mass WIMP search [23], solar axion search [24], inelastic scattering WIMP search [25], super WIMPs search [2], and two-neutrino double electron capture search [26]. The detail for the detector is explained in Sec. 6 and the refurbishment work is in Sec. 9. A new data taking after the refurbishment restarted from December 2013, and is running in stable condition.

2.2.2 Axions

Axion is originally introduced by Peccei and Quinn to solve the CP problem in QCD [27]. The strong CP problem is the question of why QCD dose not seem to break the CP-symmetry. According to QCD, CP symmetry could be broken in the strong interaction but any such experimental results have not been known so far. The axion is a pseudo Nambu-Goldstone particle and emerges at the f_a scale. The axion is very light but can be candidate for cold dark-matter because the particle can be produced non-thermally. The axion is zero mass at the temperature higher than phase transition of QCD and the field can take arbitrary values parameterized by misalignment angle θ. The axion gets mass by instanton effect at T<1 GeV. When the mass become comparable with Hubble parameter, the fields begin to oscillate around the minimum potential unless the initial value is zero. These kind of coherent oscillations convert the energy stored in the fields to physical axion quanta.

The relic abundance of axion by this mechanism is

$$\Omega_a h^2 \sim 0.16(\frac{m_a}{10\mu eV})^{-1.18}\bar{\theta_i^2}, \tag{2.7}$$

where $\bar{\theta_i}$ is the average of θ_i at the beginning of the oscillation. If $\theta \sim O(1)$ and $f_a \sim 10^{11}$ GeV ($m_a \sim 10$ μeV), the axions can explain the amount of dark matter.

Axions can be detected with axion-photon conversion (Primakoff effect) in strong magnetic field condition. A light axion of μeV order has been searched for using the Sikivie RF cavity technique. A search for 2.3 - 3.4 μeV mass range was conducted, but no significant signal was found [28]. On the other hand, a heavy axion has been

searched for as a solar axion in superconducting magnet telescopes using the inverse Primakoff effect [29] such as CAST [30] and the Tokyo helioscope group [31].

2.2.3 Hidden Photons

A hidden-photon is a massive vector boson that can mix with the ordinary photon by "kinetic-mixing". The hidden-photon might provide a way for ordinary matters to couple with new particles in a "hidden sector" that do not interact by the strong, weak, or electromagnetic forces. The hidden-photons themselves which produced thermally or non-thermally in the early universe can constitute the dark matter. The detail of the hidden-photon particles are described in Chap.3, and the relationships with dark matter are described in Chap.4.

2.2.4 Other dark matter candidates

Asymmetric dark matter (ADM) is based on the idea that there is an imbalance in dark-matter and anti dark-matter like baryon asymmetry. ADM received a lot of attentions because some direct detection anomalies in the sub-10 GeV suggest the possibilities of the dark matter in these energy regions. Mirror dark matter which is a special case of ADM but introduced by a quite different motivation have been also motivated by these signals. The details for these non-WIMP dark matters are explained in [32]. Strongly Interacting Massive Particles (SIMPs) is also receiving attentions recently. The pion like particles play the role of dark matter in this model. Assuming that the dark matter interact strongly each other, the distributions of galaxies can be explained more precisely by the simulations [33].

Chapter 3

Hidden photons

3.1 Hidden photon theory

A hidden-photon - also called "dark", "para", "secluded", and "heavy" photon - is a gauge boson of a hypothetical hidden local U(1) symmetry.

$$[SU(3)_c \times SU(2)_L \times U(1)_Y]_{SM} \times U'(1). \tag{3.1}$$

This extra symmetry is the most simplest and common in the many extension of the standard model, especially in those based on string theory. Okun and Holdom proposed hidden-photons interacting with photons by kinetic mixing [34] [35]. The lagrangian can be described as

$$\mathcal{L} = -\frac{1}{4}F_{\mu\nu}^2 - \frac{1}{4}V_{\mu\nu}^2 - \frac{\kappa}{2}F_{\mu\nu}V^{\mu\nu} + \frac{m_V^2}{2}V_\mu V^\mu + eJ_{em}^\mu A_\mu, \tag{3.2}$$

where $F_{\mu\nu}$ and $V_{\mu\nu}$ is the field strength of photon and hidden photon respectively, κ is the kinetic mixing, m_V is the hidden photon mass, and J_{em}^μ is the electromagnetic current. Kinetic mixing is produced by an exchange of a heavy communicator coupling to both hidden-photons and photons with coupling constant g_h. The natural value of the kinetic mixing is essentially expressed by $\kappa \sim eg_h/(16\pi^2)$ as the couplings of the visible and the hidden gauge. The hidden gauge coupling g_h is of order one and thus $\kappa \sim 10^{-3}$ in field theory and in compactifications of heterotic string theory. However, the hidden photon gauge coupling g_h can be very small and have no clear minimum in large volume string compactifications.

Hidden-photons have been historically gathered attentions as a tool to solve the muon anomaly at sub-GeV scale and constitute the right amount of dark radiation favored by recent CMB observations if their mass are in the meV scale and their kinetic mixing is in the micro range. For these attractive motivations, the hidden-photons have been searched for in wide mass region with many kind of observations and experiments. Figure 3.1 shows the parameter space of hidden-photons and the summary of the current bounds [36].

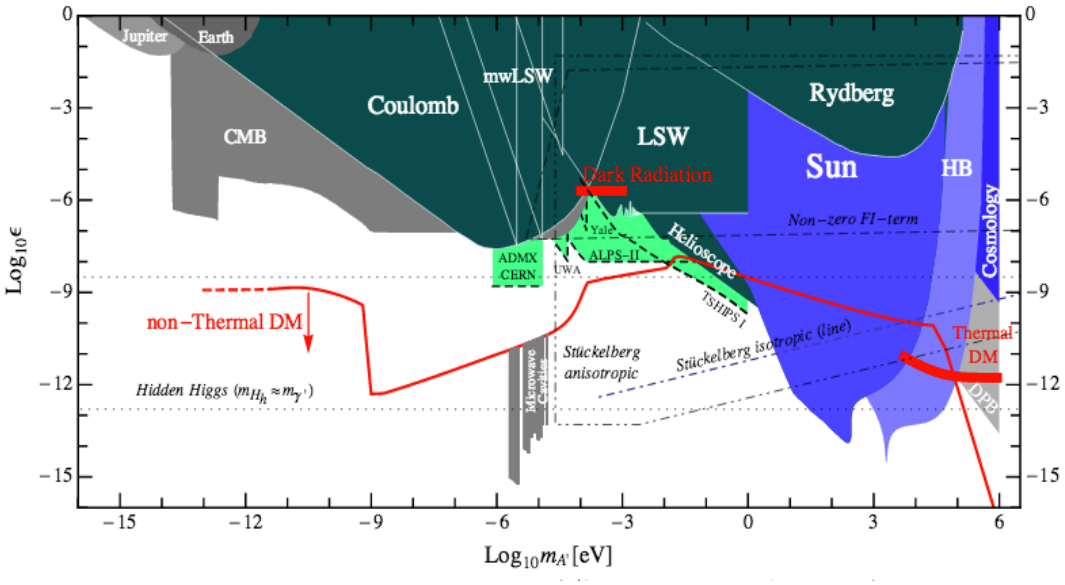

Figure 3.1: parameter space for hidden-photons (adapted from [36]). Existing constraints are indicated with gray/blue/dark green shades. Expected limits from future measurements are indicated with light green shades. The red line indicates the possibilities of hidden-photons as dark-matter. kinetic mixing parameter κ is indicated as ϵ in this figure.

3.2 Previous studies for Hidden photon search

The search for hidden-photons can be divided into $m_V > 1$ MeV and $m_V < 1$ MeV energy region. In $m_V > 1$ MeV case, a hidden-photon may decay to other charged standard particles. That kind of decayed particles can be detected by ready-made detectors, if the heavy hidden-photons are produced. On the other hand, in $m_V < 1$ MeV case, that kind of decays are forbidden kinetically and only the decay to 3γ is allowed. These low mass hidden-photons are searched for using a coupling between a photon and a hidden-photon by kinetic mixing.

3.2.1 Laboratory experiments

Light hidden-photons ($\sim$meV) has been searched for with photon regeneration experiments ("shining through the wall"). Although photons in a laser beam basically blocked by the material placed on the beam line, converted hidden-photons with some probabilities can go through the wall. Then, the hidden-photons are converted back to photons with the same probabilities. The Any Light Particle Search II (ALPS-II) mounted at DESY [37] is trying to detect the signals. The sensitivity of ALPS-II in its final phase is shown in Fig. 3.1.

3.2.2 Stellar hidden photons

Observations

Solar
The bound labelled "Sun" in Fig. 3.1 comes from the non-observation of hidden-photons emission from the Sun. Requiring that the exotic luminosity is smaller than the standard photon luminosity provides a constrain for the kinetic mixing parameter down to $\kappa \sim 10^{-14}$ at $m_V \sim$300 eV [38].

Horizontal Branch Stars
Clearly, horizontal branch (HB) stars can also be exploited to bound the parameter space. The core of an HB star burns helium into carbon and oxygen at a quite constant temperature of 8.6 keV and density $\sim 10^4$ gr cm^{-3}. With these characteristics an HB core is still a classical plasma and the Compton process can provides the most important hidden-photon production mechanism. The non-observation of hidden-photon emission provides constraints for the parameter with a peak at the plasma frequency of $\sim$2.6 keV [43].

Red Giant Stars
More hotter stars, such as red giants are more dense, and have larger plasma frequencies ($\omega_P \sim$200 keV). The constraints by Red Giants are not mentioned in Fig. 3.1. The constraints are calculated in Ref. [51]. We adopted this constraints to compare with our result in Sec. 11.

Helioscopes

Helioscopes try to detect transversely polarized hidden-photons emitted from the solar interior. The Tokyo Axion Helioscope mounted in Tokyo University and the CERN Axion Solar Telescope (CAST) set the limits around meV hidden-photon mass region [39] [38]. Recently, dish antenna type detectors were proposed [40], and some results were published. These sensitivities reach the region where meV mass hidden-photon can be cold dark-matter [41].

3.2.3 Diffused Gamma Background

Hidden photons whose masses are below twice the electron mass can only decay into three photons ($V \to 3\gamma$). The decay of HPDMs can contribute to the observed γ-ray background. The signals of HPDMs decaying into three photons have no sharp line in the observed spectrum. By imposing a constraint on the γ-ray flux from decaying HPDMs that does not exceed the total observed γ-ray flux, we can obtain a bound for the mass-mixing parameter region. The rightmost red line in Fig. 3.1 indicates the diffused gamma background constraint calculated in [49].

Chapter 4

Hidden photons as dark matter

In this section, we will discuss how hidden-photons constitute the present dark-matter density in the universe. We will mention first thermally produced hidden-photon dark-matter, and then non-thermally produced hidden-photon dark-matter.

4.1 Thermally produced HPDMs

The hidden-photons whose mass is $\sim$ 100 keV and kinetic mixing is $\sim 10^{-12}$ can be produced by thermal production mechanism. In the early universe, the photon bath partly converts into a hidden photon bath at the resonance condition. The efficiency of this conversion depends on the effective kinetic mixing parameter. A hidden photon produced thermally can be searched for by direct dark-matter detections or the search for 3γ decayed from the hidden-photons. These relatively warm dark-matter can be also called "super-WIMPs". These kind of dark-matters are motivated because they might solve the problem of a much richer structure formation of the universe with cold dark-matter. The details are described in [42], [43], and [44].

We searched for this bosonic super-WIMPs with XMASS detector in 2013 [2]. The obtained upper limit on coupling constant is shown in Fig. 4.1. The coupling constant required to reproduce the observed dark matter abundance by thermal production is also shown. This was the first direct detection experiment exploring the vector super-WIMPs in the mass range between 40 and 120 keV. We used the data taken in the commissioning phase between December 24, 2010 and May 10, 2012. We used 132.0 effective live days of data, and using a fiducial mass of 41 kg and excluded the possibility that such particles constitute all of dark-matter.

The purpose of this thesis is a search for HPDMs produced by a new production mechanism discussed in the next section as well as an improvement of this result.

4.2 Non-thermally produced HPDMs

In recent articles, Nelson and Scholtz have considered the possibilities that the misalignment mechanism (originally proposed in [46] and [47]) could also be applied for hidden-photons to generate a population of dark-matter in the universe in a way analogous to axion and Axion Like Particles (ALPs). The allowed parameter spaces are evaluated in Ref. [48] and [49]. In this case, a small part of hidden-photon dark-matter

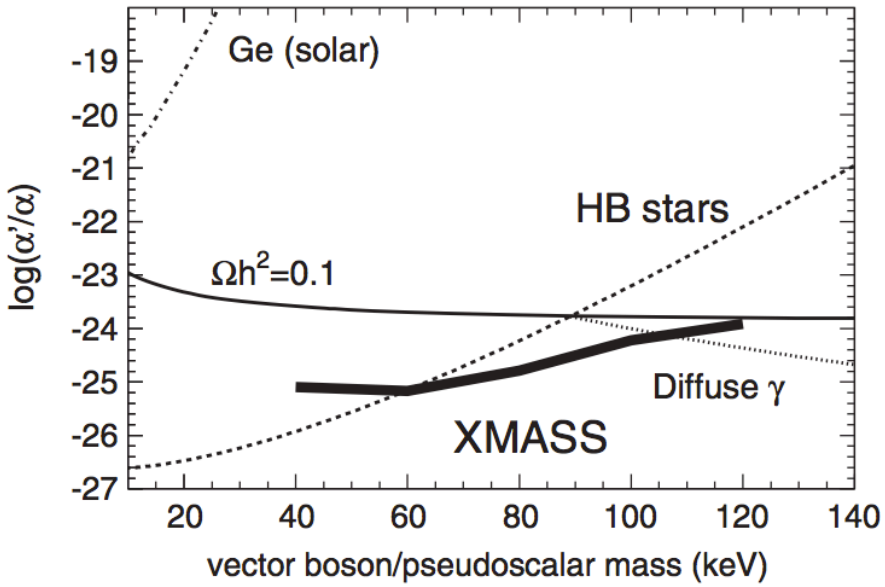

Figure 4.1: Constraints on coupling constants α'/α $(= \kappa^2)$. The thick solid line indicates the upper limit by XMASS commissioning phase data at 90% C.L. The thin solid line corresponds to the coupling constant required to reproduce the observed dark matter abundance by thermal production [42] [43]. The dotted line and dashed line correspond to the upper limit from the diffused gamma background and the constraint from the He-burning lifetime in horizontal branch (HB) stars, respectively [43]. The dash-dotted line indicates an experimental constraint assuming production in the Sun [45].

can oscillate into photons in the early universe and the abundance can leave footprints on the present universe.

4.2.1 Misalignment mechanism

The fields of hidden-photon are assumed to be random initial states in the early universe in the regime of misalignment mechanism. Assuming the universe underwent a period of inflation at a value of the Hubble expansion parameter (H) larger than the hidden-photon mass (m_V), $m_V \ll H$, the spatial component of the equation of motion in the expanding universe are described as

$$\ddot{V}_i + 3H\dot{V}_i + m_V^2 V_i = 0. \tag{4.1}$$

The solution of this equation can be divided into two epochs. For $3H \gg m_V$, the evolution of the fields is overdamped and V_i is frozen at its initial value $V_{I,i}$. When the hubble parameter become comparable with the hidden-photon mass ($3H(T_{osc}) = m(T_{osc})$), the fields begin to oscillate around the local minimum of the potential. The energy density which takes the initial value $\rho \approx m_V^2 V_{I,i}^2$ consequently redshifts with the scaling law for non-relativistic matter. The corresponding energy density parameter of the HPDMs can be described as

$$\Omega_V h^2 \approx 0.4 \frac{g_*(T_{osc})^{3/4}}{g_{*S}(T_{osc})} \sqrt{\frac{m_V}{1keV}} \left(\frac{V_{I,i}}{10^{11}GeV}\right)^2. \tag{4.2}$$

We need to consider the effect of interactions between hidden-photons and the primordial plasma if we want to derive the real relic abundance of hidden-photons in the present universe. But in any case, the equation depends on the initial value $V_{I,i}$ which can take arbitrary values after inflation. In other words, basically any sets with hidden-photon mass and kinetic mixing can constitute the cold dark-matter abundance ($\Omega h^2 \cong 0.12$) for now. In this thesis, we assume that the cold dark-matter is filled with hidden-photons. More details about the misalignment mechanism for hidden-photons are in Ref. [49].

4.2.2 Allowed regions for HPDMs

Figure 4.2 shows the allowed region for HPDMs (light red area) and the existing constraints (grey areas) [50]. Some precise observations of CMB spectrum, abundances of light elements created during BBN, and the isotropic diffused gamma background give us some constraints on such models. Additionally some regions by the near future experimental prospects (shown in different shaded of green), and interesting target regions based on the models of string theory (dashed, dotted, and dashed-dotted lines) are also shown. The prospected mass regions searched by the near future experiments can be separated into three regions. The μeV mass region can be searched by the LSW techniques such as ADMX, CERN and UWA. The eV mass region (optical regime) will be operated by ALPS-II. The dish antenna gives the prospects for a broadband search for HPDMs according to Ref. [40]. A first result by dish antenna set an upper limit on the kinetic mixing parameter of $\sim 6 \times 10^{-12}$ for the hidden-photon mass m_V=3.1$\pm$1.2 eV [41]. The mass region of $O(1)$ keV - 1 MeV of HPDMs can be searched by direct detection experiments for WIMP dark-matter search (DM ionization). Haipeng

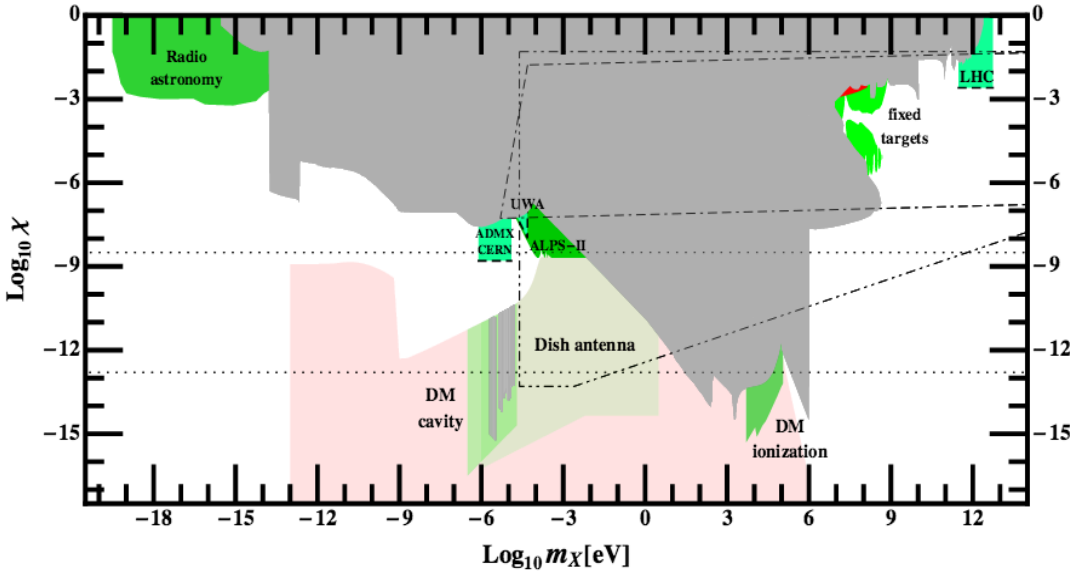

Figure 4.2: Some representative methods and interesting target region for HPDMs [50].

et al. derived constraints on the HPDMs in the 0.01 - 100 keV mass region using the data taken by XENON10 and XENON100 detector [51]. XMASS detector also have sensitivity to the HPDMs of $O(10)$ keV mass region.

Chapter 5

Direct detection of HPDM

5.1 Axio-electric effect

We discuss the method of direct search for HPDMs. Bosonic particles like hidden-photons have possibility to transform their rest mass to kinetic energy and be detected by a detector directly. XMASS detector can detect the electrons emitted from this effect and a monochromatic peak whose energy is corresponding to the rest mass of the HPDM is expected. we need to know the cross section of this photoelectric-type ionization (Axio-electric effect) to calculate the event rate detected by the detector. The energy region of interest was set to 50 - 120 keV in this study. The lowest limit was set by the increase of the background and the xenon K-edge ($\sim$ 34.6 keV). The higher limit was set at 120 keV by the validity of the application of the equation. Providing the hidden photon is cold dark-matter and non-relativistic in the present universe, the total energy of the HPDM is equal to the rest mass ($\omega = m$). On the other hand, the astrophysics bounds are derived in the regime $\omega \gg m$. In this case, we need to concern about the distinction of the polarization of the particles. In the case of non-relativistic particles, the cross section can be described as [42],

$$\frac{\sigma_{abs} v}{\sigma_{photo}(\omega = m_V)c} \approx \frac{\alpha'}{\alpha} = \kappa^2, \tag{5.1}$$

where σ_{abs} is the absorption cross section of the vector bosons on an atom, v is the velocity of the incoming HPDM particles, σ_{photo} is the cross section for the photoelectric effect, α is the fine structure constant, and α' is the fine structure constant of HPDM particles analogue to the photon's. κ is the kinetic mixing parameter. The equation is nearly independent of the HPDM velocity, and the HPDM absorption signal is completely insensitive to the intricate HPDM velocity distribution in the galactic halo. This suggests that there is no so-called "turn-over" in the dark matter signals like WIMPs and only the small modulation of the event rate due to the difference of the flux could be observed. However the magnitude of the annual modulation is relatively small ($\pm$7%) and can be negligible in this thesis. This come out the opposite of the case of WIMP elastic scattering.

5.2 Matter effect

In general, the in-medium dispersion in target material effects also must be taken into account for the description of the process of absorption of a hidden photon. The modification of kinetic mixing is [51],

$$\kappa_{T,L}^2 = \kappa^2 \times \frac{m_V^4}{|m_V^2 - \Pi_{T,L}|^2}, \tag{5.2}$$

where $\Pi_{T,L}(\omega, |\vec{q}|, T)$ are the transverse (T) and longitudinal (L) polarization functions of the photon in the matter, which is the function of the total energy ω, kinetic energy $|\vec{q}|$, and temperature T. m_V is the hidden photon mass. If the mass of the hidden photon is much larger than the ionization threshold ($m_V >> E_{th}$), the effects is negligible. On the other hand, the effects can be important as the mass close to the threshold. We can describe the absorption rate in the lab-frame of the detector as,

$$\Gamma_{\mathrm{T,L}} = -\frac{\kappa_{\mathrm{T,L}}^2 \mathrm{Im}\,\Pi_{\mathrm{T,L}}}{\omega}. \tag{5.3}$$

In the assumption of an isotropic and non-magnetic medium, we can express,

$$\begin{aligned} \Pi_L &= (\omega^2 - \vec{q}^2)(1 - n_r^2) \\ \Pi_T &= \omega^2(1 - n_r^2) \end{aligned} \tag{5.4}$$

Where, n_r is the complex index of refraction for electromagnetism. In the cold dark-matter case ($|\vec{q}| \ll \omega$), $\Pi_L = \Pi_T$, and the equation becomes,

$$\Gamma = \frac{\kappa^2 \mathrm{m_V}}{|\mathrm{n_r^2}|^2} \mathrm{Im}\,\mathrm{n_r^2}. \tag{5.5}$$

The complex refractive index (n_r=$1 - \delta + i\beta$) derived from [52] are shown in Fig. 5.1 for liquid xenon. At around the threshold of XMASS detector ($\sim 1keV$), the real part of the index is 0.9997 and the imaginary part of the index is 0.0003. Then $|n_r^2|^2 \approx 1$. The equation end up to become,

$$\Gamma \simeq \kappa^2 m_V \times \mathrm{Im}\, n_r^2 = \kappa^2 \sigma_{photo} \times (\frac{n_A}{v_V}). \tag{5.6}$$

where σ_{photo} is photoelectric absorption cross section, n_A is the number density of target nuclei, and v_V is the velocity of HPDM.

5.3 Expected signal spectrum

Provided all medium effects can be neglected and the HPDM is non-relativistic, the event rate in the detector becomes

$$\mathrm{N} \approx \frac{4(.68) \times 10^{23}}{\mathrm{A}} \kappa^2 (\frac{\mathrm{keV}}{\mathrm{m_V}})(\frac{\sigma_{\mathrm{photo}}}{\mathrm{barn}}) \mathrm{kg}^{-1}\mathrm{day}^{-1}, \tag{5.7}$$

where the standard local dark-matter density of 0.3 GeV/cm^3 was used, A is the atomic mass, κ is kinetic mixing parameter [42]. Actually, the factor of Eqs. 5.7 result in "4.68"

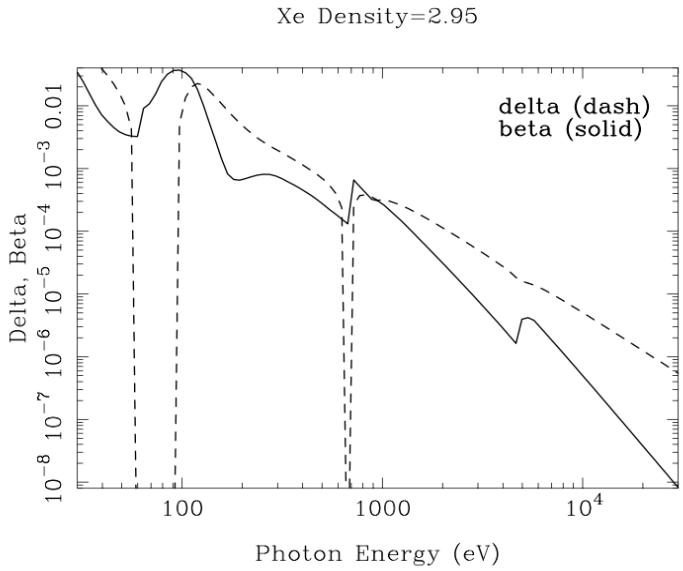

Figure 5.1: The complex refractive index of liquid xenon (n_r=$1 - \delta + i\beta$) [52].

according to the calculation. However, we adopted "4" as a common value used in ref. [42] and [2] in this study.

The expected energy spectrum of HPDMs can be estimated by injecting gamma rays Monte Carlo (MC) simulation uniformly over the entire active volume of the XMASS detector with a gamma energy corresponding to the rest mass of the HPDM. The energy spectra of each HPDM mass are shown in Chap. 10.

Chapter 6

XMASS experiment with liquid xenon

6.1 XMASS

XMASS experiment proposed in 2000 [3] is a multi-purpose low-background experiment using ultra pure liquid xenon aiming to search for dark matter, neutrino-less double beta decay, and low energy solar neutrinos (pp and ^{7}Be). XMASS owes its name to

- Xenon detector for weakly interacting MASSive particle
- Xenon MASsive detector for Solar neutrinos
- Xenon neutrino MASS detector

XMASS has a plan for three phase of experiments; the 100 kg prototype detector, the 1 ton class detector, and the 20 ton class detector. We started the construction of 800 kg detector (XMASS-I) in 2007. The data taking of commissioning phase for the dark matter search started at October 2010 and finished at May 2012. We now started the second data taking after the detector refurbishment for background reduction from November, 2013. The details of the XMASS detector and its characters are explained in this section. Figure 6.1 shows the overall of XMASS detector.

6.1.1 Inner detector (800kg Liquid Xenon)

The inner detector (ID) including approximate 800 kg liquid-xenon is the sensitive part for WIMPs and HPDMs. The liquid-xenon plays a role as a scintillator to detect dark matter signals. This part is surrounded by 642 inward-facing photomultiplier tubes (PMTs) mounted in an approximate spherical holder made of oxygen-free high-conductivity copper (OFHC). The PMT holder is put in an Inner Vacuum Chamber (IVC) filled with liquid-xenon and the IVC is put in an Outer Vacuum Chamber (OVC). The space between IVC and OVC is vacuumed for insulation to prevent heat intrusion from the outside. Fillers made of OFHC are used to fill a gap between the PMT holder and the IVC to reduce amount of liquid-xenon for economical purpose. The PMT holder is assembled into pentakis-dodecahedron structure and has an inner sensitive volume filled with liquid-xenon of 835 kg (832 kg after detector refurbishment). The area of the photo-cathode is maximized by using 630 hexagonal PMTs (HAMAMATSU

R10789-11) and 12 round PMTs (HAMAMATSU R10789-11 MOD). The photocathode coverage of the detector is achieved to be 62.4%. Figure 6.2 shows the structure of the inner detector and Fig. 6.3 shows the inner view and the over view under construction.

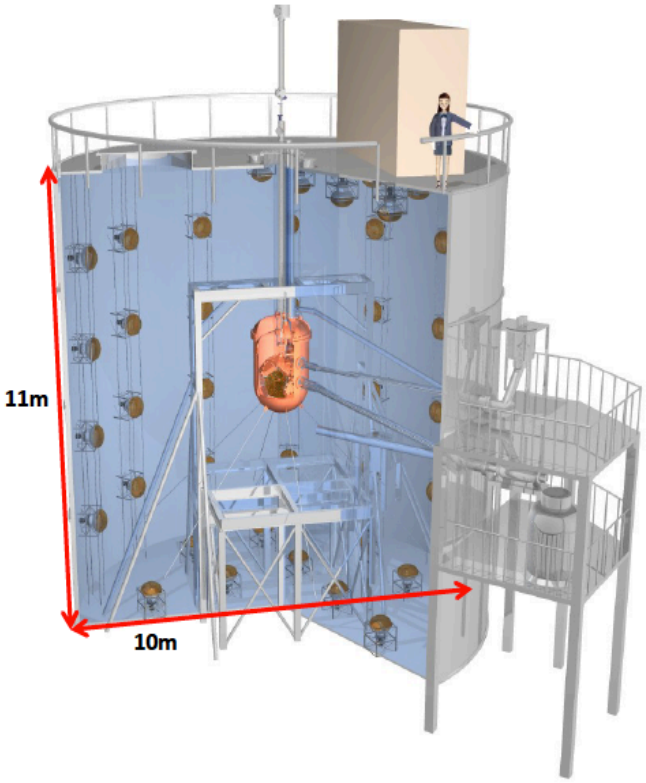

Figure 6.1: Schematic view of XMASS detector

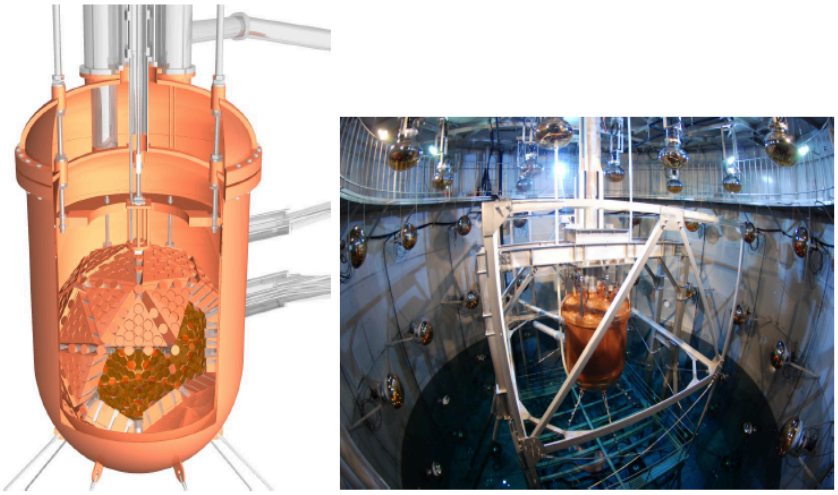

Figure 6.2: Inner detector (PMT holder, IVC, and OVC)

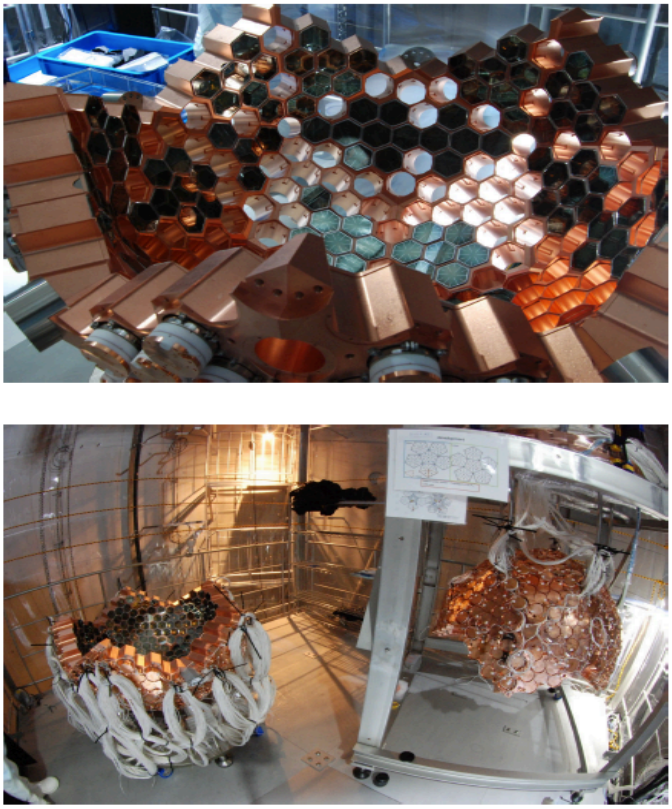

Figure 6.3: PMT holder during the PMT installation work

6.1.2 Outer detector (Water tank)

The Outer detector (OD) is a cylindrical ultra-pure water tank whose diameter is 10 m and hight is 11 m. The tank is made of stainless steel and 72 20-inch PMTs (HAMAMATSU R3600), which are the same type as used in Super-Kamiokande experiment [53], are installed on the inner surface of the tank. The tank was designed to shield the inner detector against γ-rays, fast neutrons, and to tag cosmic ray muons. We can identify and reject muon backgrounds because muons which stopped in the water tank give cherenkov signals in the OD and decayed electron signals in the ID. The actual size of the current water tank is large enough to house future extensions of the XMASS experiment. The water is constantly circulated at 5 ton/h and purified through a system consisting of filters, an ion-exchanger, an UV sterilizer and a membrane degasifier to remove impurities and radon gas. Radon reduced air processed by charcoal is supplied to the space between the water surface and top of the water tank.

6.1.3 Low background PMT

Because γ-rays and fast neutrons from the outside are shielded by the OD, the main background source in the data taken by XMASS was expected to be γ-rays from radioactive impurities inside the ID PMTs. To minimize the background, we developed low-radioactivity PMTs (R10789-11 and R10789-11MOD) with Hamamatsu Photonics K.K. Table 6.1 shows the radioactive contaminants in a PMT, including its voltage divider base as evaluated with HPGe detectors. The PMTs need to work correctly at low temperature ($\sim -100\ ^\circ C$) and have enough sensitivity for 175 nm scintillation lights. The performances of the PMTs are shown in Tab. 6.2. Figure 6.4 shows the picture of the PMT and the circuit of the bleeder. Figure 6.5 shows the dark rate distributions for the OMTs used in the XMASS experiment at room temperature and -100 $^\circ C$.

Isotopes	Radioactivity [mBq/PMT]
^{214}Pb, ^{214}Bi(U − chain)	0.70 ± 0.28
^{228}Ac, ^{212}Pb, ^{212}Bi, ^{208}Tl(Th − chain)	1.5 ± 0.31
^{40}K	< 5.1
^{60}Co	2.9 ± 0.16

Table 6.1: The contamination of radioactive sources in a PMT [54]

Gain	10^7
Dark Noise Rate (room)	200Hz
Dark Noise Rate ($-100^\circ C$)	20Hz
Quantum Efficiency	$> 28\%$

Table 6.2: The performances of the PMTs [55]

Figure 6.4: Hexagonal PMT (R10789-11) and the circuit in the bleeder

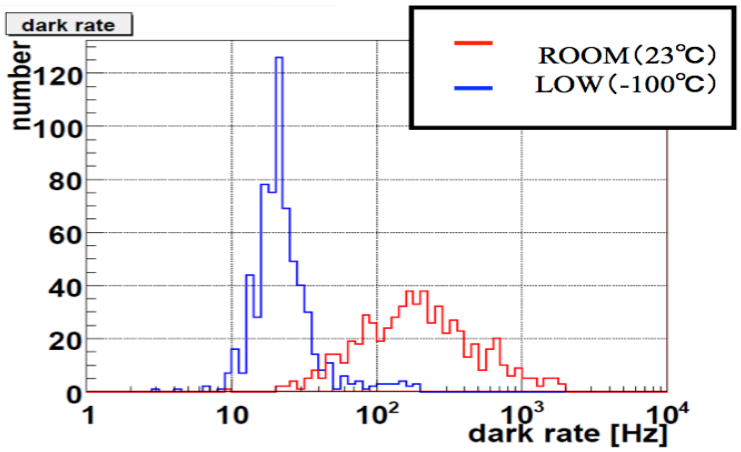

Figure 6.5: Dark rate for the PMTs used in the XMASS experiment in room temperature and -100 $^{\circ}C$

6.2 Liquid Xenon

Liquid-xenon is target material for dark matter search in the XMASS experiment and has many advantages for the purpose. These characters are also advantage for HPDM absorption search.

6.2.1 General characteristics

- *High scintillation light yield* (∼42 photons/keV)
  Since a kinetic energy of the WIMP is very small from several keV to several tens of keV, the energy deposit by nuclear recoil of Xe is also small. Therefore, a low energy threshold can be achieved thanks to this large scintillation light, and which is very advantageous to the WIMP search.

- *Relatively longer wavelength of scintillation light* (∼175 nm)
  Peak wavelength of Xe scintillation light is comparatively longer than the other noble gas scintillators (e.g. Ar is ∼ 128 nm). This character enables us to detect the lights directly without a wavelength shifter.

- *Relatively high temperature in liquid phase and ease of phase change*
  LXe can be kept at a relatively high temperature as compared to the other noble gas (-95°C at 0.1MPa). We can easily remove radioactive contaminations from the liquid-xenon and keep the purity with a combination of circulating system because of the ease of circulation between liquid phase and gas phase. Figure 6.6 shows the phase diagram of xenon.

- *High density*
  The detector volume can be compacted thanks to the high density of liquid xenon (2.9g/cm^3). Figure 6.7 shows the relationship between the temperature and the density.

- *Large atomic number*
  Because the atomic number of xenon is large (Z=54), the radiation length is short (2.77cm). It means external γ-rays stop effectively on the surface of the liquid xenon. The center of the detector can be very "silent" without any background events. This enables us to search for dark matter with high sensitivity. This "strong self-shielding ability" is a main idea of the XMASS experiment. The image of the self shielding mechanism is shown in Fig. 6.8. Figure 6.9 shows the attenuation coefficient of γ-rays in liquid-xenon.

- *Many isotopes*
  Table 6.3 shows the natural abundance of the isotope xenon. Xenon has many isotopes. The differences in the interaction by spin can provide information to identify WIMPs by comparing the interactions in even and odd mass number.

The other general properties of liquid xenon are summarized in Tab. 6.4.

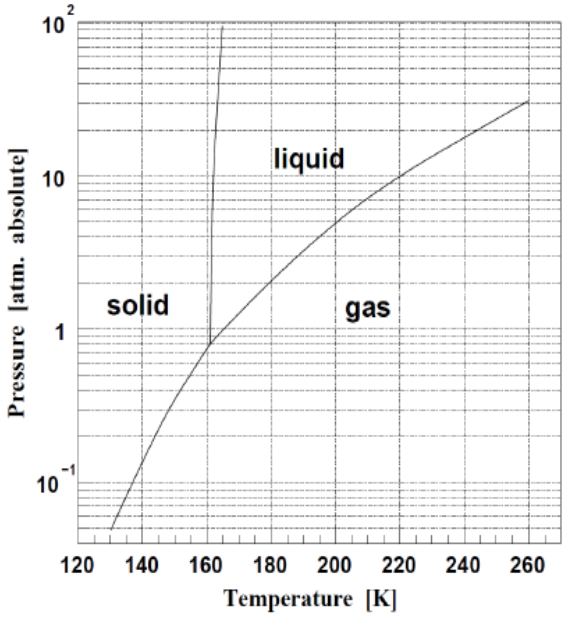

Figure 6.6: Phase diagram of Xe [56]

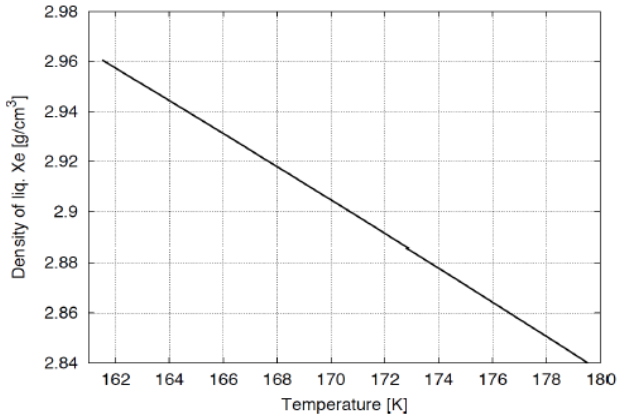

Figure 6.7: The density of Xe as a function of temperature [57]

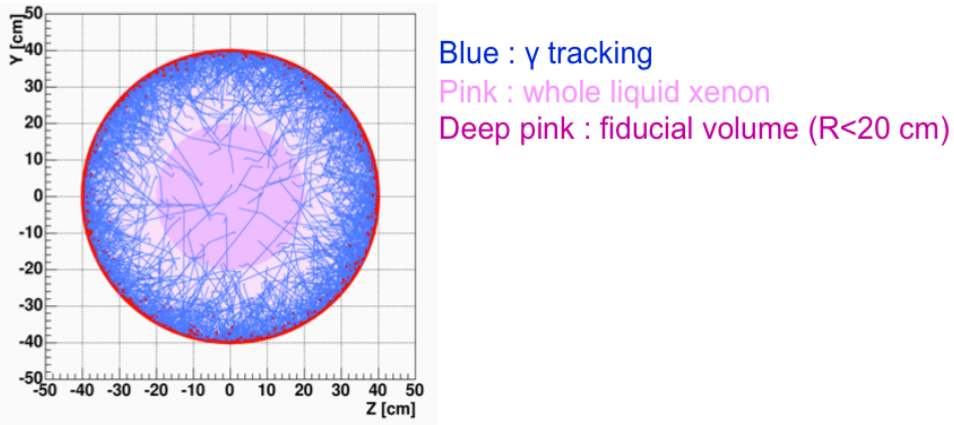

Figure 6.8: γ-ray tracking MC from external to xenon (U-chain γ-rays).

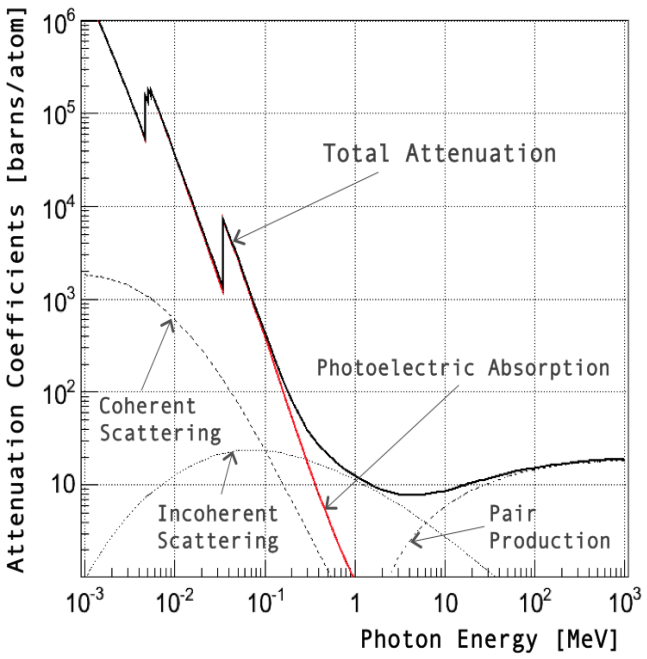

Figure 6.9: Attenuation coefficient of γ rays on Xe [52]

Isotope	^{124}Xe	^{126}Xe	^{128}Xe	^{129}Xe	^{130}Xe	^{131}Xe	^{132}Xe	^{134}Xe	^{136}Xe
Abundance[%]	0.096	0.090	1.92	26.44	4.08	21.18	26.89	10.44	8.87

Table 6.3: The natural abundance of the Xe

Property	Value	Condition	reference
Atomic number	54		[58]
Mass number	131.29		[58]
Boiling point	165.1 K	1 atm	[58]
Melting point	161.4 K	1 atm	[58]
Density	2.96 g/cm^3	161.5 K	[59],[60]
Radiation length	2.77 cm		[59]
Scintillation wavelength	175 nm		
Refractive index	1.61	177 ± 5 nm	[61]
Decay time (recombination)	45 ns	electrons, gamma-ray 1 MeV	[63]
Decay time (singlet)	2.2±0.3 ns	electrons	[63]
Decay time (triplet)	27±1 ns	electrons	[63]
Decay time (singlet)	4.3±0.6 ns	alpha particles	[63]
Decay time (triplet)	22±1.5 ns	alpha particles	[63]
Rayleigh scattering length	~ 60 cm		[62]
Absorption length	≥ 100 *cm*		[62]

Table 6.4: Properties of LXe

6.2.2 Scintillation mechanism of Xenon

The scintillation light is generated by two processes. A charged particle entering xenon deposits its energy through either atomic excitation or ionization. The excitation directly creates a dimer Xe_2^* and the ionization produces free electron. The free electron can either escape from the interaction site or recombine and creates a dimer with a finite timescale. Finally a de-excitation of the all dimer emit scintillation lights of vacuum ultraviolet with a wavelength of $\sim$ 175 nm. The scintillation process of xenon is described in Eqs. 6.1 and 6.2 [64], and the overview of the process of noble gas is shown in Fig. 6.10.

Without recombination process

$$\begin{aligned} \mathrm{Xe}^* + \mathrm{Xe} &\rightarrow Xe_2^* \\ \mathrm{Xe}_2^* &\rightarrow 2Xe + h\nu \end{aligned} \tag{6.1}$$

With recombination process

$$\begin{aligned} \mathrm{Xe}^+ + \mathrm{Xe} &\rightarrow Xe_2^+ \\ \mathrm{Xe}_2^+ + \mathrm{e}^- &\rightarrow Xe^{**} + Xe \\ \mathrm{Xe}^{**} &\rightarrow Xe^* + heat \\ \mathrm{Xe}^* + \mathrm{Xe} &\rightarrow Xe_2^* \\ \mathrm{Xe}_2^* &\rightarrow 2Xe + h\nu \end{aligned} \tag{6.2}$$

The de-excitation has the singlet component caused by a spin singlet state($^1\Sigma_u^+$) and

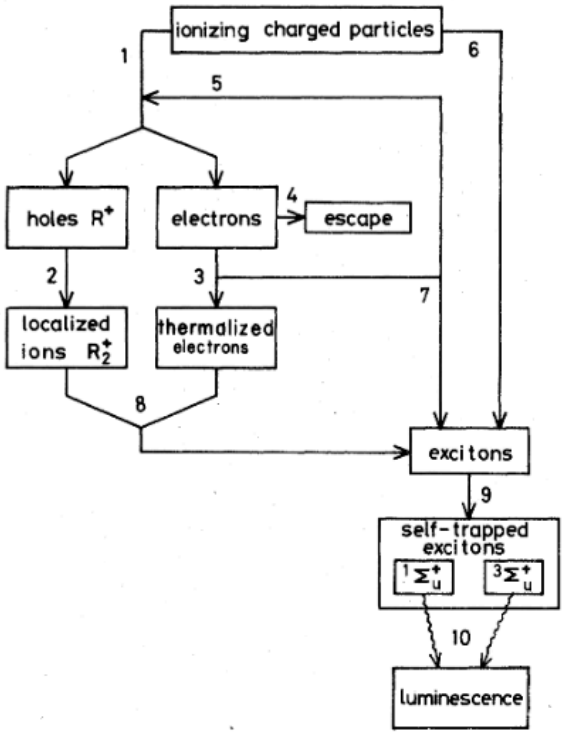

Figure 6.10: General reactions of scintillation processes occurring in noble elements. 1.Production of electron-hole pairs. 2. Formation of molecular ions, R_2^+. 3. Thermalization of hot electrons. 4. Escape of hot electrons from the Coulomb attraction of R_2^+ ions. 5. Production of electron-hole pairs by secondary electrons. 6. Production of excitons by the ionizing particle. 7. Production of excitons by secondary electrons. 8. Recombination of free electrons and molecular ions forming excitons. 9. Self-trapping of excitons forming excited molecules. 10. De-excitation of excited molecules emitting uv photons [65]

.

the triplet component caused by a spin triplet state ($^3\Sigma_u^+$).

6.2.3 Pulse shape for scintillation light

In dark matter search, the identification of nuclear recoil events from $\beta(\gamma)$ backgrounds are studied for extraction of the WIMP signals. On the other hand, The identification of beta events from neutron backgrounds are studied in the experiments for neutrino less double beta decay. The separations of α-ray events and $\beta(\gamma)$-ray are also implemented to identify the source of the backgrounds. We also use this technique to estimate the abundance of the U-chain background in the liquid xenon by separating α-ray events and $\beta(\gamma)$-ray events in Chap. 8.

The pulse shape for a scintillation event can be basically characterized by three components: the singlet lifetime, the triplet lifetime, and the recombination time. Additionally the ratio between the each component also important for the determination of the pulse shape. Of course, a geometry of a detector and responses of electronics can

also affect the pulse shape. We know also electric fields can change the time structure by reducing the recombination component and extracting the free electron from the interaction site according to some studies [65].

In the case of electric recoil, the electron-ion pairs distribute widely because dE/dx is small. On the other hand, the density of the electron-ion pairs is high in the nuclear recoil because dE/dx is large. As described in the previous section, the scintillation mechanism can be classified into two processes determined by whether or not the process includes recombination. If the process includes recombination, the high ion density caused by a nuclear recoil attract electrons with strong Coulomb attraction. Therefore the electrons recombine with the nearest ions before they are thermalized. Then the decay constant is determined by only singlet term and triplet term. On the other hand, in the case of electron recoil events, the recombination occurs after the electron is thermalized because the Coulomb attraction is weak. This cause the long recombination time. This is the mechanism of the difference of the pulse shape between the nuclear recoils (including heavy ions, alpha particles) and the electron recoils. Figure 6.11 shows the pulse shape of 1 MeV electrons and 5.3 MeV alpha particles. We can see there are two component for the alpha particle but only one component for the electron because the recombination term become dominant.

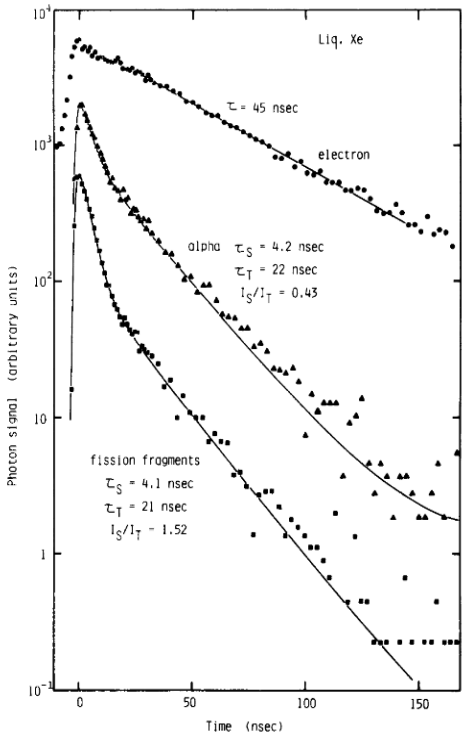

Figure 6.11: Decay curves of the scintillation light obtained for liquid xenon excited by electrons, α particles and fission fragments [68]

6.2.4 Xenon distillation system

Commercial xenon contains a small amount of krypton (0.1 - 1 ppm) [55], which has a radioactive isotope, ^{85}Kr (half-life of 10.76 years). The β-rays from ^{85}Kr can be

background for both of WIMPs and HPDMs search. Our requirement for Kr/Xe is less than 2 ppt. The xenon obtained for our experiment had a Kr/Xe content of 340 ppb and a ^{85}Kr/Kr ratio of $(0.6 \pm 0.2) \times 10^{-11}$ which was measured from off-gas measurement using a high purity germanium (HPGe) detector by ourselves. We developed a distillation system to reduce the Kr/Xe ratio. During the commissioning run, a sample was taken and its krypton concentration was measured by atmospheric pressure ionization mass spectroscopy (API-MS) but no excess over the BG level of the API-MS was found, and an upper limit of 2.7 ppt was obtained for the krypton contamination. The details are reported in [55].

6.2.5 Xenon circulation system

Figure 6.12 shows the flow map of the xenon circulation and purification system for the XMASS detector. H_2O, O_2, and radioactive contaminations can be removed using Charcoal filter or Getter during circulation. Works for removing contaminations were done before the data taking.

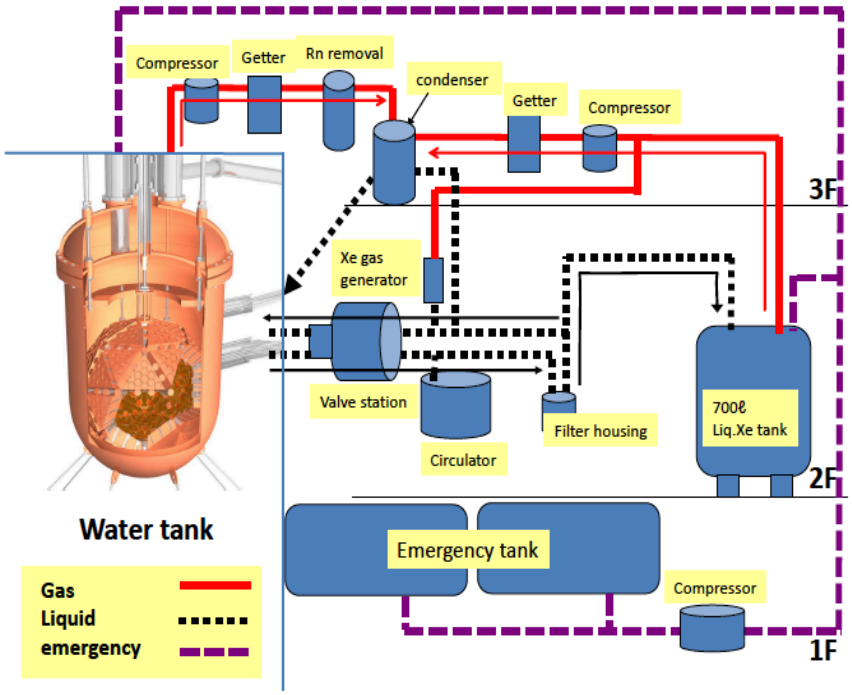

Figure 6.12: Flow map of xenon circulation system for the XMASS detector.

6.3 Data acquisition system

The schematic view of the XMASS data acquisition system is shown in Fig. 6.13. The PMT signals from the ID go through $\sim$ 11m of coaxial cables and feed-throughs that separate the xenon gas volume from the outside air. Analog-Timing-Modules (ATMs) originally developed for and used in Super-Kamiokande I-III were used mainly

for XMASS experiment in the commissioning phase. The ATMs function as Analog-to-Digital Converters (ADCs) and Time-to-Digital Converters (TDCs) and register the information of integrated charge and arrival time for each PMT. Since the ATM has 12 channels per one ATM board, we can take all signals from 642 ID and 72 OD with 66 ATM boards. After the refurbishment work of XMASS detector (The detail for the refurbishment work are written in Sec. 9), the main modules for dark matter searches were replaced by Flash-ADC (Flash Analog-to-Digital Converter) boards. The ATM are used only for generation of triggers and data acquisition for OD in the data used for this analysis.

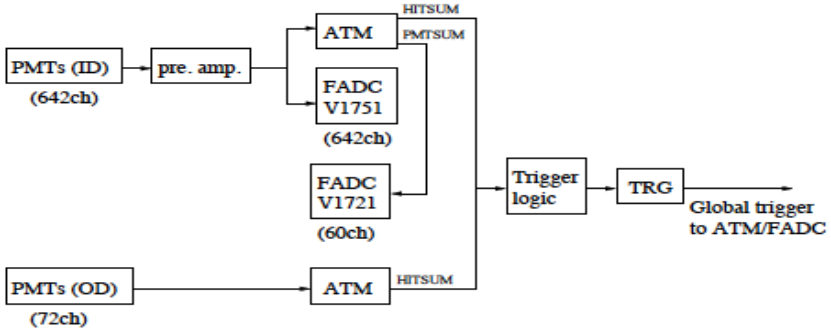

Figure 6.13: schematic view of the XMASS DAQ system

6.3.1 Trigger logic

When the ATMs get a signal whose voltage is less than -5 mV (corresponding to 0.2 P.E.), they generate a rectangular signal 200 ns wide and 15 mV high. The sum of rectangular signals from 12 channels in an ATM board are output from the front panel (HITSUM signals). For generation of a global ID trigger, all HITSUM signals are summed again. When the HITSUM signal exceed the height corresponding to 3 hits, a global ID signal is generated. This system is same for OD triggers (trigger threshold is 8 hits). The typical trigger rate of ID and OD is $4s^{-1}$ and $7s^{-1}$, respectively. The TRG (a custom-made VME trigger module) outputs global trigger signals and 16-bit event numbers and they are fed into ATMs and FADCs regardless of the type of the triggers (ID, OD or external clock trigger). The TRG registers the trigger times (20 ns resolution), trigger types, and event numbers. 6 μs veto are applied after ID trigger in order to reject after-pulses caused by bright events.

6.3.2 Flash ADC

Flash-ADC (FADC) is an electric module which can sequentially convert input analog voltage signals to digital signals. Flash-ADC enables us to handle the signals from the PMTs as waveforms. CAEN V1751 FADCs were installed in December 2011 for better understanding of the background and more sophisticated searches for dark matter signals using timing information. The sampling rate is 1GHz and the dynamic range is 1V with 10bit ($\sim$1mV) resolution (1 mV corresponding to 0.05 P.E.). CAEN V1721

FADCs were used for background analysis in the commissioning phase. PMT-SUM signals, which is an analogue sum of the 12 channels in one ATM board input to the FADC. The input signal is attenuated by a factor of eight. We can analyze high energy events, such as an α-ray events with this FADC modules without saturations.

6.4 Detector simulation

6.4.1 Geant4 based MC package

An MC simulation package for XMASS detector was developed based on Geant4 ([70],[71]). Figure 6.14 shows the geometry of the ID in the XMASS MC. The basic geometries of the detector defined in the MC are determined by the design of the detector. Some finer geometries are determined by the tuning of the MC from some data information. Several optical parameters, such as absorption and scattering length of liquid xenon, reflectance at the inner surface of the PMT copper holder and the aluminum strip on the PMT window, refractive indices of liquid xenon and the quartz PMT window, and the reflection and absorption probabilities at a PMT photo-cathode, are also needed to be determined experimentally. In this study, 600 cm of the absorption length, 52 cm of the absorption length, 0.25 of the reflectance of the copper, and 0.60 of the reflectance of the aluminum were used for the MCs. These parameters were derived as the best fit parameters based on the ^{57}Co calibration data taken in Nov. 22, 2013, and summarized in Tab. 6.5.

Parameters	Best fit value
Absorption length in liquid xenon	600 cm
Scattering length in liquid xenon	52 cm
Reflectance of copper	0.25
Reflectance of aluminum	0.60

Table 6.5: Best fit values of parameter tuning of the calibration MC

The incident particles tracks, scintillation process, propagation of scintillation photons, PMT response and readout electronics are simulated by the MC. Non-linearity of scintillation efficiency, the energy distribution of the scintillation photons, and the quantum efficiency of each PMT are taken into account. Figure 6.15 shows the number of photoelectrons (nPEs) spectrum observed using the Co57 source at z=0 cm and the MC result. The nPEs distribution is reproduced well by the MC.

6.4.2 Event reconstruction

The vertex positions and energies of events are reconstructed using nPE information from the PMTs [55]. Various grid positions are defined in the ID, and expected nPE distributions in each PMT are calculated in the MC. The probability density functions (PDFs) are obtained by normalizing the distributions. We defined Cartesian grid, Polar grid for internal events, and Wall grid, PMT grid, Edge grid, and Valley grid for the inner surface events in our approximately 80 cm diameter detector. In total 3375 cartesian grid are positioned along a 15 cm $\times$ 15 cm $\times$ 15 cm coordinate by

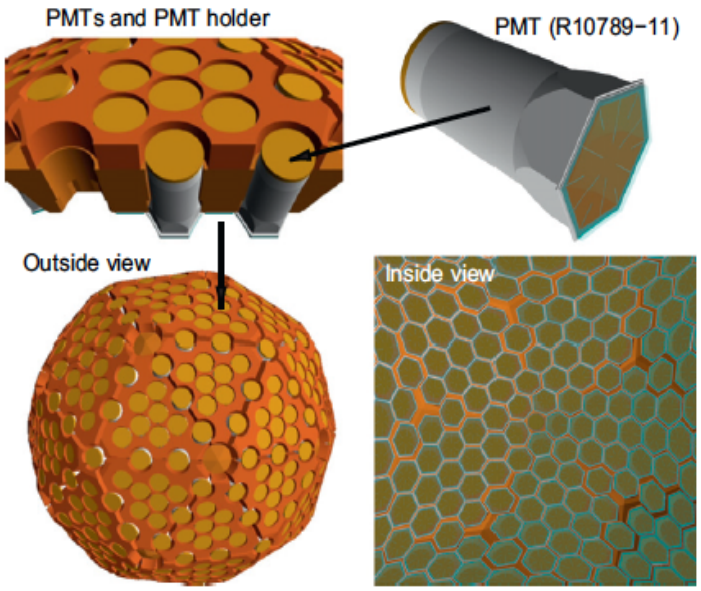

Figure 6.14: XMASS geometry defined in the XMASS MC package

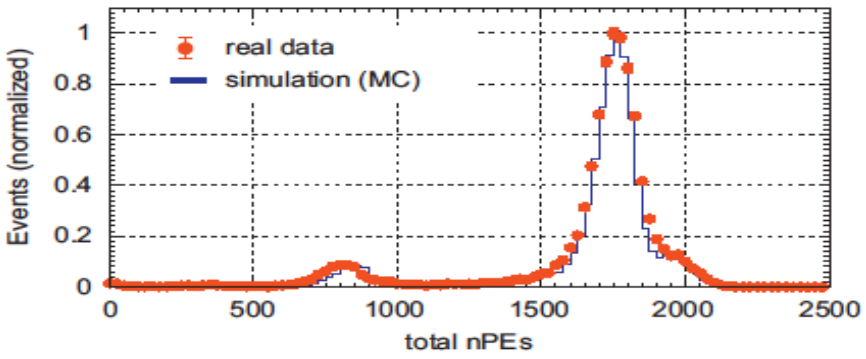

Figure 6.15: Observed nPE distribution using Co57 source at z=0 cm and its MC

3 cm distance. More finer "interpolated grids" are defined along the coordinate by linear interpolation by 1.5 cm interval. Finally, 2 mm distance grids are added by interpolation. Polar grids are defined on radial lines from the center of the detector. Wall, PMT, Edge, and Valley grids are defined around the inner surface of the detector to identify surface events efficiently. The probability, $p_i(n)$, that the ith PMT detects nPE with is calculated using the PDFs. The likelihood of the events on the position $\boldsymbol{x}$ is defined as

$$L(x) = \prod_{i=1}^{642} p_i(n_i). \tag{6.3}$$

Where, n_i expresses nPE for the ith PMT. The most likely position is derived by maximizing L. Figure 6.16 shows the reconstructed energy distribution (upper) and the reconstructed position for various Co57 source positions (lower) respectively.

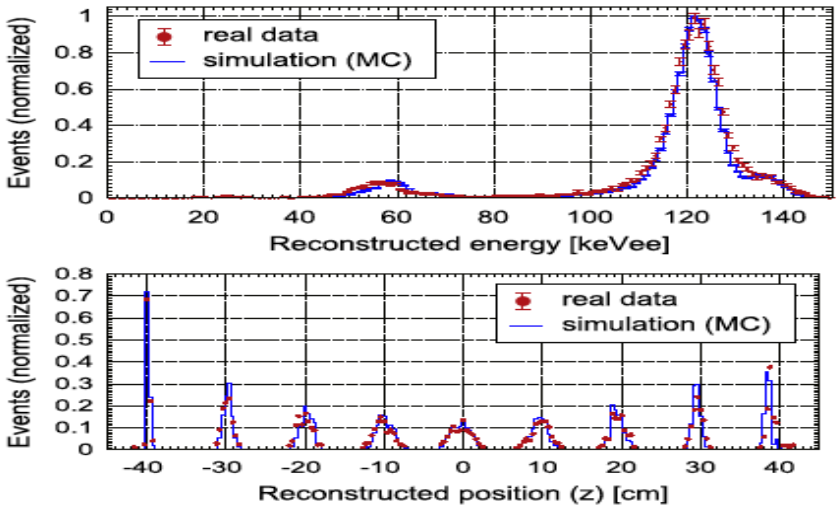

Figure 6.16: Reconstructed energy distribution using Co57 source at z=0 cm and its MC (upper), Reconstructed positions using Co57 source at a-0cm and its MC (upper)

Chapter 7

Detector Calibration

For the purpose of the understanding of our detector responses, we need to calibrate the detector using some well known radioactive sources or light sources. The calibration for XMASS detector have two different aspects. Firstly, using some kind of radioactive sources whose energies, positions, or particles are known, we evaluate some parameters (absorption length of xenon, scattering length of xenon, decay constant and so on.) used in the MC simulations. Secondly, the stability of 1 p.e. gain and photon yield are checked using calibration data taken at regular interval. LED, neutron, inner, and outer calibrations are implemented in XMASS experiment.

7.1 LED Calibration

An investigation of PMT gain stability was performed by a LED calibration. Eight LEDs of blue light with Teflon diffuser were installed at the surface of PMT holder in the ID. Low occupancy LED data were taken with every week for obtaining the PMT 1 p.e. data in the XMASS commissioning phase. This system was upgraded to take the LED data automatically regularly by the DAQ system at the refurbishment. The PMT gain was found to be stable within $\pm 5\%$ [55].

7.2 Neutron Calibration

The study of nuclear recoil was performed by a dedicated neutron calibration system. Figure 7.1 shows the schematic view and the picture of the neutron calibration system. This system was installed at the detector refurbishment work. The system constitutes of radioactive source (^{252}Cf and ^{60}Co), plastic scintillator, lead shield, polyethylene collimator, and a 1.5-inch PMT. ^{252}Cf source enables us to identify the neutron events using the coincidence by γ-ray events which occur simultaneously with the neutron events. Although the light yield L_{eff} of nuclear recoil in the liquid xenon around the dark matter energy region is vigorously studied worldwide, the error is still large. We are required to study the light yield using neutron which cause nuclear recoil as is the case with dark matter signatures in our own detector to minimize the systematic error. The decay constant of scintillation lights between the nuclear recoil and the electron recoil have different values. This information give us the possibilities to separate WIMP dark matter events from backgrounds which are mainly caused by electron recoil events. We

are trying to establish the pulse-shape-discrimination techniques by using waveforms taken by FADC.

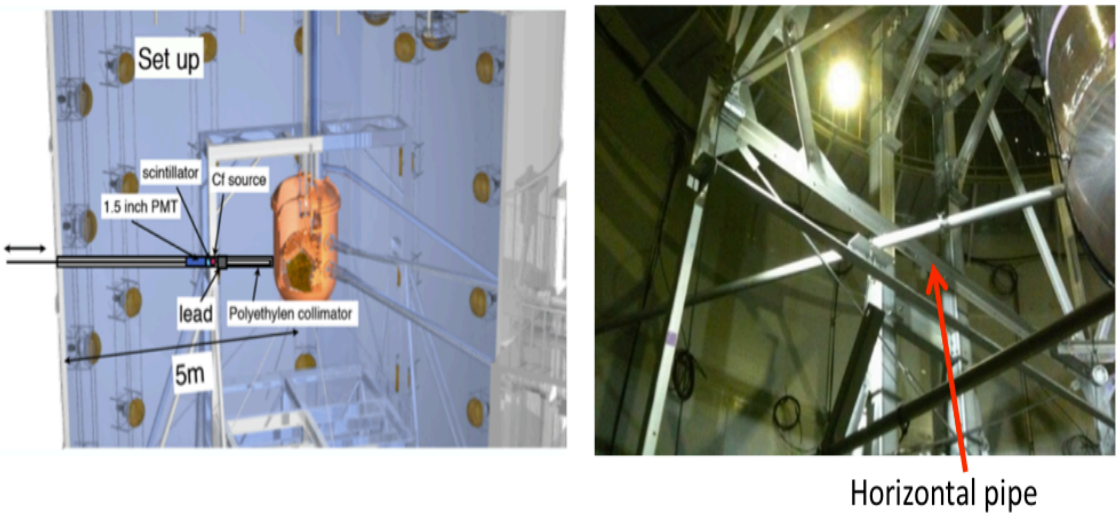

Figure 7.1: The schematic view of the neutron calibration system (left) and the picture of the horizontal pipe for the introduction of ^{252}Cf (right).

7.3 Inner source Calibration

An inner source calibration system is connected to the ID and enables us to insert a radioactive source inside the liquid xenon region along the vertical axis with a precision of better than 1 mm [55]. Fig. 7.2 shows the inner source calibration system, which consists of a radioactive source, an OFHC copper rod, a thin stainless steel wire, and a stepping motor. The radioactive source can be mounted at the tip of the copper rod. Figure 7.3 shows a picture of the edge of the ^{57}Co source rod.

The radioactive sources used in the XMASS experiment are summarized in Tab. 7.1. They can be exchanged without interrupting detector operation. The ^{241}Am and ^{57}Co have a diameter of 0.21 mm [72], which is much shorter than the absorption length for 59.5 keV and 122 keV γ-rays in liquid xenon ($\sim$0.44 mm and $\sim$0.25 mm, respectively). This enables us to take inner calibration data without large shadow effect due to the source geometry. On the other hand, the source geometries for ^{57}Fe and ^{109}Cd calibration sources are different from the ^{241}Am and ^{57}Co calibration sources as shown in Fig. 7.4. More larger shadow effects can be observed.

The ^{241}Am and ^{57}Co were used in the analysis of the HPDMs search for the correction of the energy scale and evaluation of systematic errors. Figure 7.5 shows the reconstructed vertex of the MC and the real data taken during the commissioning run for the ^{57}Co calibration source. The position resolution was 1.4 cm (RMS) at $Z = 0$ cm and 1.0 cm at $\pm$20 cm for 122 keV γ-rays. Figure 7.6 shows the reconstructed energy of the MC and the real data. The energy resolution was 4 % for 122 keV γ-rays. The reconstructed energies and the reconstructed positions for 122 keV γ-rays are reproduced well by the MC.

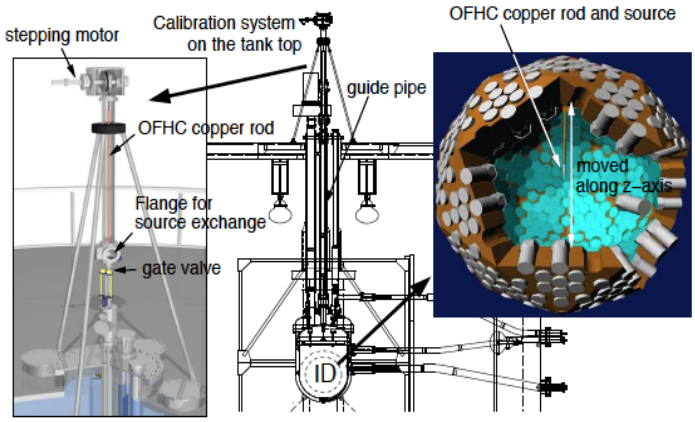

Figure 7.2: Inner calibration system

Figure 7.3: ^{57}Co calibration source rod

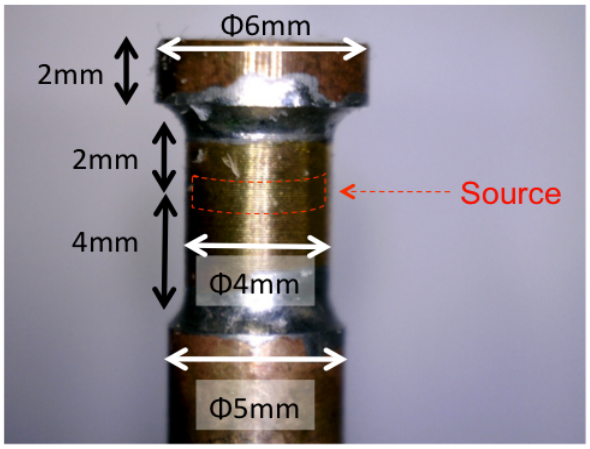

Figure 7.4: Source geometry for ^{57}Fe and ^{109}Cd sources.

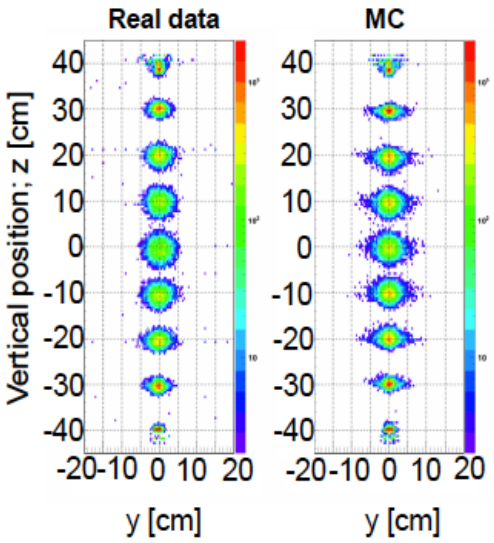

Figure 7.5: The reconstructed vertex distribution of ^{57}Co calibration data and MC

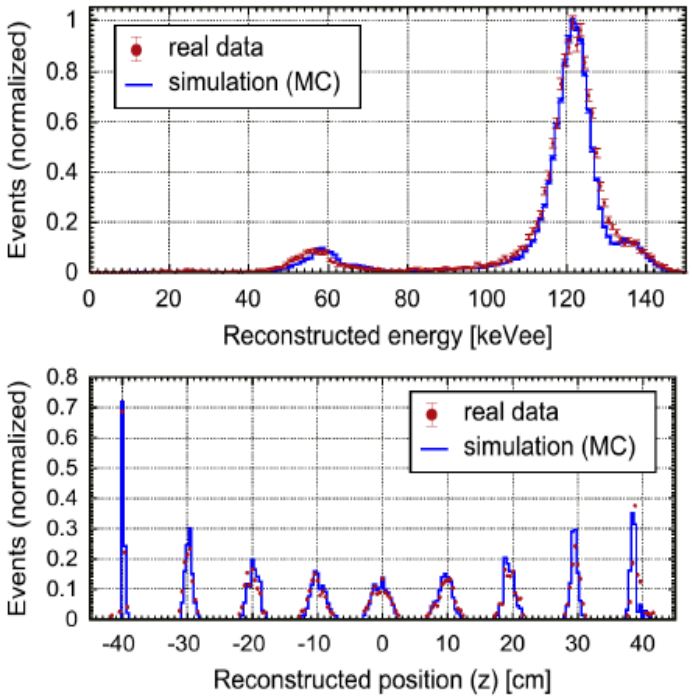

Figure 7.6: The energy spectrum and reconstructed vertex distribution of ^{57}Co calibration data and MC at 122 keV

Isotopes	Energy (keV)	Shape
^{55}Fe	5.9	Cylinder
^{109}Cd	8(*1),22,58,88	Cylinder
^{241}Am	17.8,59.5	Thin cylinder
^{57}Co	59.3(*2),122	Thin cylinder
^{137}Cs	662	Cylinder

Table 7.1: Calibration sources and energies. The 8 keV (*1) in the ^{109}Cd and 59.3 keV (*2) in the ^{57}Co source are K_α X-rays from the copper and tungsten, respectively, used for source housing.

Chapter 8

Background

In experiments searching for rare events, such as dark-matter and neutrino-less double beta decay, one of the main issues is to reduce backgrounds (BGs) to the utmost limits in order to increase the experimental sensitivity. We also paid attention to avoid the radioactive contamination into the XMASS experimental systems.

Figure 8.1 shows the BG levels of some representative low BG detectors adopted from [73]. The BG level of a fiducial volume of XMASS detector in the energy region around 100 keV_{ee} is the lowest compared to the other low BG detectors. This fact enables us to search for HPDM signals with the highest sensitivity. Actually, the BG level after the detector refurbishment (XMASS-RFB) is several times worse than the level before the detector refurbishment (XMASS-CM). This suggests that additional BG components were added during or after the refurbishment. However, we were able to derive a stronger constraint on the kinetic mixing parameter by using a larger statistic as a data set after the refurbishment. The detail will be discussed in the next chapter and Chap. 11.

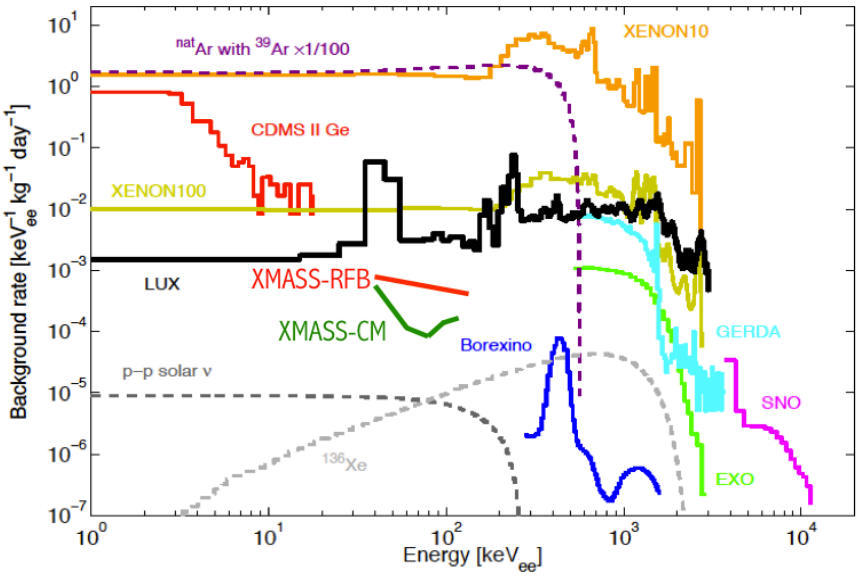

Figure 8.1: Comparison of the BG levels of some representative low BG detectors (adopted from [73]).

In this chapter, we explain about the known BG components. The BG sources are categorized into the external BG, the radioactive contamination in the liquid xenon, and the BGs originating in the detector materials.

8.1 External background

When a cosmic ray proton impacts atomic nuclei in the atmosphere, pions are created and the pions decay into muons (secondary muons) and muon neutrinos. The secondary muons can penetrate to the Earth's surface and become large BGs for the dark-matter search. Therefore, XMASS detector is located underground 1000 m from the top of Mt. Ikenoyama in Japan. The muon rate in the mine is a level of 10^{-5} of the ground [74]. Fast neutrons and gammas from the rocks around the detector can also be obstacles for the dark-matter search. The neutron BG can be separated into the three category based on its production processes.

- Nuclear spallation by cosmic muons
- Nuclear fissions of U and Th chain in the rocks
- (α,n) reactions between detector material or rocks and α particle produced by decay of U and Th chain.

The performance of the water tank as a neutron modulator was evaluated by a simulation study. The study showed that 2 m of water shield can reduce the event rate from the external fast neutron as well as γ-rays to levels of the γ-rays BGs from the PMT materials in the inner detector. The water shield which is more than 4 m thick in all directions is sufficient for this goal [55] [75].

8.2 Internal background

The BGs contaminated in the liquid xenon itself can not be shielded by the water tank or the self shielding by the liquid xenon. Therefore, the inner BGs become the main BG sources after the selection of the fiducial volume of the detector, especially for the energy region of our interest (40-140 keV). We did not try to reduce the inner BG at the detector refurbishment because the level of the inner BG almost achieved our target value for the search for WIMPs. We mention here how to measure the amount of the radioactive contaminations, the obtained values, and the energy spectra for each inner BG sources;Uranium-chain, Thorium-chain, Krypton, Argon, and $2\nu\beta\beta$ from ^{136}Xe.

8.2.1 Uranium chain

^{238}U have long half time ($\tau_{1/2} = 4.5 \times 10^9$ y). The decay chain until the stable nuclei are shown in Fig. 8.4. Beta-rays or low energy γ-rays can be BGs for the detection of dark-matter signals. If a radioactive equilibrium is assumed, the successive two decays are identified by using delayed coincidence technique and the abundance can be estimated.

$$^{214}Bi \xrightarrow[\beta(99.98\%)]{Q=3.27MeV} {}^{214}Po \xrightarrow[\alpha(100\%)]{7.687MeV} {}^{210}Pb \qquad (\tau_{1/2} = 164.3\mu s) \tag{8.1}$$

The amount of ^{222}Rn in the liquid xenon was estimated as 8.2±0.5 mBq/detector in the commissioning run [55] and 7.48±0.04 mBq/detector in the after refurbishment run, respectively. In order to select Bi-Po pairs, The following seven cut-conditions were applied; 1)ID-trigger cut, 2)Number of hit PMTs>=4, 3)TDC-RMS cut, 4)Cherenkov cut, 5)100 μs <Difference of time from the previous event< 1000 μs, 6)Number of photo electron of 2nd event> 2500, 7)Decay slope of 2nd event< 35 ns. The ID-trigger is a selection of ID events. The number of hit PMTs is set to exceed 4hits to maintain consistency with the detector threshold. TDC-RMS cut is for electrical noise cut. The details are described in Chap. 10. Beta-rays from ^{40}K in a quartz of a PMT generates cherenkov light in the PMT. These events can be separated by using the steeper slope of the waveforms compared with scintillation events (Cherenkov cut). The time window of the second event was set to detect ^{214}Po events efficiently ($\tau_{1/2}$=164 μs). The number of photoelectron and the decay slope of 2nd events were set to improve the purity of the ^{214}Po α-ray events. Figure 8.2 shows the decay slope of the events derived by exponential fitting for the waveforms. We can select α-ray events by imposing decay slope cut because α-ray events have steeper decay slope than that of γ-rays and β-rays generally. The photo electron distributions after Bi-Po events selection are shown in Fig. 8.3. The half time of these events is consistent with ^{214}Bi events within the margin of error.

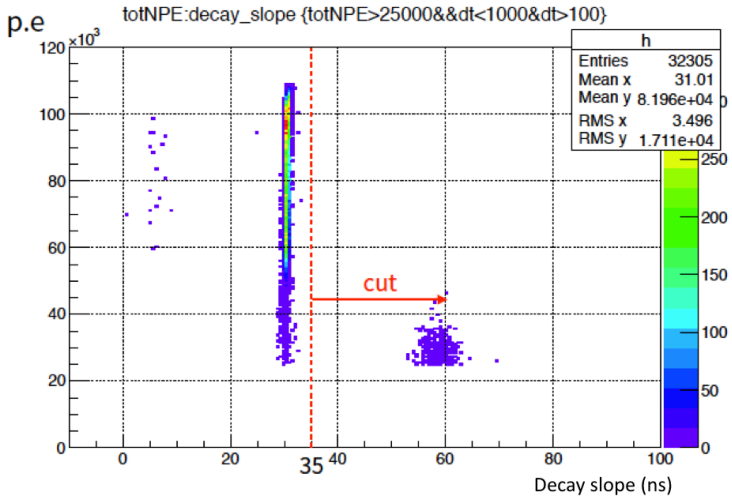

Figure 8.2: A decay slope distribution. The vertically distributed around 30 ns is α-ray like events. The events distributed around 60 ns are γ-ray (or β-ray) like events. The events only more than 2500 p.e. are shown.

8.2.2 Thorium chain

^{232}Th have long half time ($\tau_{1/2} = 1.4 \times 10^{10}$ y). The decay chain until the stable nuclei is shown in Fig. 8.5. Beta-rays or low energy γ-rays can be BGs for the detection of dark-matter signals. If radioactive equilibrium is assumed, the successive two decays are

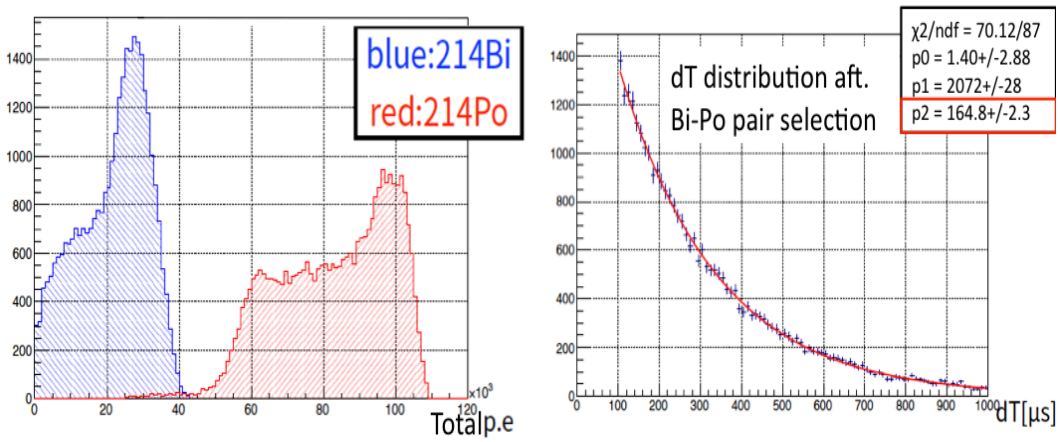

Figure 8.3: The left figure shows photoelectron distributions of ^{214}Bi (β-rays) and ^{214}Po (α-ray) event candidates. The right figure shows the distribution of the time difference of them. The half time derived by fitting by exponential function is consistent with the nominal value (164 μs).

identified by using a delayed coincidence technique and the abundance can be estimated.

$$^{220}Rn \xrightarrow[\alpha(100\%)]{Q=6.288MeV} {}^{216}Po \xrightarrow[\alpha(100\%)]{6.779MeV} {}^{212}Pb \quad (\tau_{1/2} = 0.14\,s) \tag{8.2}$$

The upper limit of the amount of Th232 in the liquid xenon was 0.28 mBq/detector in the commissioning run [55]. After the detector refurbishment, our obtained value is 39 μBq/detector. The contribution is negligible compared with the abundance of the uranium-chain.

8.2.3 ^{85}Kr

^{85}Kr have a half time of 10.756 y. The decay scheme for ^{85}Kr is shown in Fig. 8.6. ^{85}Kr is generated in a reactor and dispersed into the atmosphere. The commercial xenon therefore include the Kr and also ^{85}Kr at the ppm level at the time of manufacture. The expected energy spectrum of β-rays from ^{85}Kr with WIMPs signal is shown in Fig. 8.7. In order to achieve the BG level one order less than 100 GeV WIMP signal with cross section of 10^{-45} cm^2, the target value of the amount of Kr was set to 2 ppt level in the design phase (Here, ^{85}Kr/Kr=$(0.6\pm0.2)\times10^{-11}$ was used [55].). We need to reduce the contamination of krypton at a level of 10^{-5}. For this purpose, the dedicated distillation tower was developed. The details are described in Chap. 6.

During the commissioning run, a xenon sample was taken and its krypton contamination was measured by Atmospheric Pressure Ionization Mass Spectroscopy (API-MS). No excess over the BG level of the API-MS was found, and an upper limit of 2.7 ppt was obtained for its krypton contamination. 99.563% of ^{85}Kr decay to ^{85}Rb by β decays (Q=687 keV). This beta spectrum interrupt the search for hidden photons as well as WIMPs. Remaining 0.434% of ^{85}Kr decay to excited state of Rb85 by β decay and then emit γ-ray (514 keV) by 1.015 μs half life.

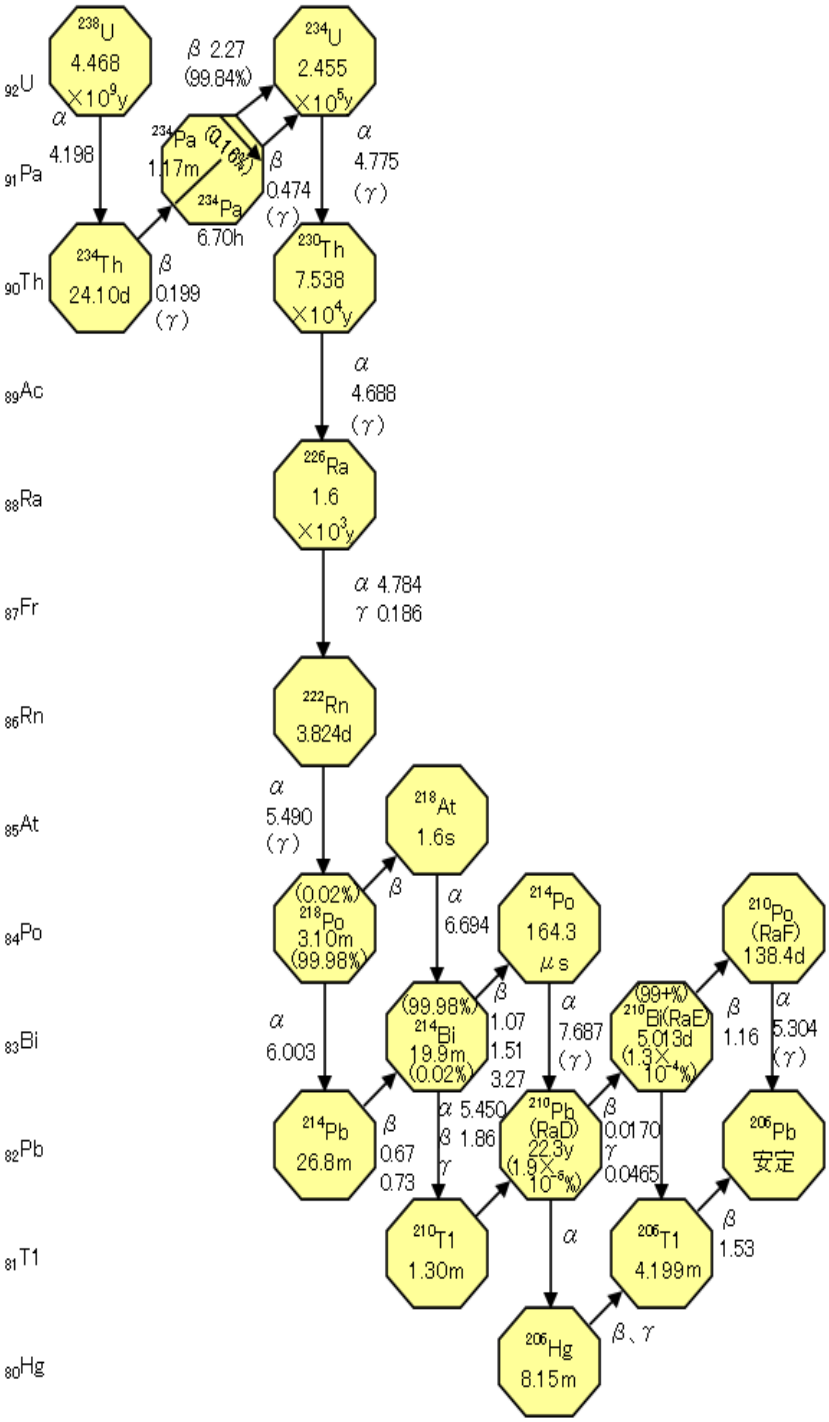

Figure 8.4: Uranium chain [76]

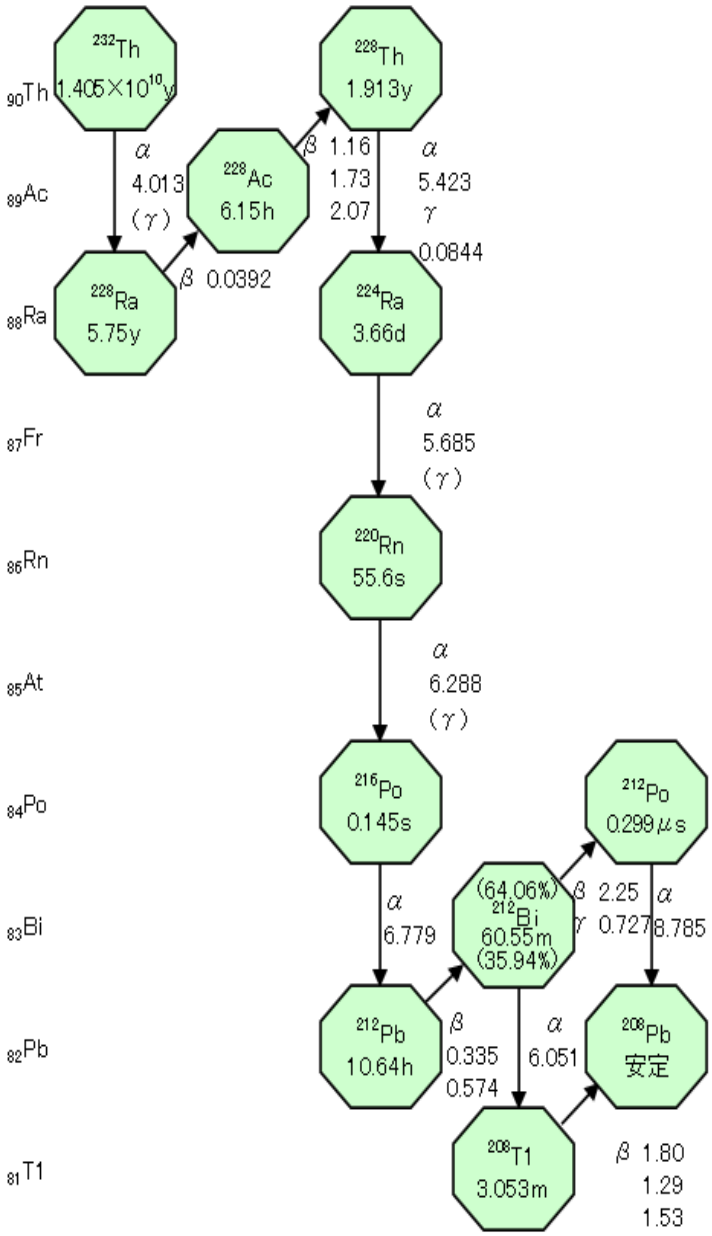

Figure 8.5: Thorium chain [76]

The amount of the ^{85}Kr also can be estimated from the real data using a delayed coincidence technique using the advantage of the FADC. Because the time window of FADC is set to 10 μs, the detection efficiency of sequential two events of ^{85}Kr decay is high sufficiently. After the refurbishment, we obtained a finite value for the abundance of ^{85}Kr as follows. In order to select Kr events, The following seven cut-conditions were applied; 1)ID-trigger cut, 2)Number of hit PMTs>=4, 3)Difference of time from the previous event< 10 ms, 4)TDC-RMS cut, 5)Cherenkov cut, 6)0.6μs <Difference of time between the two peaks< 5 μs, 7)10 keV<Energy of the 1st event<150 keV, 8)400 keV< Energy of the 2nd event<650 keV, 9)Reconstructed radius of the 1st events<38 cm.

As a result of the analysis using 512.7 days normal run data after the detector refurbishment, 22 events remained. Taking into account the signal efficiency of 0.398, the abundance was estimated to be 0.26±0.07 mBq/detector (6.9±2.9ppt).

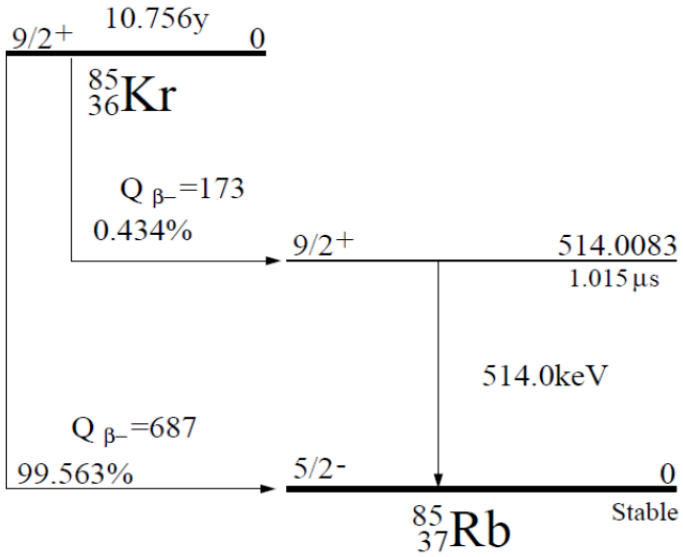

Figure 8.6: Decay scheme for ^{85}Kr

8.2.4 ^{39}Ar

100% of ^{39}Ar decay to ^{39}K by β decays (Q=565 keV) as shown in Fig. 8.8. The half time is 269 years. This beta spectrum can interrupt the search for WIMPs and hidden photons. We measured impurities in a xenon sample taken from the XMASS detector with our gas chromatography. However, Ar can not be separated from O_2 because their peak positions are too close each other. Therefore, an upper limit of 0.33 ppm for Ar was estimated from O_2 value. If the natural abundance of ^{39}Ar is assumed (8×10^{-16}), the abundance results in 83 μBq/detector.

8.2.5 $2\nu\beta\beta$ from ^{136}Xe

Double beta decay is a type of beta decay process where a nucleus releases two β-rays as a single process. Although about 60 types of isotope can decay emitting two electrons,

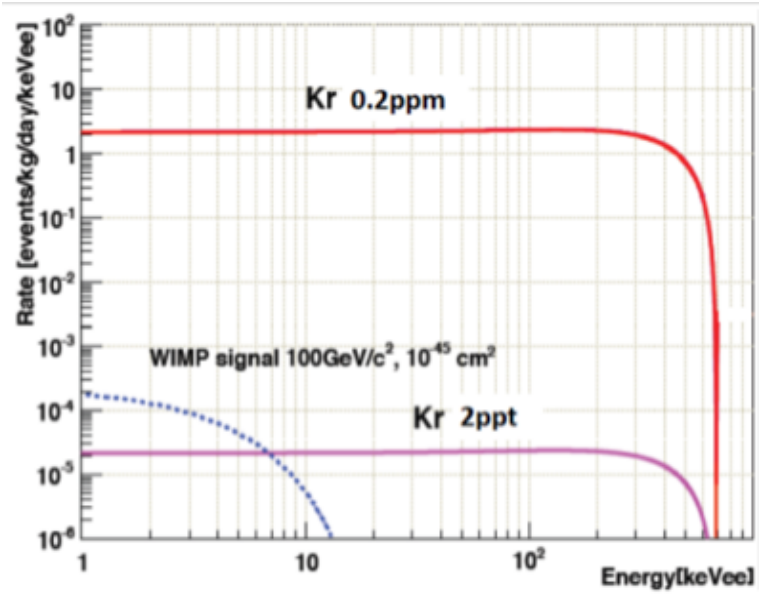

Figure 8.7: Energy spectrum for ^{85}Kr with 100 GeV WIMPs signal

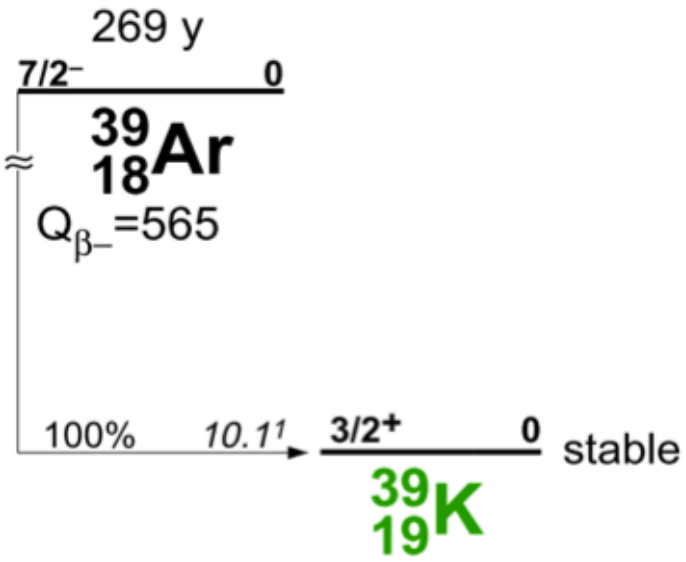

Figure 8.8: Decay scheme for ^{39}Ar

only 11 types of double beta decays have been observed in the past. Contrarily, double beta decays without neutrino emissions ($0\nu\beta\beta$) are widely searched for because the fact proves neutrinos are majoron particles. ^{136}Xe is included in the natural xenon at a rate of 8.86%. Double beta decays from the ^{136}Xe can become a BG component of XMASS experiment. The decay process can be written as,

$$(2\nu\beta\beta) \quad {}^{136}Xe \rightarrow {}^{136}Ba + 2e^{-} + 2\bar{\nu}_e. \tag{8.3}$$

KamLAND-Zen is a liquid xenon scintillator experiment aiming to detect $0\nu\beta\beta$ events using 90.93% enriched ^{136}Xe. The target xenon is contained in a 3.08 m diameter spherical inner balloon. They measured $2\nu\beta\beta$ half-life of ^{136}Xe with the lowest errors. The value is $\tau^{2\nu}_{1/2} = 2.38 \pm 0.02(stat) \pm 0.14(syst) \times 10^{21}$ years [77]. The obtained energy spectrum and the simulated BG components of KamLAND-Zen experiment are shown in Fig. 8.9 (left). The expected energy spectrum of $2\nu\beta\beta$ in the R<30 cm fiducial volume of XMASS detector assuming $\tau_{1/2} = 2.38 \times 10^{21}$ years is shown in Fig. 8.9 (right).

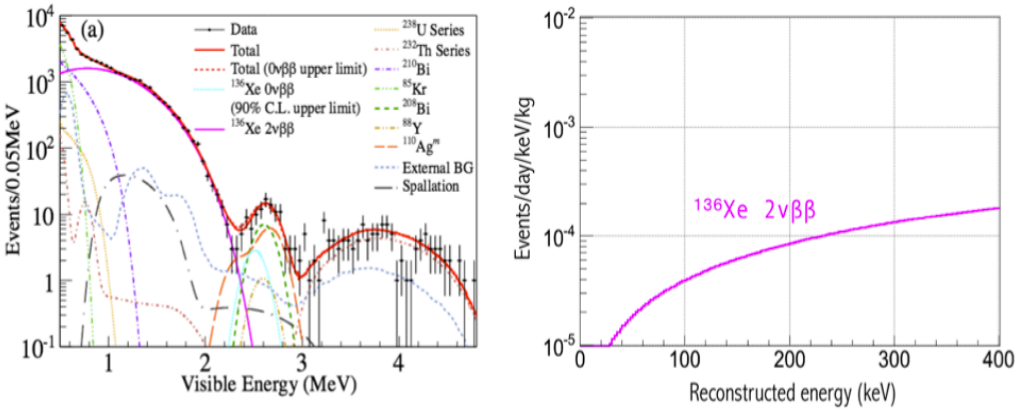

Figure 8.9: Energy spectrum and BG components of KamLAND-Zen experiment (left) [77]. Expected energy spectrum of $2\nu\beta\beta$ in the R<30 cm fiducial volume of XMASS detector (right). $\tau_{1/2} = 2.38 \times 10^{21}$ years is assumed.

8.2.6 Energy spectrum composed of the inner background

In this section, we mentioned the amount of inner BGs which could directly affect the HPDM search and their measurement methods. Figure 8.10 shows an expected energy spectrum by the BG MCs mentioned here. The left figure shows a stacked energy spectrum. The right figure shows a non-stacked energy spectrum. The red line indicates the sum of all the BG components. Although only the amount of the ^{39}Ar is an upper limit, the amounts of ^{214}Pb, ^{85}Kr, and $2\nu\beta\beta$ are of the same order of magnitude. Actually, these BG components can not explain all of the observed energy spectrum expressed by a black dash line. The components not mentioned here will be explained in Chap. 11.

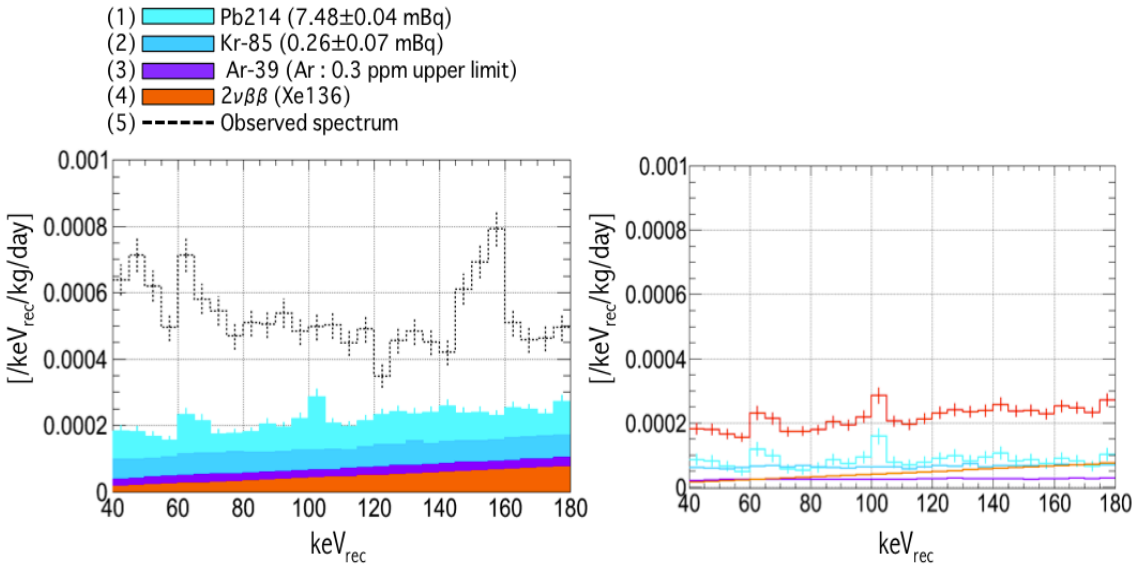

Figure 8.10: Expected energy spectrum by the BG MC.

8.3 Radioactive contamination in PMT aluminum seal

The event rate in the commissioning run of XMASS experiment was unexpectedly large. According to the result of the analyses conducted during the commissioning run [55], the unexpected BG component was attributed to the surface events caused by the detector materials. Sealing materials made from aluminum (Fig. 9.1 in Chap. 9) between the PMT body and its window are directly attached to the xenon sensitive region. Beta-rays and γ-rays from the radioactive isotopes contaminated in the aluminum seals deposit their energy to the liquid xenon. If the deposit position is in front of the PMT window, we can easily identify the events by the PMT hit pattern. On the other hand, the events whose deposit position is blind angle from the PMTs, the identification is very difficult, because the p.e. information is reduced. These events can result in vertex mis-reconstruction. We measured the contribution of low energy γ-rays from the aluminum seal by a High-Purity Germanium (HPGe) detector and found significant amounts of ^{238}U, ^{214}Pb and, ^{234}Th.

Figure 8.11 shows the full volume energy spectrum of the real data taken during the commissioning run and the BG MC including the contribution of the aluminum seals. The horizontal axis is a p.e. proportional energy scale scaled by a ^{57}Co energy peak. The expected BG level estimated by the MCs and the observed data have a good agreement with the level of $\sim$1 keV^{-1}day^{-1}kg^{-1}. The expected radioactive intensity for each isotope were modified to match in the error of the result by HPGe detector measurement. We conducted a detector refurbishment to handle this issues. The detail and its result will be described in Chap. 9.

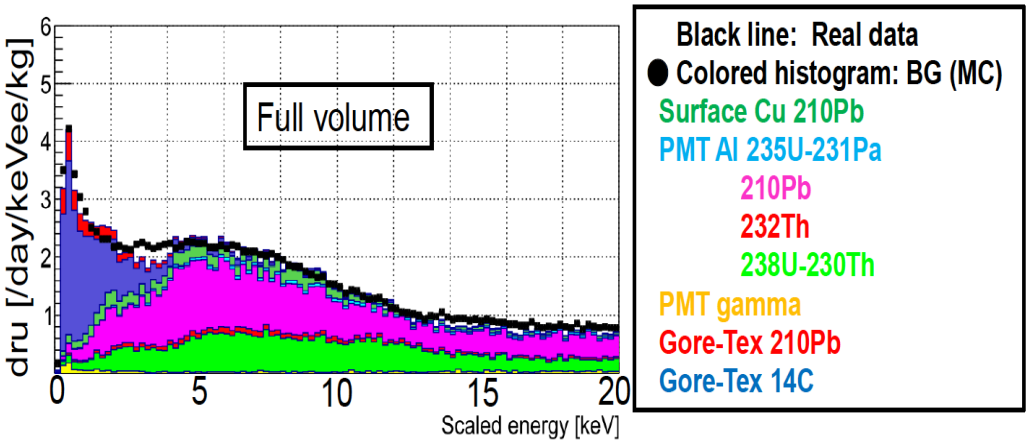

Figure 8.11: Energy spectrum of the commissioning run and the BG MC

Chapter 9

Detector Refurbishment

After the first run of XMASS in 2011, we found unexpected backgrounds are contaminated in the data. As a result of the comparison between the data and BG MC simulations and the measurements of samples by HPGe detector, we concluded that β-rays and γ-rays from mainly Al parts which are sealing materials between PMT quartz and PMT body are contaminating unexpected largely to the data. Figure 9.1 (left) shows the aluminum parts of a PMT which including radioactive contamination.
We implemented a detector refurbishment work in the period of May, 2012 through November, 2013. On the parallel with the dismantlement and the re-construction of the detector, we worked for reduction of the radioactivity and developing of the radioactive shields. The main issues are four topics below and explained in this chapter.

1) Radioactivity in the aluminum materials in the PMTs

2) Scintillation events in the gap region

3) Surface BG

4) Fluorocarbon polymer

9.1 The issues and the countermeasures

9.1.1 Radioactivity in the aluminum materials in the PMTs

An aluminum part which seals between a PMT quartz and a PMT body contaminates unexpected amount of radioactive contaminations. We determined not to rebuild PMTs from the manufacturing stage. Instead, we developed several shielding materials for α-rays, low energy γ-rays, and scintillation lights using the combination of aluminum evaporation and copper rings and plates. The side of a PMT was evaporated by an high purity aluminum to prevent scintillation photons generated in a gap between PMTs being leaked into the XMASS sensitive region as shown in Fig. 9.2.

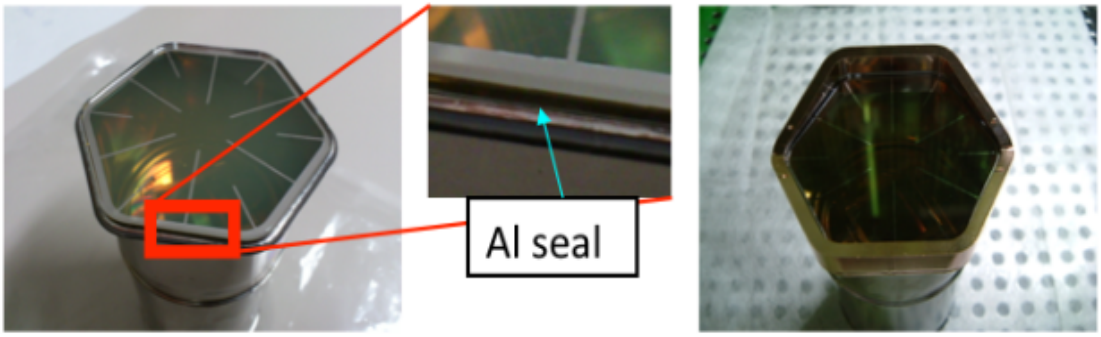

Figure 9.1: The aluminum seal including radioactive contamination and its closeup picture (left). A copper ring mounted on a PMT (right).

9.1.2 Scintillation events in the gap region

The most advantageous point for XMASS experiment is the self shielding capability. We can achieve low BG data using only fiducial volume of the center of the detector. The vertex reconstruction is very important to accomplish this goal. We estimate the event vertex using photoelectron (P.E.) information of each PMT. However, the events which are caused in the blind areas against the near PMTs cause unexpected P.E. patterns and can be reconstructed in wrong position. An example of the gap event simulated by MC is shown in Fig. 9.3. In order to avoid this situation, the gaps between PMTs were reduced by the fillers of the copper rings and the lights generated between the copper rings are also shielded by the copper plates. The cross section of newly installed parts are shown in Fig. 9.2 and the inner view of the refurbished detector is Fig. 9.4.

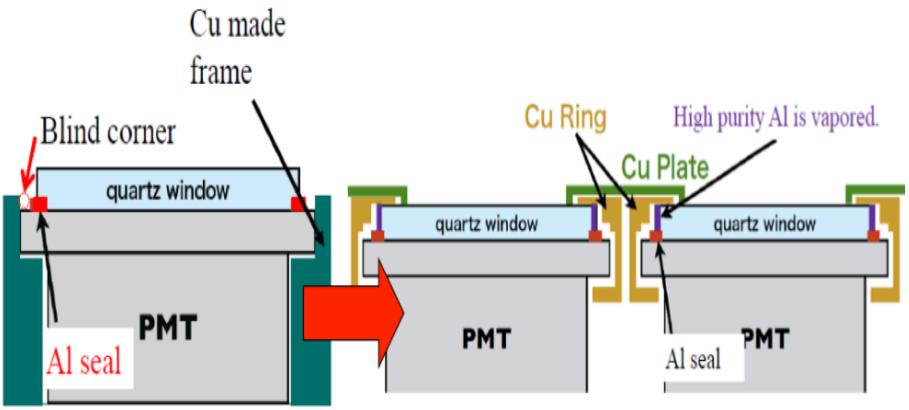

Figure 9.2: cross section of PMTs. The high purity aluminum evaporation, the copper ring, and the copper plate are newly developed for the BG reduction.

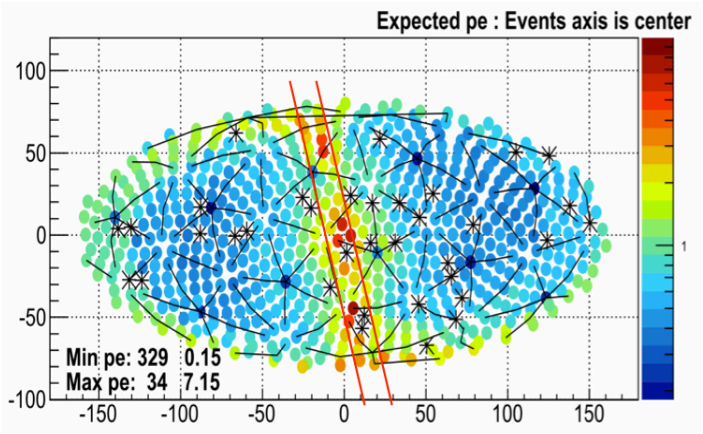

Figure 9.3: A P.E. pattern of a gap event simulated by MC.

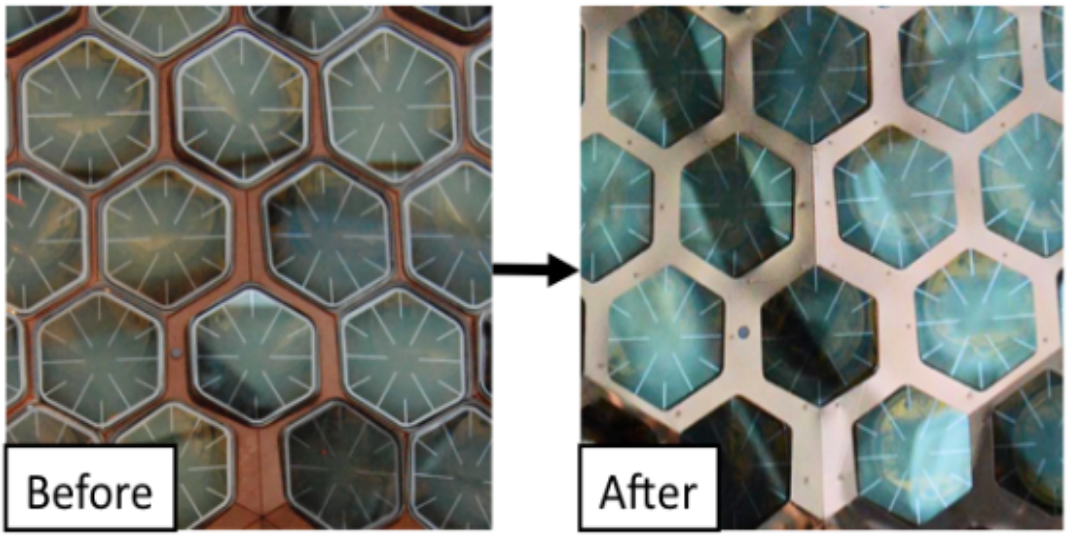

Figure 9.4: The inner view of the XMASS detector before and after the refurbishment.

9.1.3 Surface background

We also struggled to minimize the surface radioactive contaminations, such as ^{210}Pb and ^{210}Po. The electrical polishing for the ready-made copper surfaces of the PMT holder were applied. The ratio of the radioactivity of ^{210}Pb and ^{210}Po reduced <0.1 and <0.0034, respectively. The clearance method for the surface of the PMTs are also developed and implemented to all 642 PMTs. We rinsed the PMTs with 1mol/l nitric acid for 4 minutes each PMTs. The reduction rate for ^{210}Pb was evaluated to be $\sim 70\%$ by the measurement of α-ray. The pictures of the electrical polishing work and the photocathode cleaning work are on Fig. 9.5, Fig. 9.6 respectively.

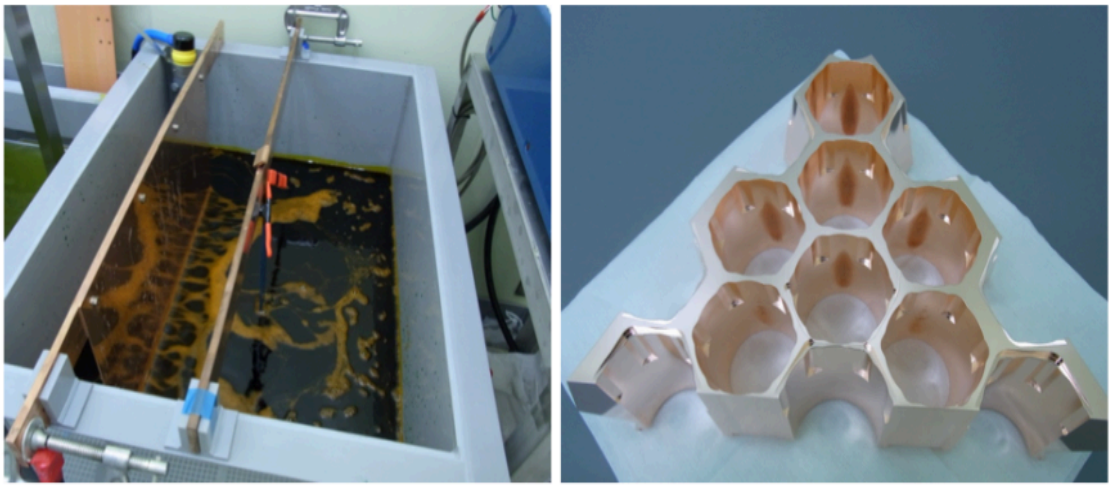

Figure 9.5: The electropolishing bath (left) and the picture of a PMT holder after the polishing (right).

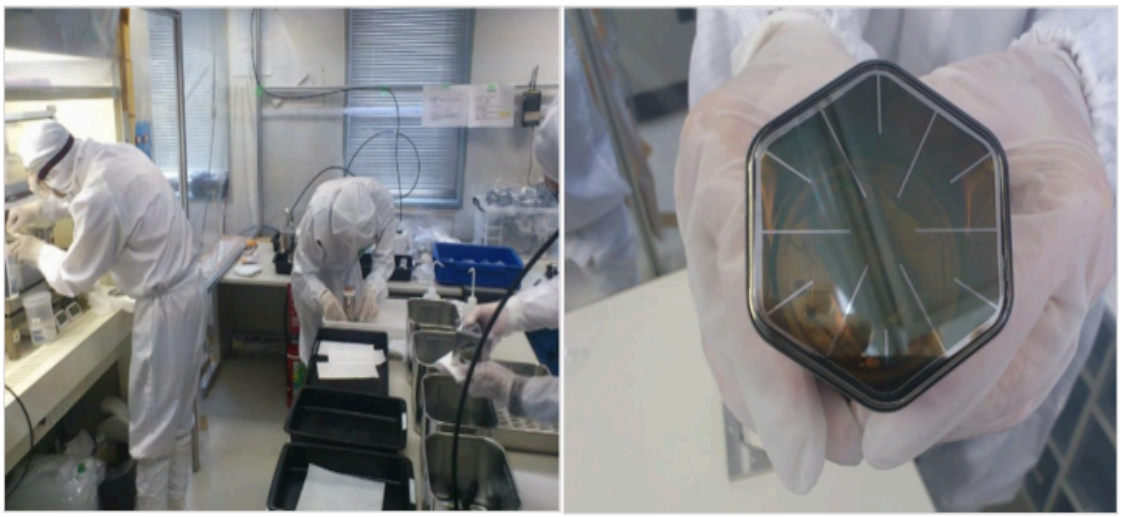

Figure 9.6: The PMT cleaning work using nitric acid (left) and the picture of a PMT after the cleaning (right).

9.1.4 Fluorocarbon polymer

The fluorocarbon polymers were used for buffers between the PMT and the PMT holder. However it was very difficult to evaluate the physical property because of their large uncertainty. They were removed at the refurbishment.

9.2 Background level of before and after the refurbishment

The physical run to search for dark matter resumed in Nov. 2013 after the refurbishment work. Figure 9.7 shows the comparison of the BG level before and after the refurbishment for the low energy region. The standard noise reduction and cherenkov-like event reduction were applied on both of them (The details are explained in Chap. 10). We succeeded approximately 1/10 reduction at around 5 keV$_{ee}$ energy region. The parameter of the maximum P.E. divided by the total P.E. of 642 PMTs (maxPE/totalPE) have information about the position of the events. The event which occurred in front of the PMTs have large maxPE/totalPE. On the other hand, the events which occurred at the blind corner from the PMTs have smaller maxPE/totalPE because the nearest PMT can not catch the photons due to the sharp incident angle. Figure 9.8 shows the maxPE/totalPE distributions depending on the energy for the commissioning run data and the data after the refurbishment. The "Gap" events greatly reduced after the refurbishment as we had expected.

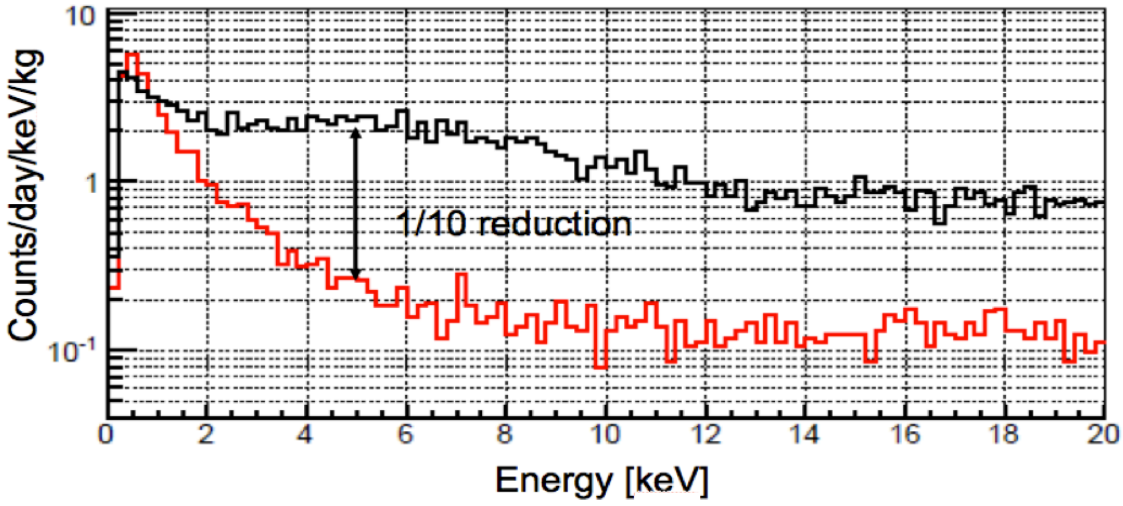

Figure 9.7: BG level before (black) and after (red) the detector refurbishment below 20 keV.

On the other hand, the BG level of the higher energy region used in this thesis is described below. Table 9.1 shows the comparison of the BG levels at around 100 keV$_{ee}$ before and after the detector refurbishment. The fiducial volume cut of 15 cm for the commissioning data and 30 cm for the data after the refurbishment was applied. Actually, the BG level after the refurbishment (5.0×10^{-4} dru) is worse than that before the refurbishment (1.4×10^{-4} dru) [2]. The BG level in the commissioning phase was

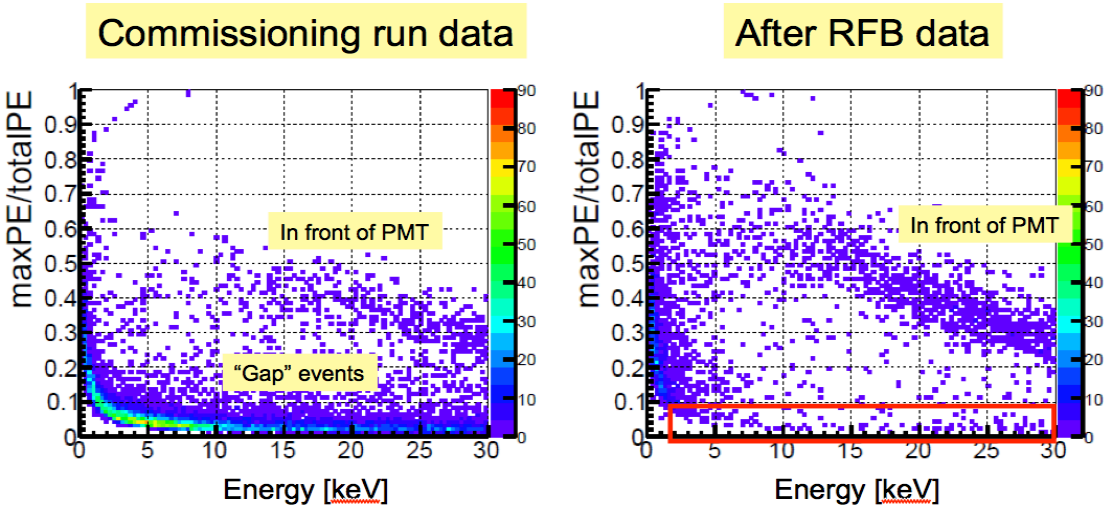

Figure 9.8: max pe/total pe distributions

consistent with the component contributed by ^{214}Pb distributed uniformly in the liquid xenon. We need to assume additional BG components to explain the increased BG level. However, we were able to store a much larger data by enlarging the fiducial volume as a result of the detector refurbishment. As a result, we succeeded to keep the statistical error low and increase the sensitivity if we apply a BG subtraction.

	XMASS-CM	XMASS-RFB
BG level	1.4×10^{-4} (dru)	5.0×10^{-4} (dru)
Statistic	5.4 (ton·day)	82.9 (ton·day)
Statistical error on each 1 keV$_{ee}$ bin	$\pm1.6\times10^{-4}$ (dru)	$\pm0.8\times10^{-4}$ (dru)

Table 9.1: Comparison of the BG levels at around 100 keV$_{ee}$ before and after the detector refurbishment. (dru) = (/keV$_{ee}$/day/kg).

Chapter 10

Analysis of HPDM absorption

10.1 MC simulation for HPDM absorption

As discussed in Chap. 5, an HPDM interacts with electrons by axio-electric effect and deposits their all energy including their rest mass. HPDM signals are simulated by injecting γ-rays uniformly in the active volume of the liquid xenon with a gamma energy corresponding to the rest mass of the particles. The MCs are generated with the mass from 50 keV/c^2 to 120 keV/c^2 by 2.5 keV/c^2 steps. This procedure is reasonable because it is identical for γ-rays and HPDMs to deposit their energy including their rest mass to electrons at these low energies, albeit with different coupling constant in Eqs. 5.1. The energy spectra simulated by this procedure are shown in Fig. 10.16.

10.2 Data reduction

The data used in this analysis were taken from November, 2013 to December, 2014 after the detector refurbishment. The total live-time is 268.9 days. The data taking was conducted in a stable condition during the period. The dedicated run quality check was done in order to remove noise events, such as extensive PMT noise, unstable pedestal levels, and abnormal trigger rates. After the refurbishment, neutron calibrations were implemented two times. Because the runs after the neutron calibrations are expected to have events stemming from the activations of xenon nuclei, 10 days of runs after the calibration were removed to reduce these impacts. As mentioned in Chap. 7, the dominant components of the events are electric noise events and background (BG) events due to γ-rays from PMTs. The dedicated event reduction procedure was developed and applied to reduce these impacts. The details of the procedure of the event reductions and the signal acceptances are discussed below.

10.2.1 Cut (1); Pre-selection

A pre-selection is based on the ID trigger, the time difference between a event and next to it, and RMS of hit timing distribution. These selections are applied to remove events by electronics or detector artifacts.

ID-trigger cut

We have four different trigger identification flags (ID, OD, LED, and GPS trigger). Only ID-trigger events are used for the dark matter search. High energy cosmic ray events are reduced by this trigger selection. The total photoelectron (P.E.) spectra before (black) and after (red) the ID-trigger selection are shown in Fig. 10.1.

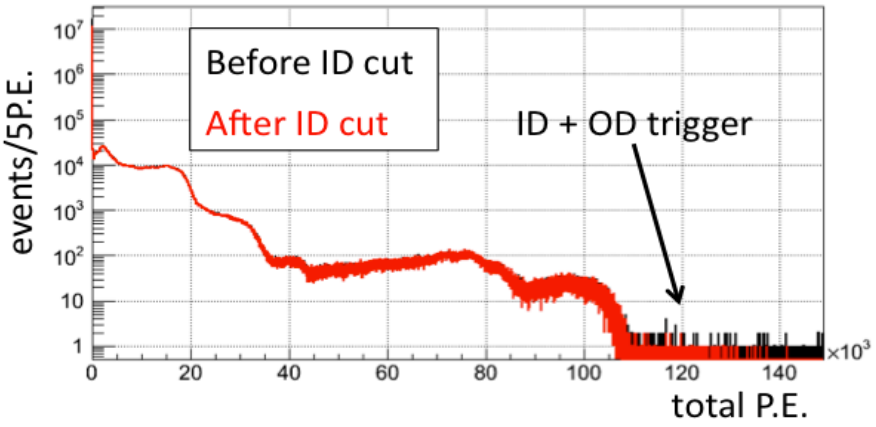

Figure 10.1: Total P.E. spectra before (black) and after (red) ID-trigger cut

dT-pre/post cut

The events have trigger timing information stamped by a TRG module. The events whose differential time to the previous events (dT-pre) are short are dominated by after-pulses which arise after bright events, and the events whose differential time to the post events (dT-post) are short are dominated by Bi-Po sequential events of radon daughters. The events whose dT-pre or dT-post is less than 10 ms are removed. The higher energy events, such as α-rays, which are accompanied by large after-pulses are also removed by this procedure. The total live-time reduce by 6.0% due to this process. dT-pre and dT-post distributions are shown in Fig. 10.2. The right side of the red arrows pass these reduction. Figure. 10.3 shows the total P.E. distributions before and after the dT cut. The total live time after the dT cut results in 252.9 days.

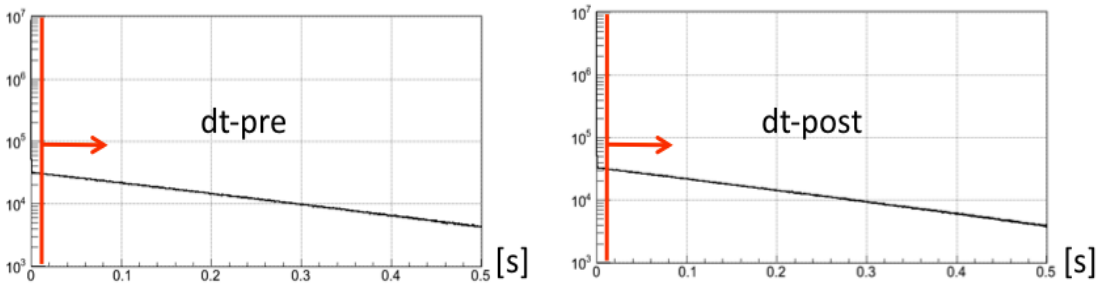

Figure 10.2: dT-pre cut (left) and dT-post cut (right) distributions

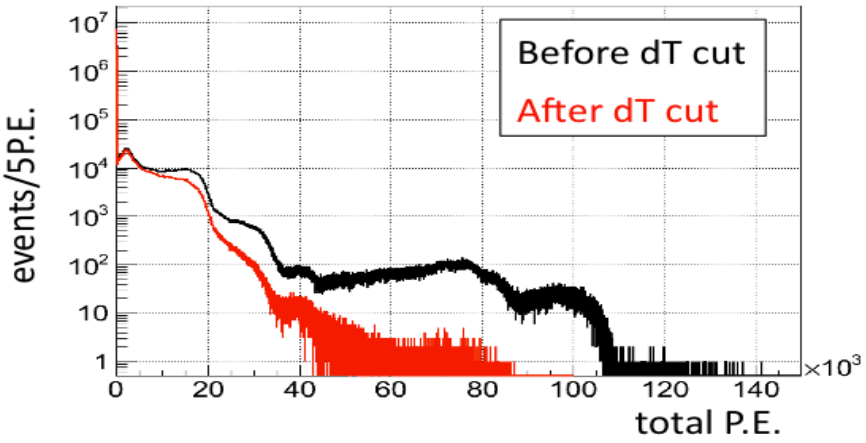

Figure 10.3: Total P.E. distributions before (black) and after (red) the dT-pre and dT-post cut

TDC-RMS cut

After-pulses and other electric noises enlarge the TDC distribution of an event. The events whose TDC-RMS is more than 100 ns are removed. Figure 10.4 shows the distributions of TDC-RMS of the observed data and the simulation of 80 keV/c^2 HPDM. The signal acceptance is not significantly affected by this cut. The total P.E. distributions before and after the TDC-RMS cut is shown in Fig. 10.5.

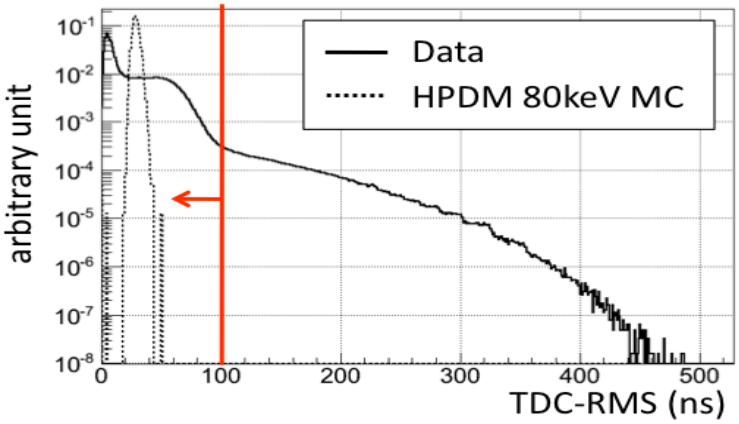

Figure 10.4: TDC-RMS distributions of the data and the simulation of 80 keV/c^2 HPDM

10.2.2 Cut (2); Fiducial volume cut

As discussed in Chap. 6, the main idea of XMASS detector is self shielding against γ-ray BGs caused by the detector materials and outer environments, and exploiting the events generated in the detector center. We applied a fiducial volume cut based on a reconstructed vertex mentioned in Chap. 6. Figure 10.6 shows the reconstructed radius

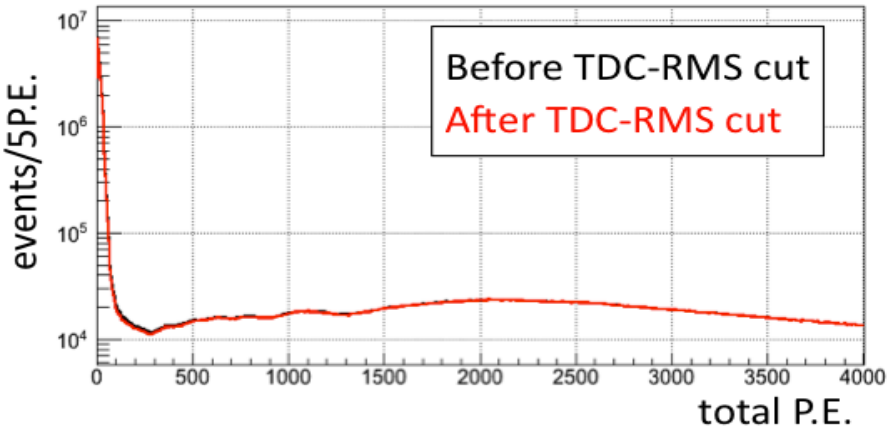

Figure 10.5: Total P.E. distributions before (black) and after (red) the TDC-RMS cut.

distributions and the radius cubed distributions for the events of all energies and those of the reconstructed energy region of our interest (40 - 120 keV$_{rec}$).

We can see some spike structures in the R cubic distribution of the energy between 4 hits and 3000 p.e. This structures have roots in very low p.e. events. The same structures can be reproduced by our MC simulation. We need to handle the effect in a competent way if we use the reconstructed vertex of low p.e. events. We don't need to consider the effects this time because the minimum energy of our interest is sufficiently high. We can also see some spike structures in R cubic distribution of 80 keV/c^2 signal MC. This pattern is caused by the events reconstructed near the wall side grids. This effects are small for the detector inner events.

For the radius cubed distribution of the events whose energy is between 40 keV and 120 keV$_{rec}$, the distribution inner than 30 cm is almost flat. Therefore, the event rate is almost constant regardless of the cut position of the fiducial volume as long as R <30 cm. On the other hand, the outer gamma ray BGs leak into the fiducial volume if R >30 cm as described in Fig. 6.8. We adopted R <30 cm as a fiducial volume in this analysis in order to maximize the number of the samples. The radius and radius cubed distributions of 80 keV/c^2 HPDM signal MC are shown in Fig. 10.7. The signal efficiency is obtained by a signal MC, and defined as the number of events remaining after the fiducial volume cut divided by the total signal events generated in the fiducial volume by the MC. Gamma-ray events are generated uniformly in the xenon active volume (R < 40 cm). Both "leak in" and "leak out" can be considered due to uncertainties of the vertex reconstruction program by this definition (An event generated outside R = 30 cm may be reconstructed inside R = 30 cm, and vise versa.). The signal efficiency can be larger than 100% for this reason. The signal efficiency of the 80 keV/c^2 HPDM after the pre cut and the fiducial cut is 99.3%. The signal efficiencies of the other HPDM mass are shown in Tab. 10.1.

The number of the events after each reduction step are summarized in Tab. 10.2.

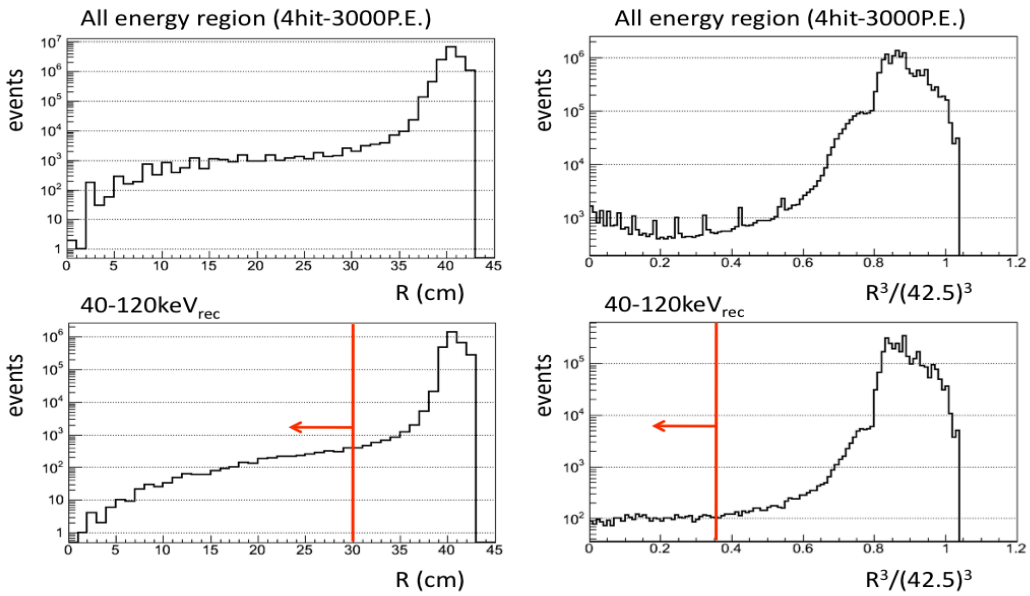

Figure 10.6: The left figures show the reconstructed radius distributions for total energy (upper) and between 40 - 120 keV$_{rec}$ energy region (lower). The right figures show the radius cubed distributions respectively.

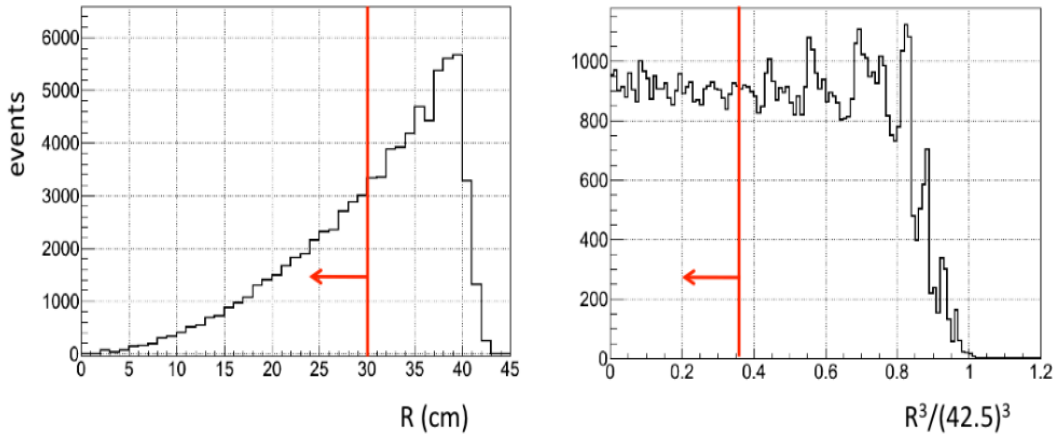

Figure 10.7: The reconstructed radius and radius cubed distribution for 80 keV/c^2 HPDM MC

HPDM mass (keV/c^2)	50	55	60	65	70	75	80	85
efficiency(%)	101.3	100.6	100.2	99.9	99.7	99.6	99.3	99.2

HPDM mass (keV/c^2)	90	95	100	105	110	115	120
efficiency(%)	99.1	99.0	98.9	98.7	98.8	98.5	98.8

Table 10.1: Signal efficiencies after the fiducial volume cut for each HPDM mass

Reduction condition	Number of events
Total events	112,920,245
ID trigger	79,369,575
dT-pre $>$ 10 ms	68,265,131
dT-post $>$ 10 ms	58,581,045
TDCRMS $<$ 100 ns	57,472,404
4 hit - 3000 P.E. (For reconstruction P.E. range)	13,874,910
$R <$ 30 cm	24,668

Table 10.2: The number of events after each reduction step.

10.3 Energy scale correction

10.3.1 time variation correction

We have frequently (almost once a weak) taken ^{57}Co inner calibration data in parallel with the normal physical data taking in order to check the detector stability. We observed P.E. yield changes as shown in Fig. 10.8 (top). This changes can be separated into the three components: Gradual changes from the beginning of the run, Sudden drop at the power failure (Aug. 17th, 2014), and Rapid changes at the swaps of the cold-heads in the XMASS refrigerator (Dec. 24th 2014, Jun. 7th, 2015, and Jun. 22nd, 2015). During all the period, environmental parameters, such as pressure and temperature, were measured. We also occasionally measured H_2O and other gas impurities by a dew-point meter and a gas chromatography, respectively. According to the MC simulation, the observed P.E. changes can be explained by changing the absorption length parameter (second top in Fig. 10.8). On the other hand, other parameters, such as the amount of intrinsic scintillation emission and the scattering length are not dominant factors as shown in the bottom two figures in Fig. 10.8. The cause of the absorption length changes can be explained by gaseous impurity contaminated in the liquid xenon. Water is one of the candidates for this impurities but the processes are not fully understood. We removed the data taken in the week when the power failure happened because the change of the absorption length is rapid. The periods including the swaps of the cold-heads are out of the data period used in this analysis. The more details for the evaluation and the treatment of the change of the absorption length are in [78].

Because we are using a fixed absorption length parameter (600 cm) for the event

reconstruction, we need to treat the effect of the change of the parameter adequately. For reconstructed energy, this changes were scaled by using the weakly taken ^{57}Co calibration data (Z = 0 cm) based on the first ^{57}Co data (Nov. 22nd, 2013). The mean values of the reconstructed energy were obtained by the fittings of a crystal ball function to the energy distributions. The definition of the crystal ball function is Eqs. 10.1.

$$
\begin{aligned}
f(x;\alpha,n,\bar{x},\sigma) &= N \cdot \begin{cases} \exp(-\frac{(\mathrm{x}-\bar{\mathrm{x}})^2}{2\sigma^2}), & \text{for } \frac{\mathrm{x}-\bar{\mathrm{x}}}{\sigma} > -\alpha \\ A \cdot (B - \frac{x-\bar{x}}{\sigma})^{-n}, & \text{for } \frac{\mathrm{x}-\bar{\mathrm{x}}}{\sigma} \leq -\alpha \end{cases} \\
A &= (\frac{n}{|\alpha|})^n \cdot \exp(-\frac{|\alpha|^2}{2}) \\
B &= \frac{n}{|\alpha|} - |\alpha|
\end{aligned}
\tag{10.1}
$$

Where, n and α are free parameters and adjusted to fit to the distribution well. The scale factors at the periods between the calibrations were obtained by linear interpolation as shown in 10.9. The remained deviations at the other radius positions are taken into account as systematic errors and discussed in the later section. For reconstructed position, the impact will also be evaluated and discussed in the later section. The energy spectra of the real data after pre-cut and the fiducial volume cut are shown in Fig. 10.10. The horizontal axis is reconstructed energy.

10.3.2 $\mathrm{keV_{rec}} \rightarrow \mathrm{keV_{ee}}$ scale correction

Generally, intrinsic scintillation light efficiency of liquid xenon (Number of photon per keV) depends on dE/dx and have energy non-linearities. Although our reconstructed energy scale is basically including this energy non-linearity model, the model is not perfect. For this incompleteness, we define the 122 keV peak of the ^{57}Co in the reconstructed energy scale as 122 keV_{ee}. The absolute energy scale of the MC is also adjusted at 122 keV_{ee}. The keV_{ee} energy scale is obtained by using three energy peaks (17.8 keV and 59.5 keV of ^{241}Am, and 122 keV of ^{57}Co) and their interpolation. The systematic difference of the energy scale between the data and the MC due to the imperfect modeling of the non-linearity in MC is estimated in the later section. Figure 10.11 shows the conversion function from reconstructed energy (keV_{rec}) to the intrinsic deposit energy (keV_{ee}). We also have 5.9 keV of ^{55}Fe and 87.7 keV of ^{109}Cd as calibration sources. However, the geometries of these calibration sources are different from those of ^{57}Co and ^{241}Am calibration sources as shown in Fig. 7.3 and Fig. 7.4. Hence the total photo-electron and the reconstructed energy tends to be low by the shadow effects due to the geometry. We don't use these calibration sources here to obtain a energy correction factor. The energy spectra of the real data after the time variation correction and the $\mathrm{keV}_{rec} \rightarrow \mathrm{keV}_{ee}$ scale correction is in Fig. 10.12.

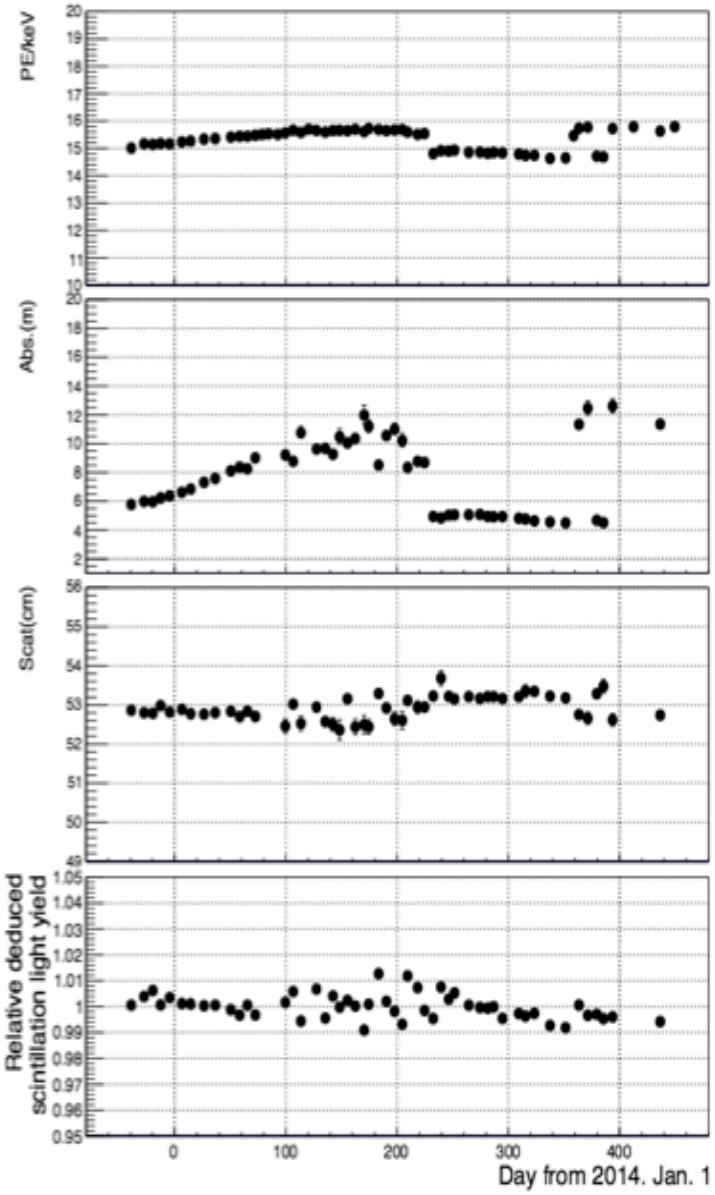

Figure 10.8: Time variations of P.E. Light yield, absorption length, scattering length, and intrinsic light yield changes.

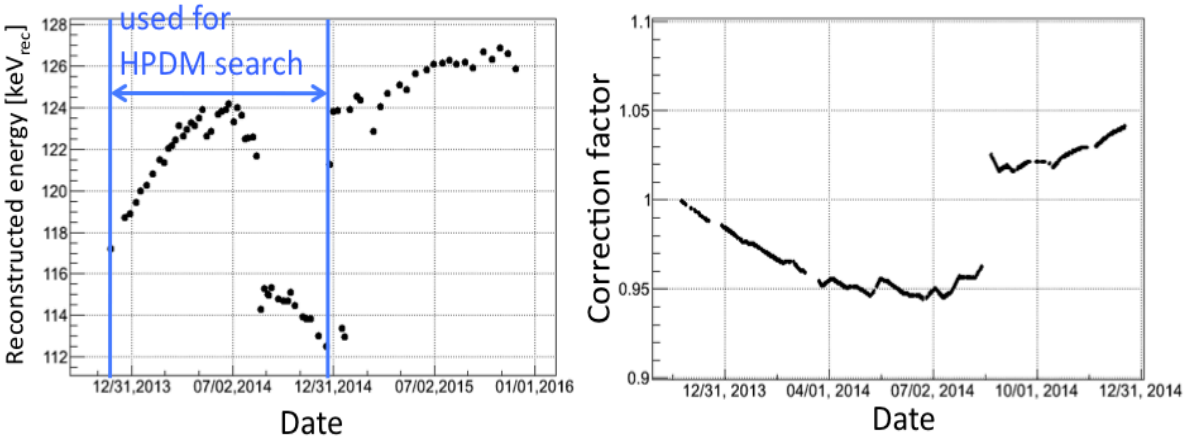

Figure 10.9: Time variation of reconstructed energy of the peak of the ^{57}Co inner source calibration data ($Z = 0$ cm) and corrections factor derived by the data.

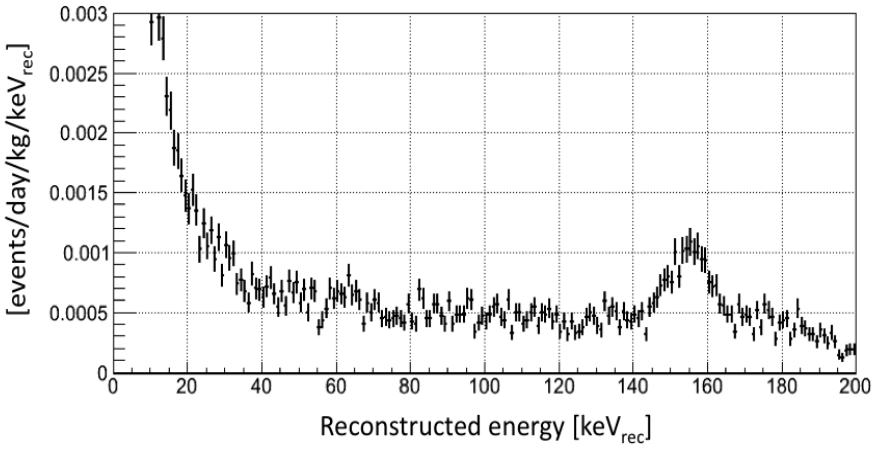

Figure 10.10: Energy spectrum after both of the pre-cut and the fiducial volume ($R < 30$ cm) cut

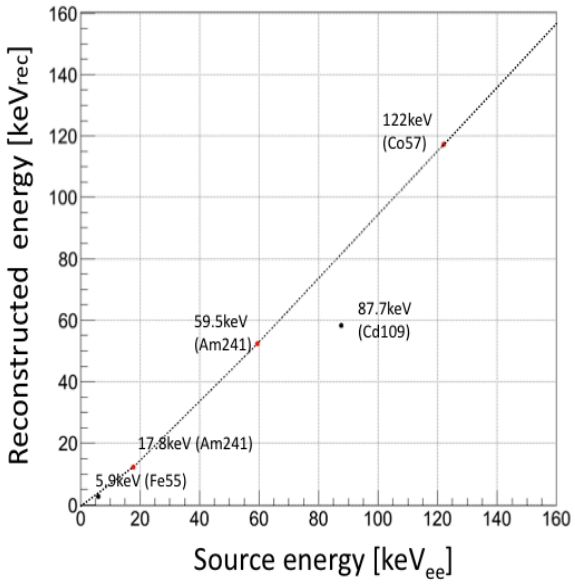

Figure 10.11: Conversion function of energy scale from reconstructed energy to intrinsic deposited energy in LXe.

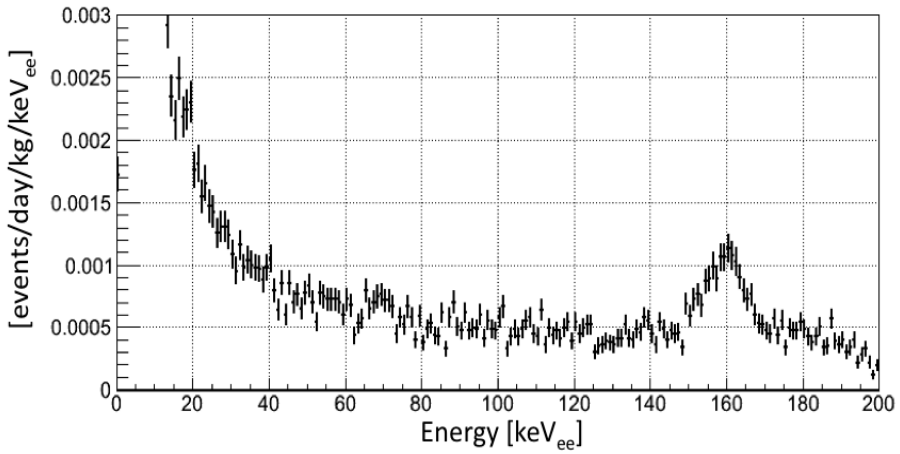

Figure 10.12: Energy spectrum after pre-cut and fiducial volume ($R < 30$ cm) cut after the time variation and the keV$_{rec}$ $\rightarrow$ keV$_{ee}$ correction.

10.4 ^{131m}Xe peak

We can clearly see a peak around 160 keV$_{ee}$ in the energy spectrum of the real data. This peak was caused by γ-rays by decays from ^{131m}Xe nucleus created by neutron captures. Because of the neutron calibrations conducted in Dec. 17, 2013 and Mar. 12, 2014, ^{131m}Xe activated from ^{130}Xe are generated. Table 10.3 shows the properties of activations of the xenon nucleus. Figure 10.13 shows decay schemes of ^{131m}Xe (^{131}I).

RI	Natural abundance (%)	Created	Half-time (day)	Cross section (barn)
^{130}Xe	4.07	^{131m}Xe	11.8	0.45

Table 10.3: Properties of the activations of ^{130}Xe

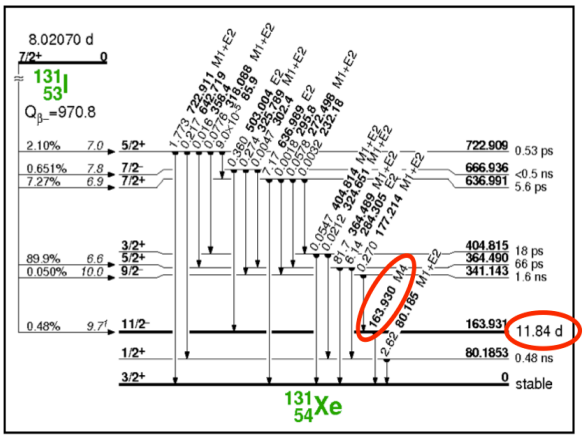

Figure 10.13: Decay schemes of ^{131m}Xe (^{131}I).

Figure 10.14 shows the stability of the event rate of three different energy ranges. We separate our total data set to 17 terms. The green points with errors indicate the event rate of the energy range from 40 to 90 keV$_{ee}$, the black points with errors indicate the event rate of the energy range from 90 to 140 keV$_{ee}$, and the red points with errors indicate the event rate of the energy range from 140 to 180 keV$_{ee}$. We can see that the event rate of the beginning of the run (#1) and after the neutron calibration run (#2,6) of the energy range from 140 to 180 keV$_{ee}$ are relatively higher than the other terms. Even though we removed the data set for 10 days after the neutron calibration, the peak seems to be still remaining. We did not remove these data set (#1,2,6) from the final data set because the event rates of our interest (40-140 keV$_{ee}$) are not significantly changed in these terms. Additionally even if we concentrate only after #7, the event rates of energy region from 140 to 180 keV$_{ee}$ are systematically higher than that of energy region from 90 to 140 keV$_{ee}$. Actually, we can see a peak around 160 keV$_{ee}$ in the energy spectrum of only after #7 as shown in Fig. 10.15. The cause of the activations is briefly mentioned in Chap. 11, but the actual mechanism is under study.

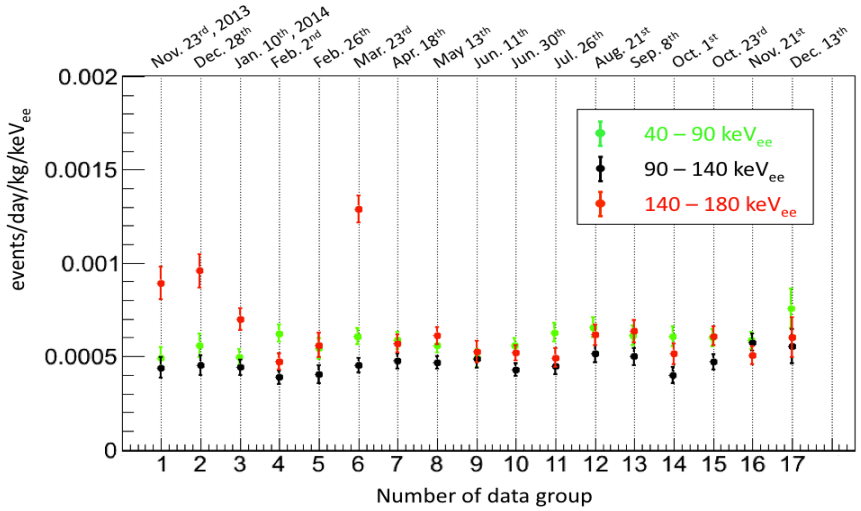

Figure 10.14: Event rate stabilities for three energy region; 40 - 90 keV$_{ee}$ (green), 90 - 140 keV$_{ee}$ (black), 140 - 180 keV$_{ee}$ (red).

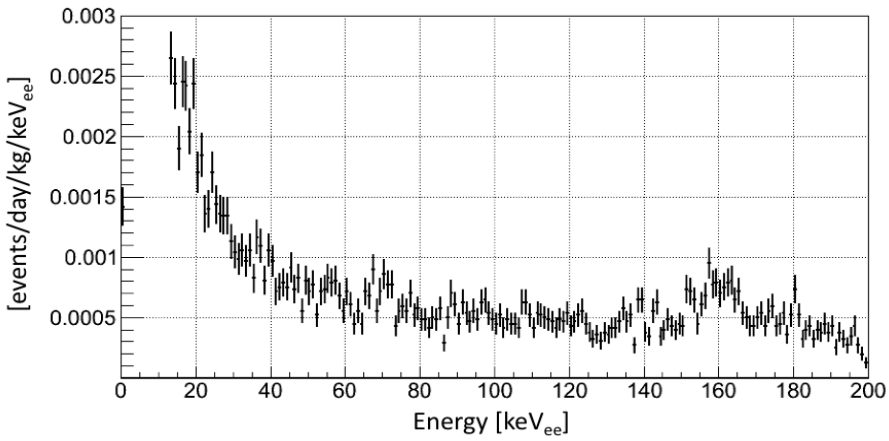

Figure 10.15: Energy spectrum of only after #7.

10.5 Peak finding

The large fiducial volume of $R \leq 30$ cm enables us to search for HPDMs with a large sample. Besides, the energy spectrum in the energy region of our interest is relatively flat. Therefore, we search for HPDMs by means of peak finding method assuming that the BG spectrum can be described by "exponential + constant (+ gaussian)" function (assuming that the component is composed predominantly of β-rays) in the energy region from 30 keV$_{ee}$ to 180 keV$_{ee}$. The peak of ^{131m}Xe is modeled by the last gaussian function. In order to secure the fitting range adequately, we searched for HPDMs whose mass is from 50 to 120 keV/c^2 every 2.5 keV/c^2 steps. We use the sum of the BG model function and the signal model function (gaussian) as a model function, and fit it to the observed energy spectrum.

$$f(x) = a_0 + \exp(a_1 x + a_2) + \frac{a_3}{\sqrt{2\pi}a_5}\exp(-\frac{(x-a_4)^2}{2a_5^2}) + \frac{c}{\sqrt{2\pi}\sigma}\exp(-\frac{(x-\mu)^2}{2\sigma^2}), \quad (10.2)$$

where, a_0, a_1, a_2, a_3, a_4, and a_5 are free parameters. The mean value μ and the energy resolution σ are fixed parameters for each HPDM mass and derived from the signal MC tuned by calibration sources. The signal MCs are generated in the active volume of the XMASS detector spatially uniformly with respect to each HPDM mass. The normalized energy spectra of the signal MCs with each mass are shown in Fig. 10.16. A mean value μ and a resolution σ for each signal spectrum is derived by a gaussian fitting for the signal spectrum. The validity of the mean value and the resolution can be checked by the comparison between ^{57}Co (^{241}Am) calibration data and its MC. Figure 10.17 and Fig. 10.18 show the energy spectrum of ^{57}Co and ^{241}Am calibration data and their MCs, respectively. The discrepancy of the mean value and the energy resolution between the data and the MC is considered as a systematic error. The details are discussed in the next section.

We performed a peak finding by evaluating the chi square obtained by a fitting of the model function represented by Eqs. 10.2 to the observed energy spectrum, while increasing the signal intensity c iteratively. The value c is an expected number of HPDM events detected in the 327.8 kg fiducial volume during the 252.9 days live-time after applying the signal efficiency. This value can be calculated by Eqs. 5.7 as,

$$c \approx \frac{4 \times 10^{23}}{131.29}\kappa^2(\frac{keV}{m_V})(\frac{\sigma_{photo}}{barn}) \times 327.8 \times 252.9 \times \eta_{eff}. \quad (10.3)$$

Where, σ_{photo} is a cross section of photoelectric absorption obtained by Fig. 6.9. η_{eff} is a signal efficiency tabulated in Tab. 10.1. We search for significant signals or derive upper limits at 90% C.L. The fitting results at the best fit are shown in Fig. 10.19, 10.20, 10.21, 10.22, 10.23, 10.24, 10.25, and 10.26. The χ^2 shifts depending on κ for each HPDM mass are shown in Fig. 10.27, 10.28, 10.29, and 10.30. In order to take an uncertainty of the best fit parameters of the BG model function into accout, we took 7 as the degree of freedom and adopted $\Delta\chi^2$ =12.02 as an upper limit at 90% C.L.

We adopted "exponential + constant (+ gaussian)" represented by Eqs. 10.2 as a BG model function in this thesis. The critical value of the chi square distribution for the best fit with mass of 67.5 keV/c^2 is 13.6% (χ^2 = 161.7, ndf= 143), and have a sufficient validity. For confirmation, we checked fitting validities based on the other BG model function: "polynomial" and "fractional" function.

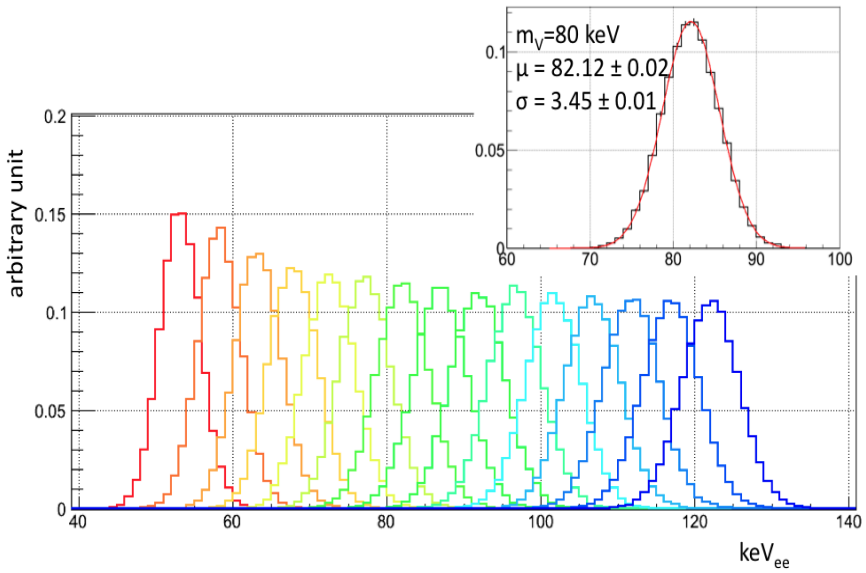

Figure 10.16: signal MC simulation (50,55,60,65,70,75,80,85,90,95,100,105,110,115, and 120 keV/c^2). Signal MC of 80 keV/c^2 and gaussian fitting (right upper).

$$f_{pol}(x) = a_0 + a_1 x + a_2 x^2 + a_3 x^3 + \frac{a_4}{\sqrt{2\pi} a_6} \exp(-\frac{(x-a_5)^2}{2a_6^2}) + \frac{c}{\sqrt{2\pi}\sigma} \exp(-\frac{(x-\mu)^2}{2\sigma^2}), \tag{10.4}$$

$$f_{frac}(x) = a_0 + \frac{a_1}{x+a_2} + \frac{a_3}{\sqrt{2\pi} a_5} \exp(-\frac{(x-a_4)^2}{2a_5^2}) + \frac{c}{\sqrt{2\pi}\sigma} \exp(-\frac{(x-\mu)^2}{2\sigma^2}), \tag{10.5}$$

a_0, a_1, a_2, a_3, a_4, a_5 and a_6 are free parameters. The fitting results at the best fit with mass of 67.5 keV/c^2 are shown in Fig. 10.31 (blue). The fitting by Eqs. 10.2 is also shown in the figure (red). For the comparison of the goodness of the fitting between the different BG modelings, we show the reduced chi square value at the best fit in Fig. 10.32. Since we can see that the fitting by Eqs. 10.2 is always better compared to the other function modeling, we adopted it as the BG model function in this thesis.

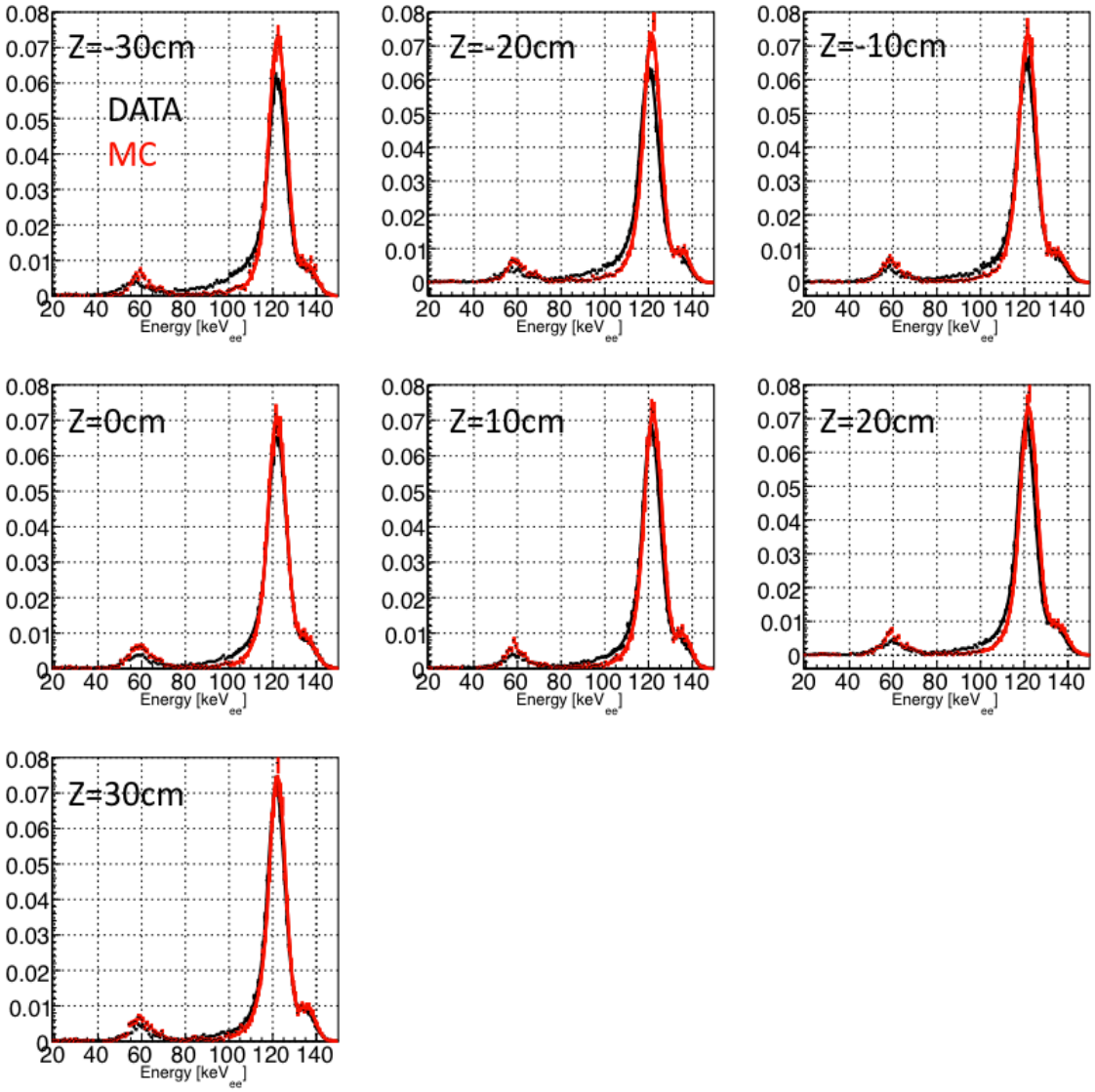

Figure 10.17: Position dependence of ^{57}Co 122 keV peak and their fitting by crystal ball function

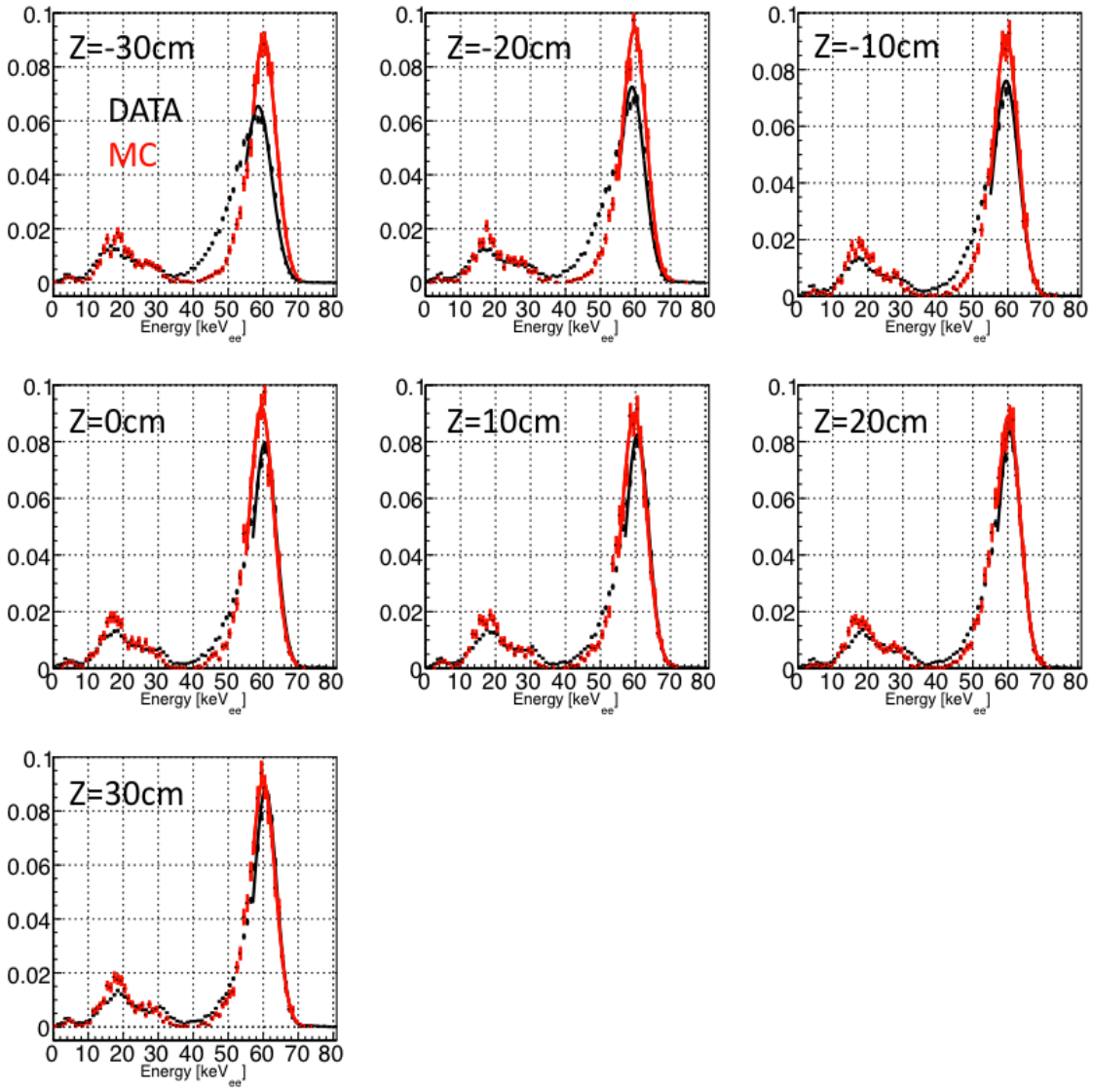

Figure 10.18: Position dependence of ^{241}Am 59.5 keV peak and their fitting by crystal ball function

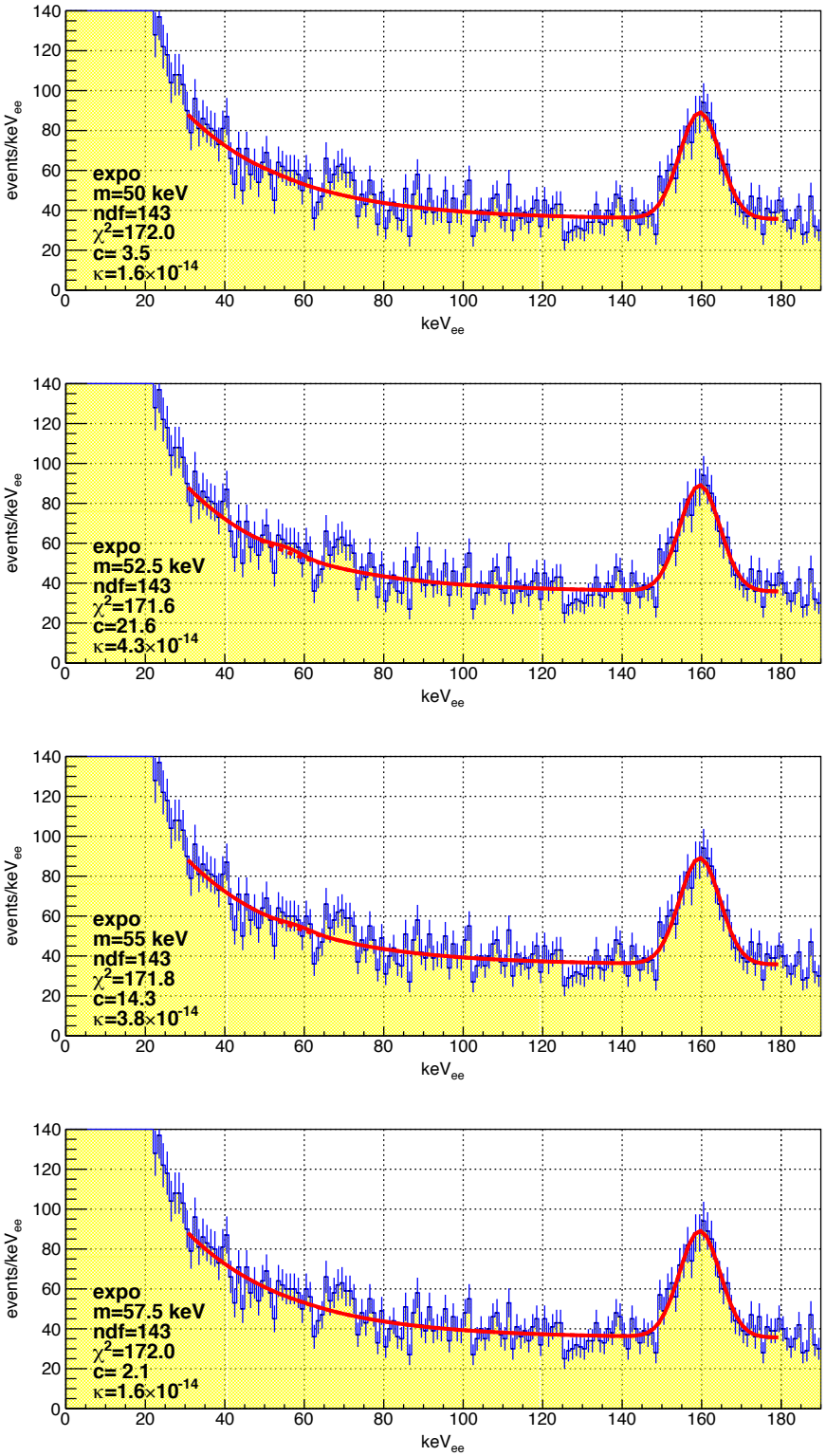

Figure 10.19: Fitting results for HPDM signals of m_V=50 - 57.5 keV/c^2 at the best fit. Only statistical errors are taken into account.

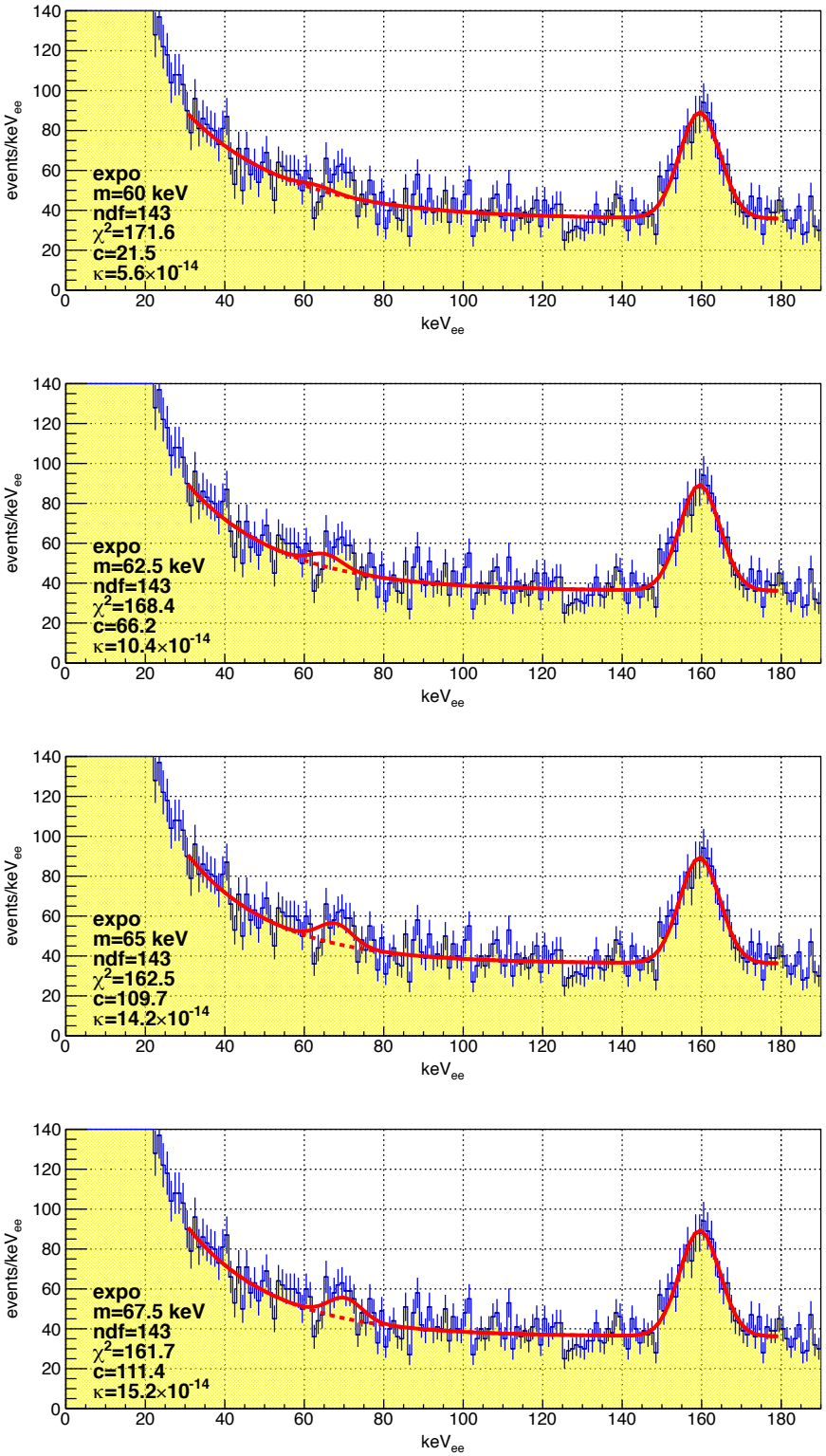

Figure 10.20: Fitting results for HPDM signals of m_V=60 - 67.5 keV/c^2 at the best fit. Only statistical errors are taken into account.

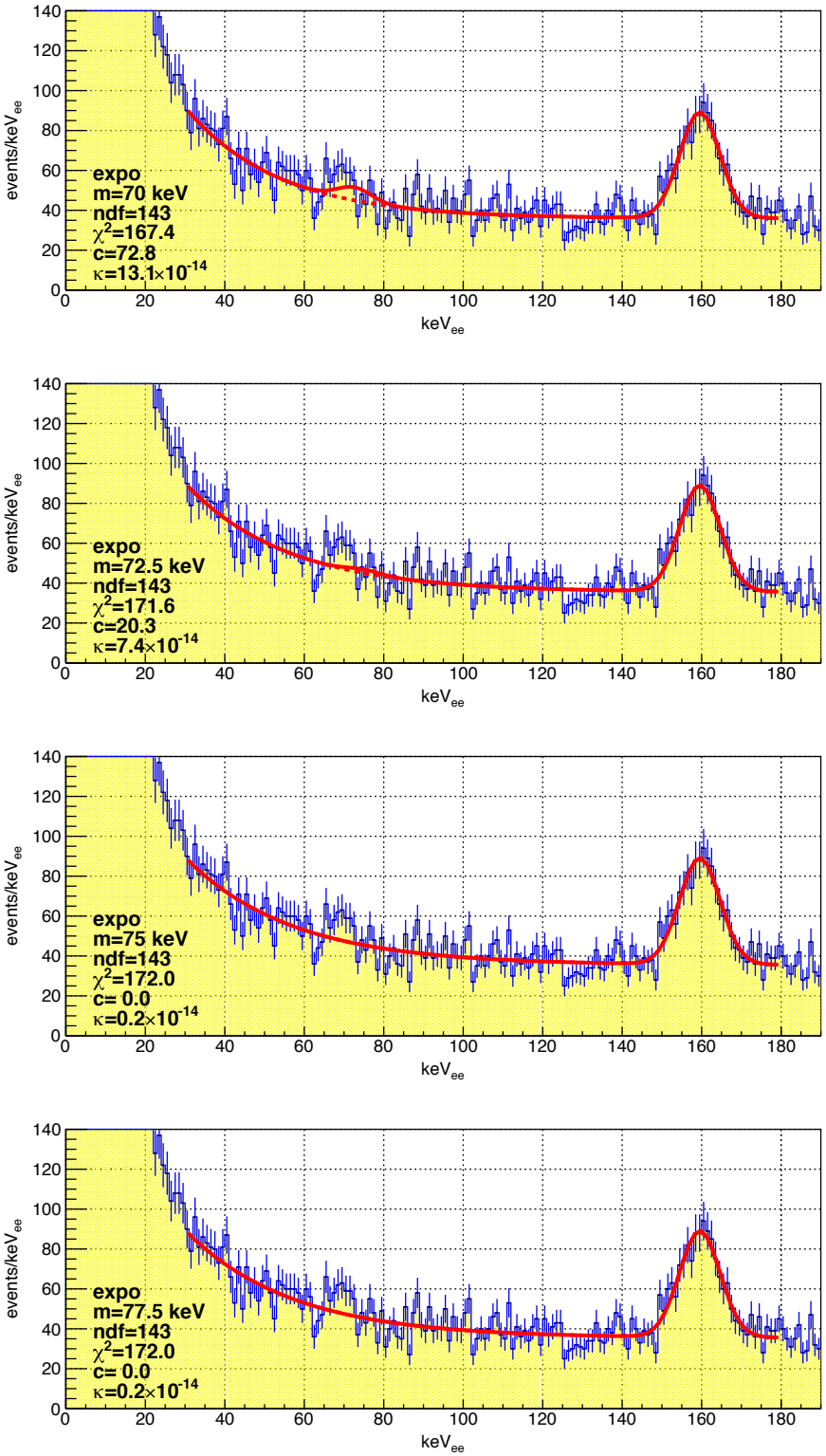

Figure 10.21: Fitting results for HPDM signals of m_V=70 - 77.5 keV/c^2 at the best fit. Only statistical errors are taken into account.

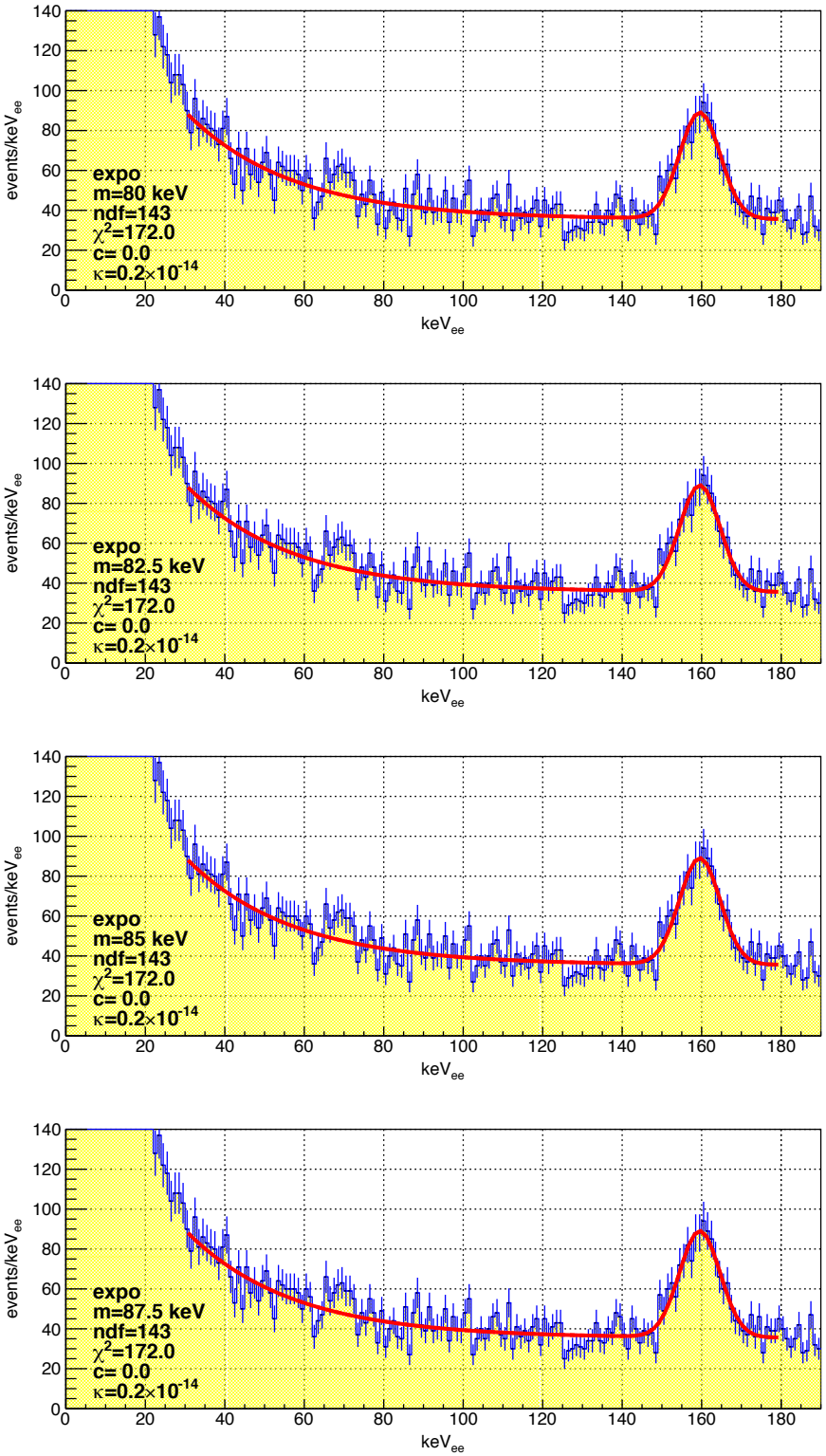

Figure 10.22: Fitting results for HPDM signals of m_V=80 - 87.5 keV/c^2 at the best fit. Only statistical errors are taken into account.

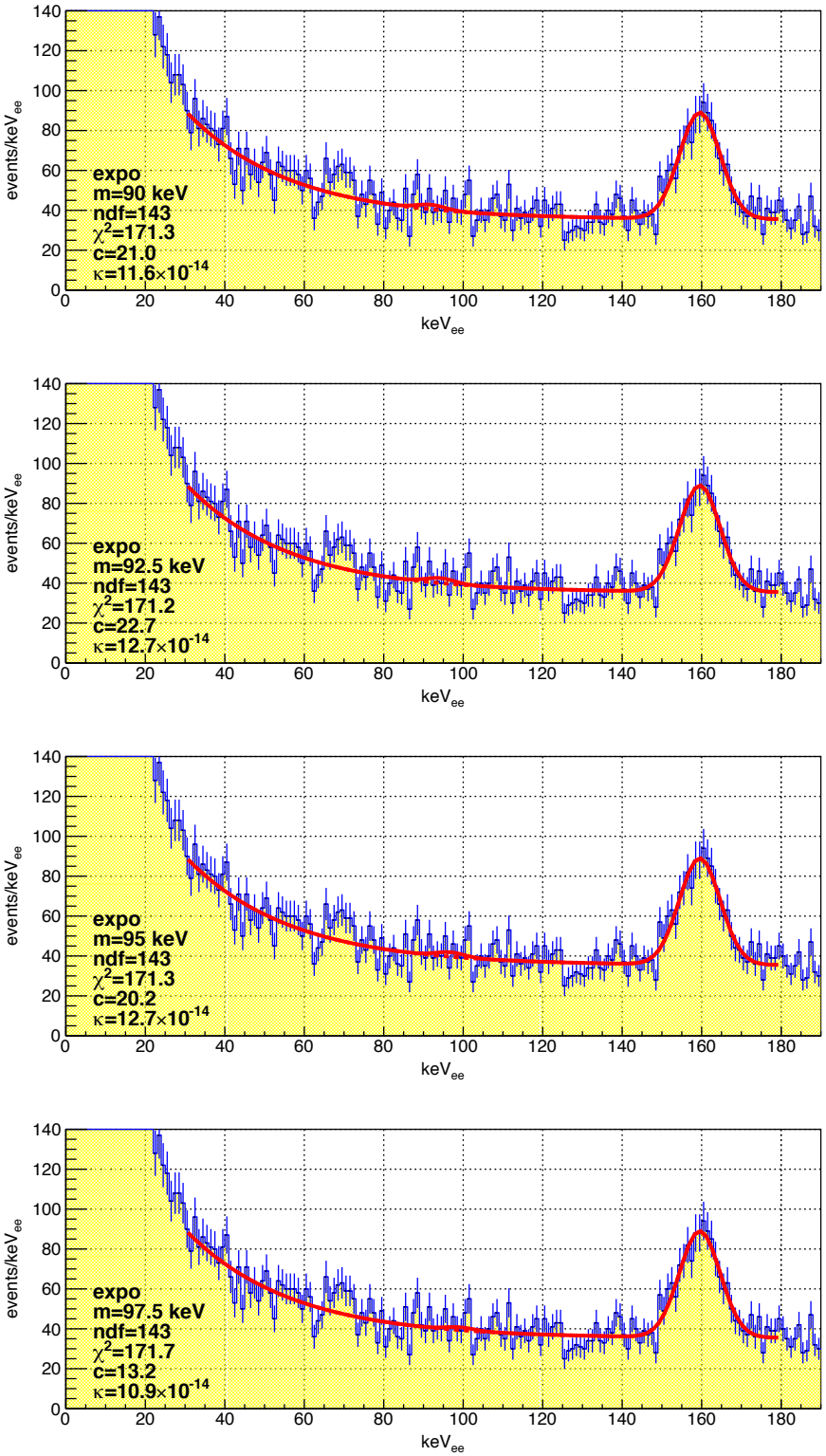

Figure 10.23: Fitting results for HPDM signals of m_V=90 - 97.5 keV/c^2 at the best fit. Only statistical errors are taken into account.

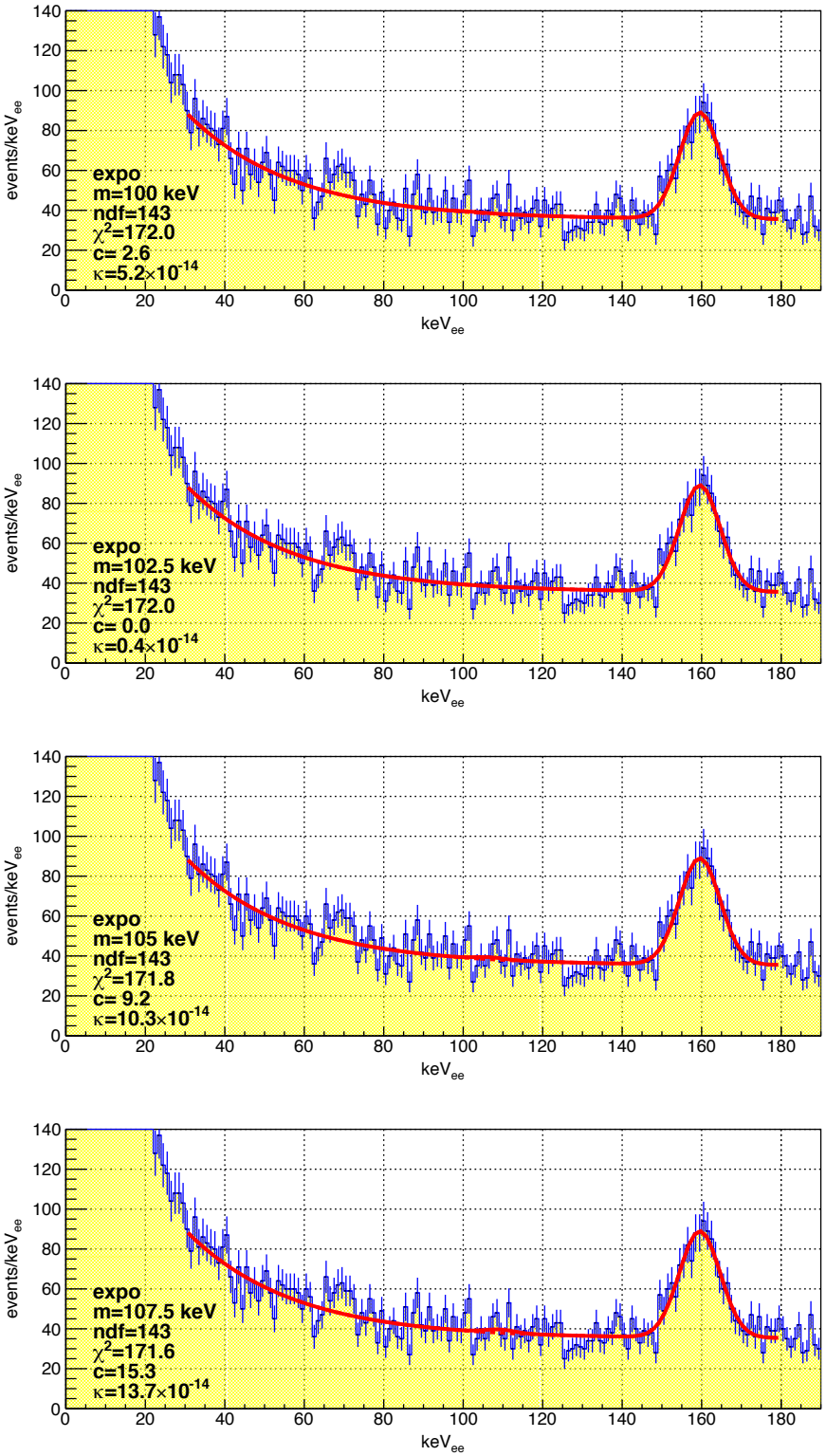

Figure 10.24: Fitting results for HPDM signals of m_V=100 - 107.5 keV/c^2 at the best fit. Only statistical errors are taken into account.

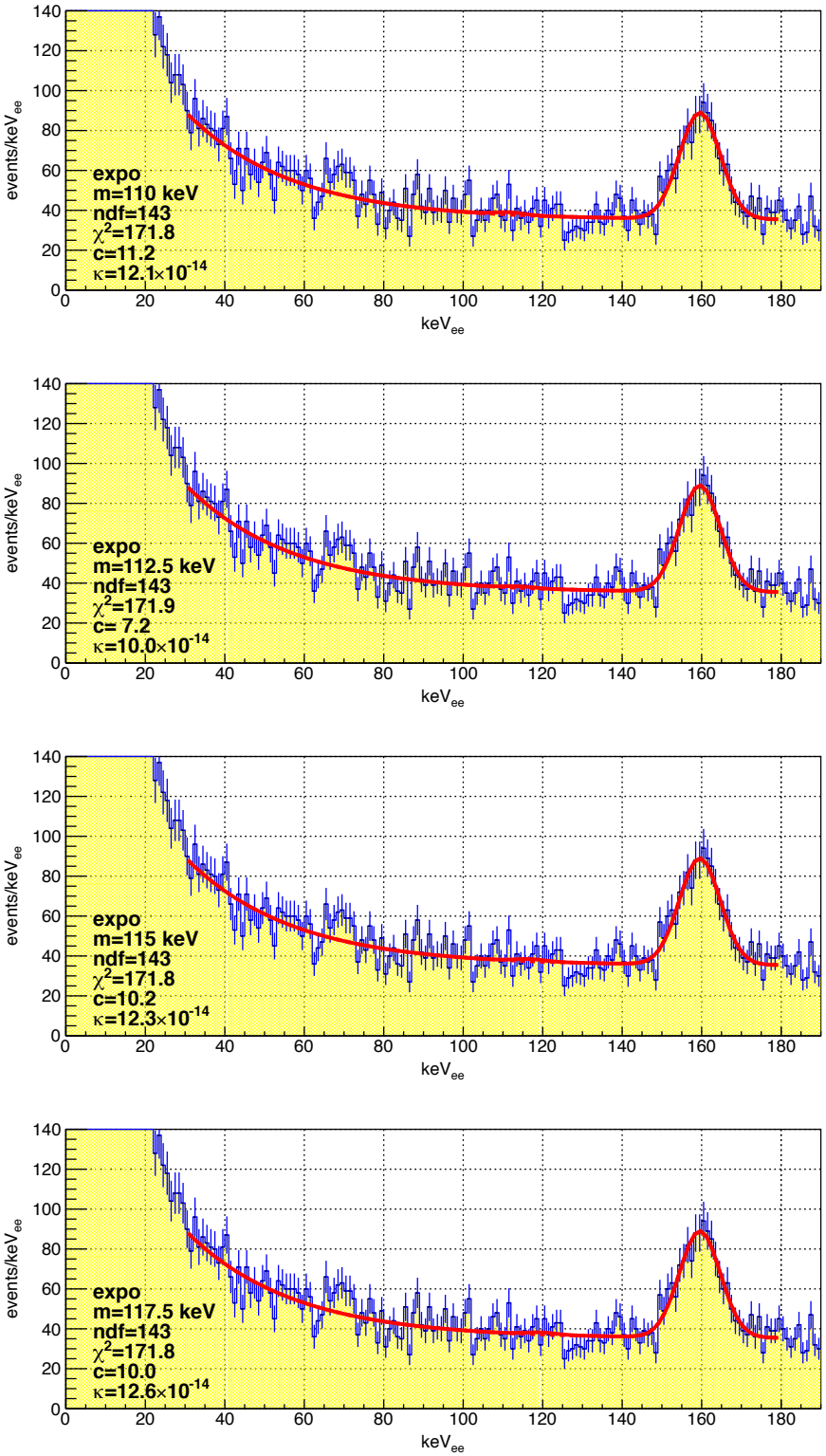

Figure 10.25: Fitting results for HPDM signals of m_V=110 - 117.5 keV/c^2 at the best fit. Only statistical errors are taken into account.

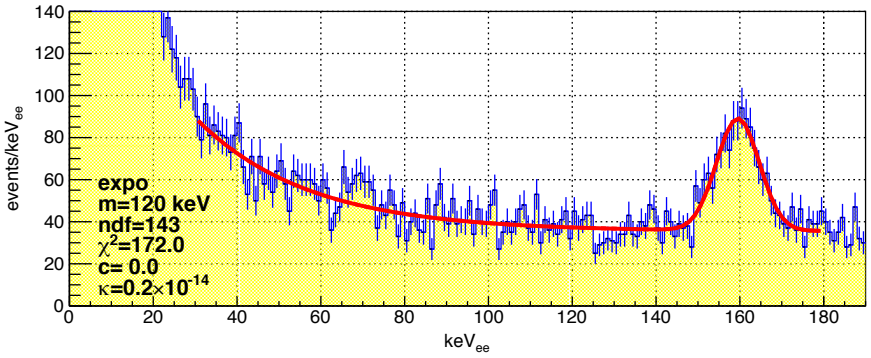

Figure 10.26: Fitting results for HPDM signals of m_V=120 keV/c^2 at the best fit. Only statistical errors are taken into account.

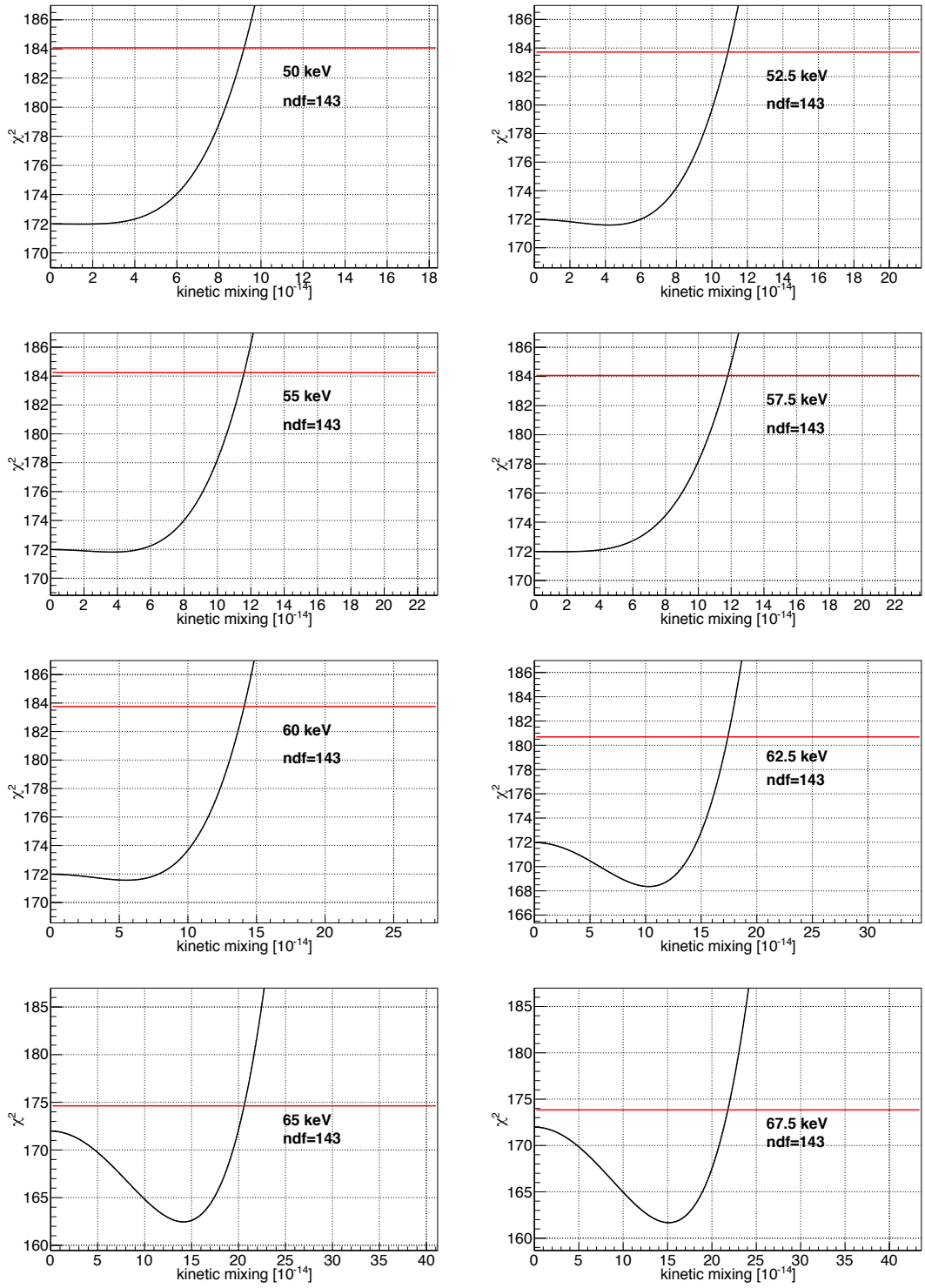

Figure 10.27: The x-axis represents the kinetic mixing parameter, while the y-axis represents the χ^2 for the fitting with HPDM mass of 50 - 67.5 keV/c^2. The red horizontal lines represent a 90% C.L. from the best fit ($\Delta\chi^2$=12.02). Only statistical errors are taken into account (case (1) in Tab. 10.5).

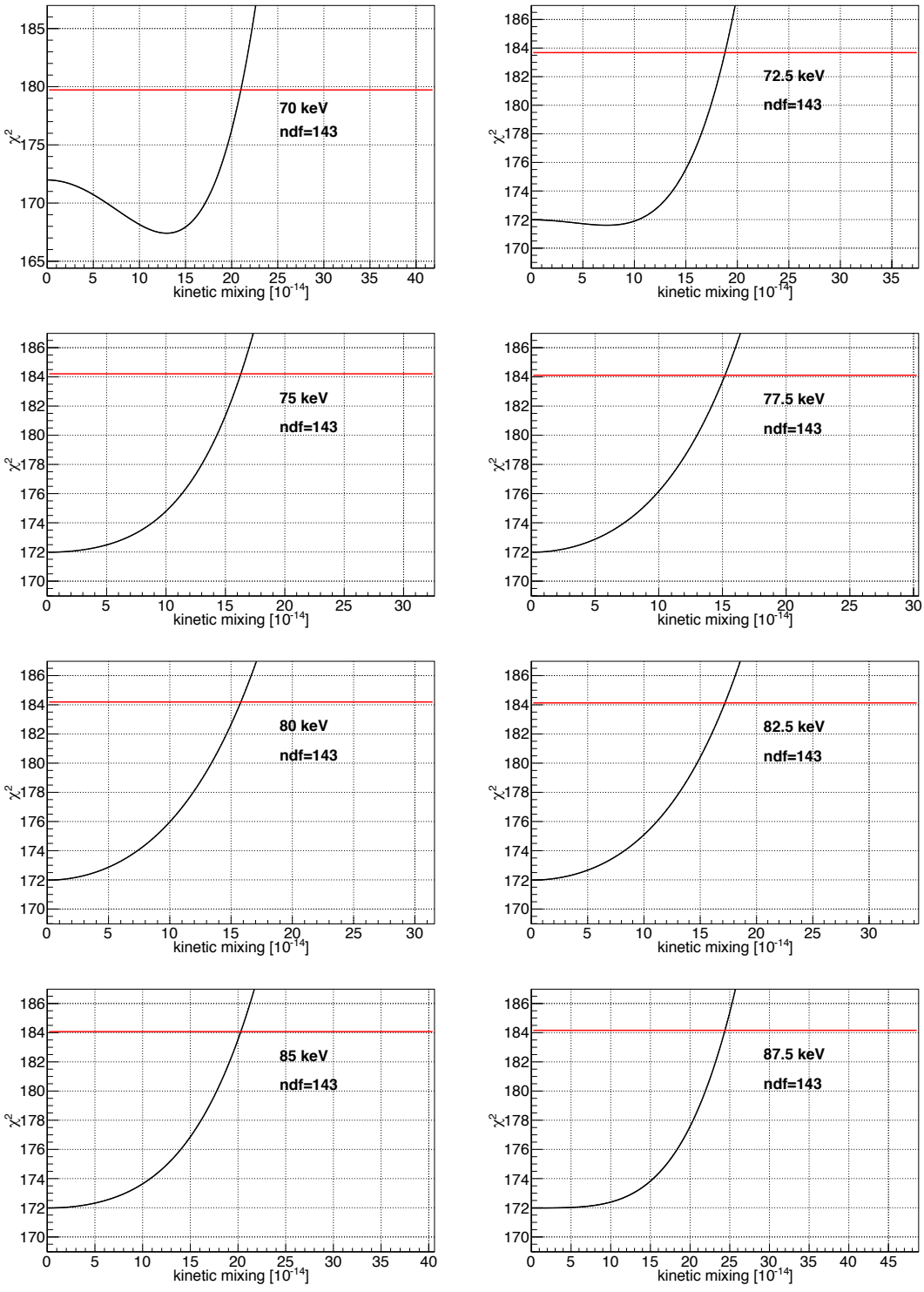

Figure 10.28: The x-axis represents the kinetic mixing parameter, while the y-axis represents the χ^2 for the fitting with HPDM mass of 70 - 87.5 keV/c^2. The red horizontal lines represent a 90% C.L. from the best fit ($\Delta\chi^2$=12.02). Only statistical errors are taken into account (case (1) in Tab. 10.5).

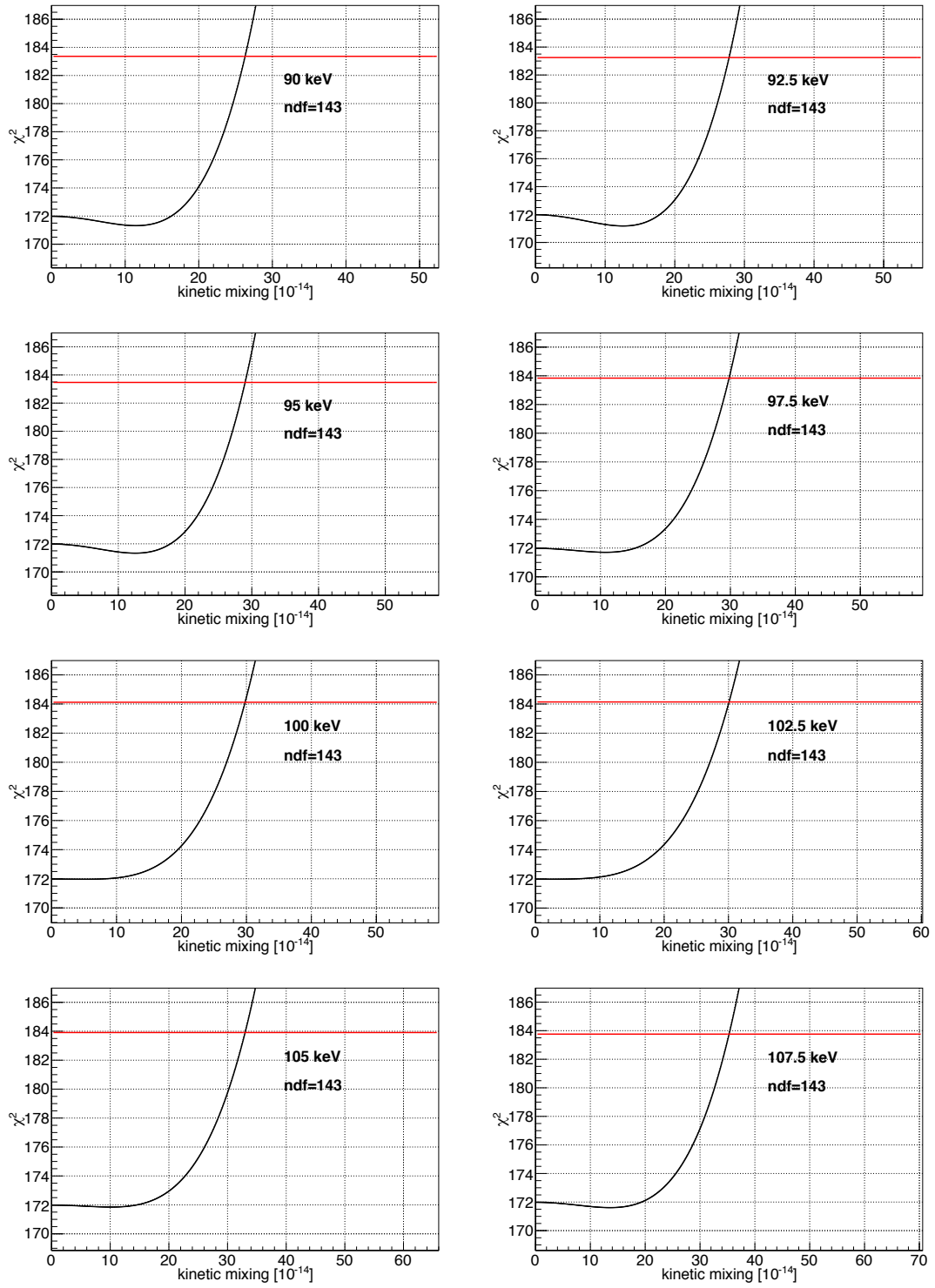

Figure 10.29: The x-axis represents the kinetic mixing parameter, while the y-axis represents the χ^2 for the fitting with HPDM mass of 90 - 107.5 keV/c^2. The red horizontal lines represent a 90% C.L. from the best fit ($\Delta\chi^2$=12.02). Only statistical errors are taken into account (case (1) in Tab. 10.5).

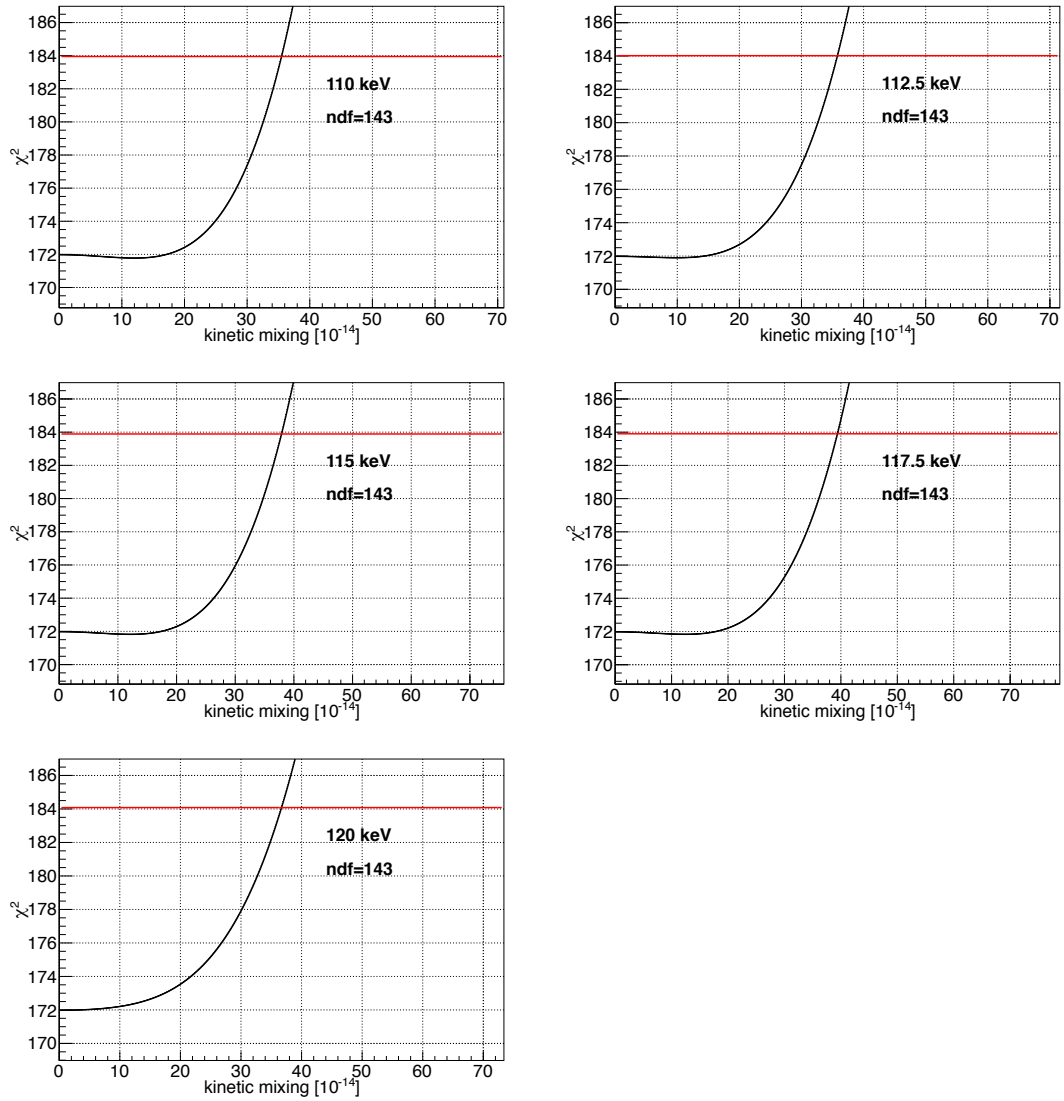

Figure 10.30: The x-axis represents the kinetic mixing parameter, while the y-axis represents the χ^2 for the fitting with HPDM mass of 110 - 120 keV/c^2. The red horizontal lines represent a 90% C.L. from the best fit ($\Delta\chi^2$=12.02). Only statistical errors are taken into account (case (1) in Tab. 10.5).

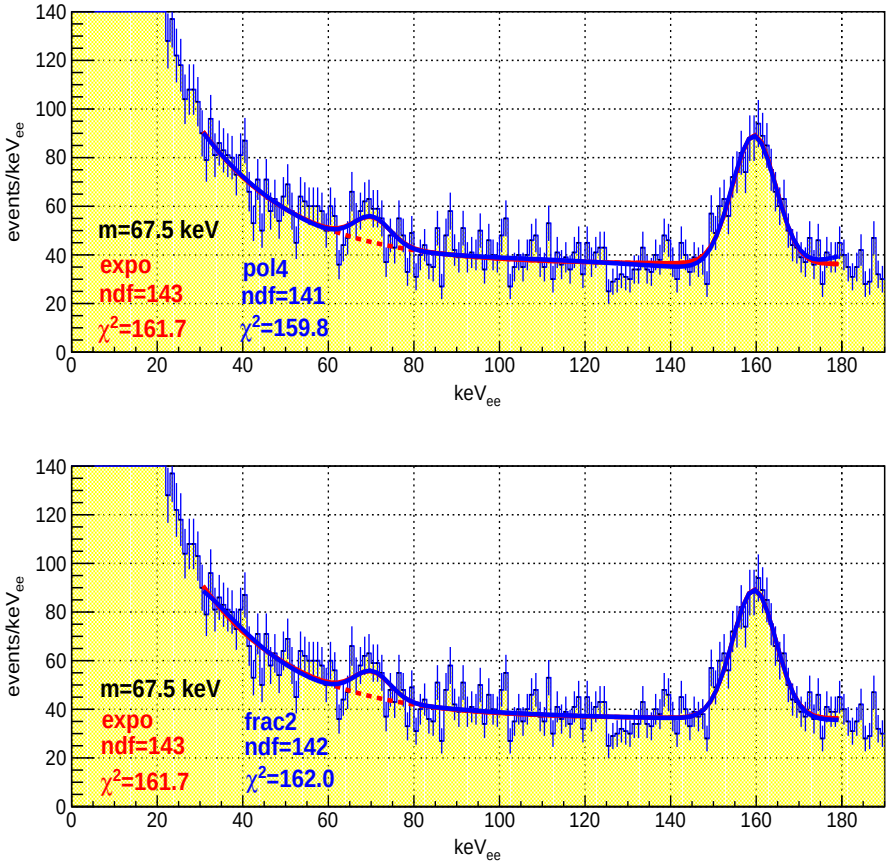

Figure 10.31: The upper figure shows an overlaid 4th-degree function (Eqs. 10.4) on a exponential function (Eqs. 10.2) at the best fit. The lower figure shows an overlaid 2nd-degree fractional function (Eqs. 10.5) on a exponential function (Eqs. 10.2) at the best fit. The mass of the signal is 67.5 keV/c^2.

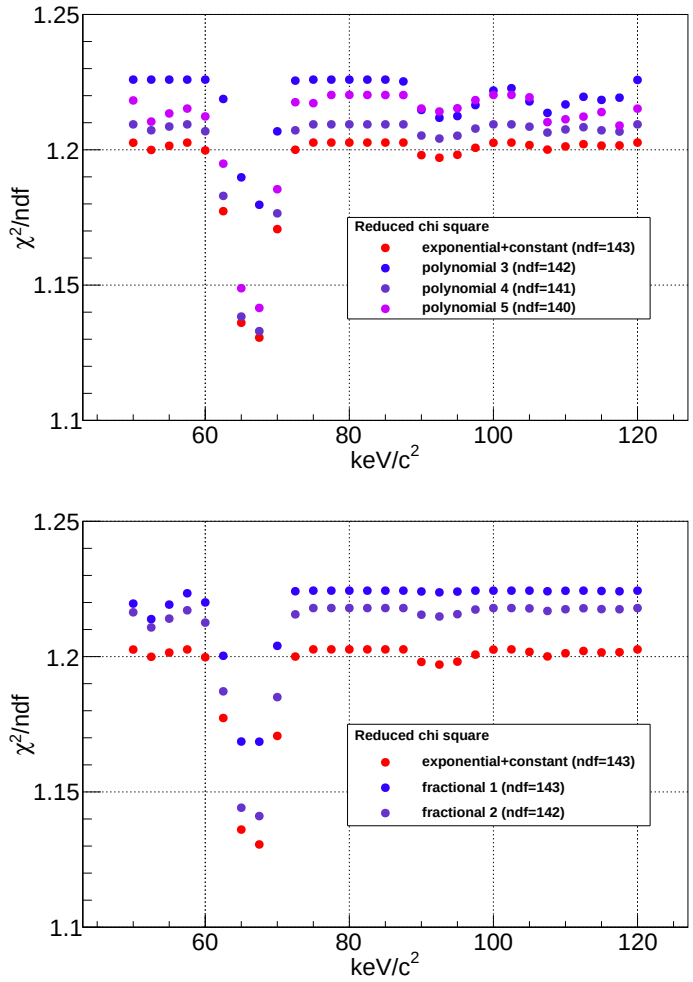

Figure 10.32: The reduced chi square at the best fit fot each signal mass. (upper) Red : eponential + constant, Blue : 3rd-order polynomial, purple : 4th-order polynomial, Pink : 5th-order polynomial. (lower) Red : exponential + constant, Blue : 1st-order fractional, Purple : 2nd-order fractional.

10.6 Systematic error evaluation

A systematic uncertainty on a kinetic mixing parameter was estimated using our calibration data at various positions within the fiducial volume and those taken in a several different time periods. The calibration MCs at corresponding positions were also used to compare with the data. From the comparisons of these distributions, we evaluated systematic differences in the energy scale, the radius reconstructed position, and the energy resolution. The systematic uncertainties of mass from 50 to 85 keV/c^2 were evaluated by using ^{241}Am, and those of mass from 90 to 120 keV/c^2 were evaluated by using ^{57}Co calibration source, respectively.

10.6.1 Energy scale

Absorption length change

As described in the previous section, the variation of the energy scale due to the changes of the absorption length are scaled based on the mean value of the ^{57}Co calibration data at $Z = 0$ cm. However, there is no guarantee that the impact of the change of the absorption length at a site distant from the detector center behave in the same manner with the center.

In order to know which radial position should be monitored, the radius cubed distribution of event rate was checked again. The mean value of the radial position weighted by the number of events resulted in $R =\sim 24$ cm for $R = 30$ cm fiducial volume. In this experiments we took ^{57}Co calibration data also at each 10 cm step every week in the data taking period. We check the behavior of the change of the 122 keV energy peak of $Z = -20$ cm and $Z = -30$ cm calibration data, instead of monitoring the behavior of $R = 24$ cm calibration data. We derive the mean of the reconstructed energy by fitting a crystal ball function (Eqs. 10.1) to the ^{57}Co calibration data. $Z = +20$ cm and $Z = +30$ cm calibration data are not used here because we know that shadow effects caused by the calibration rod inserted through the top of the detector are more relevant to the number of detected photons of the upper side than the lower side of the detector. In order to avoid the shadow effects, we used the $Z = -20$ cm and $Z = -30$ cm calibration data as representatives for $R = 20$ cm and $R = 30$ cm calibration sources to estimate systematic errors. Figure 10.33 shows the behavior of the relative peak position of $Z = 0$ cm (black circle), $Z = -20$ cm (blue triangle), and $Z = -30$ cm (red inverted triangle) after the time variation correction based on $Z = 0$ cm calibration data. From this figure, we found that $+/-0.9\%$ deviation of energy scale change is remaining even after the time variation correction. We take this $+/-0.9\%$ deviation into account as a systematic error conservatively.

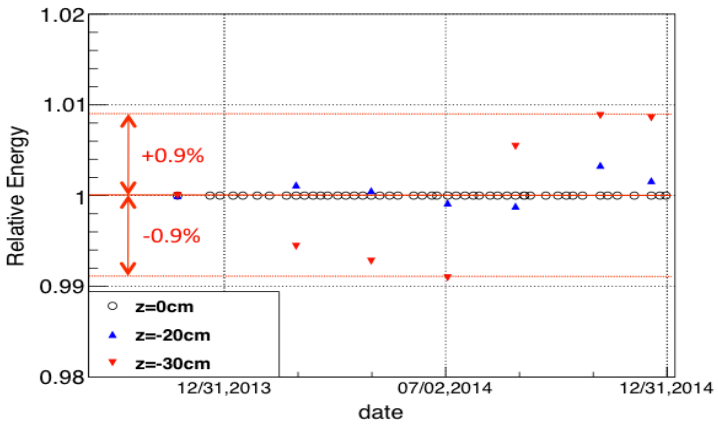

Figure 10.33: The variation of relative reconstructed energy of ^{57}Co energy peak at $Z = 0$ cm, -20 cm, and -30 cm after the time variation correction. The remained difference of the change (± 0.9 %) is considered as a systematic error conservatively. The intrinsic position dependences of reconstructed energies are discussed as another item in the next section.

Uncertainties of position dependence of energy

If an estimation of a position dependence of a reconstructed energy have some inaccuracy, it will cause an error on the energy scale. Figure 10.17 and 10.18 show the energy spectrum of each source position and their fitting results. Figure 10.34 shows position dependences of reconstructed energy for ^{241}Am and ^{57}Co, respectively. Weighting the difference between the MC and data for each source position, the mean deviations of $^{+0.8}_{-1.8}$% for ^{241}Am and -0.7% for ^{57}Co were obtained, respectively.

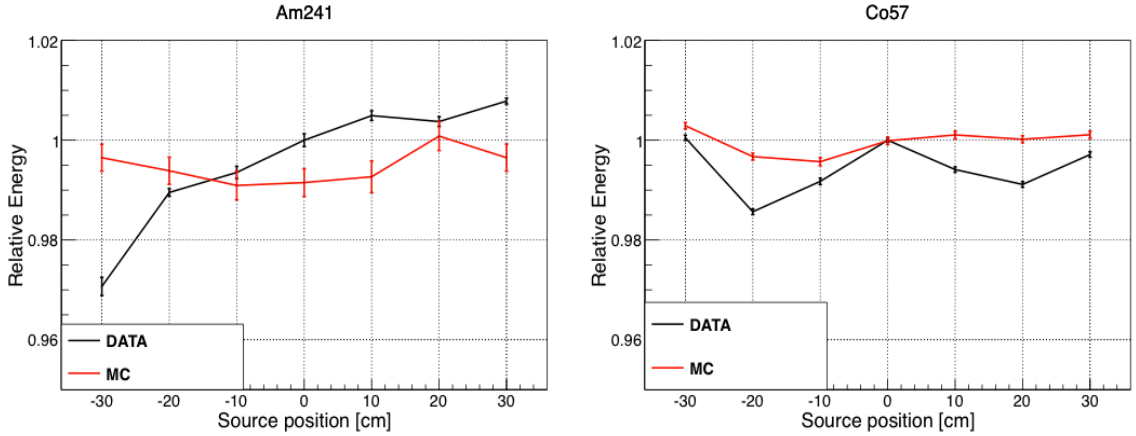

Figure 10.34: Position dependences of reconstructed energy of peak position of the sources

10.6.2 Fiducial volume cut

Absorption length change

The longer the absorption length of the liquid xenon become, the less the difference in the detected number of photons among the PMTs become, and the reconstructed position results in more inner position. Figure 10.35 (left) shows the time variation of the reconstructed radius of the ^{57}Co source ($Z = -30$ cm). The right figure shows the MC deduced absorption length dependence of reconstructed radius position of the source. The relative changes of reconstructed position is $+0.12$ cm and -0.18 cm with reference to the position of the first taken ^{57}Co calibration data (Nov. 22, 2013). This change is considered as a systematic error for the fiducial volume cut.

Uncertainties of reconstructed position

We also need to consider the difference of reconstructed position between data and MC. Figure 10.36 and Fig. 10.37 show the reconstructed radius distributions of each source position for ^{241}Am and ^{57}Co calibration sources, respectively. The left and right figures of Fig. 10.38 show a difference of a reconstructed radius between data and MC of each source position. We are interested especially in the accuracy of the reconstructed position around $R = 30$ cm because the fiducial volume cut was applied at $R = 30$ cm. These figures show the discrepancy around ± 30 cm is almost within a range of ± 0.30 cm error. We consider this ± 0.30 cm as a systematic error.

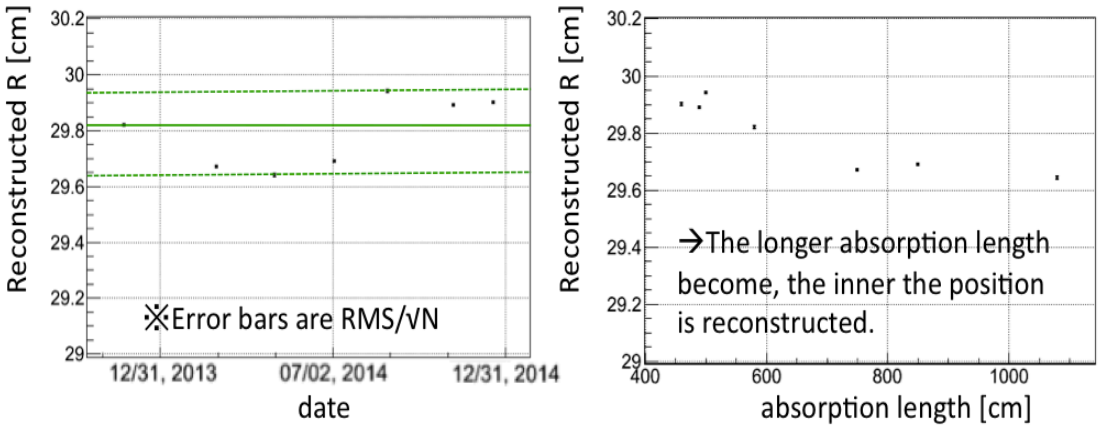

Figure 10.35: Time variation of reconstructed radius position of $Z = -30$ cm ^{57}Co source (left) and MC deduced absorption length dependence of reconstructed radius position of the source (right).

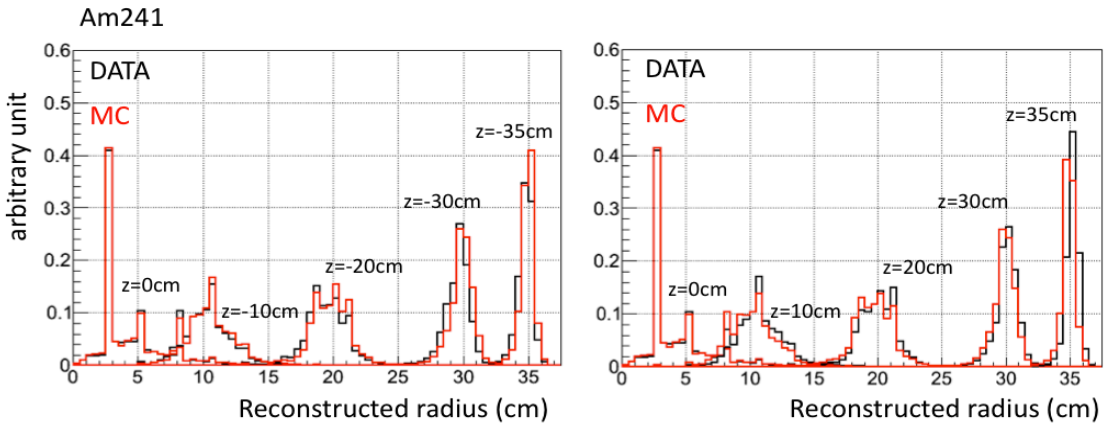

Figure 10.36: The comparison of reconstructed radius position distribution between the ^{241}Am data (black) and their MCs (red) at nine vertical positions in the detector; $Z = -35$ cm, -30 cm, -20 cm, -10 cm, 0 cm, $+10$ cm, $+20$ cm, $+30$ cm, $+35$ cm.

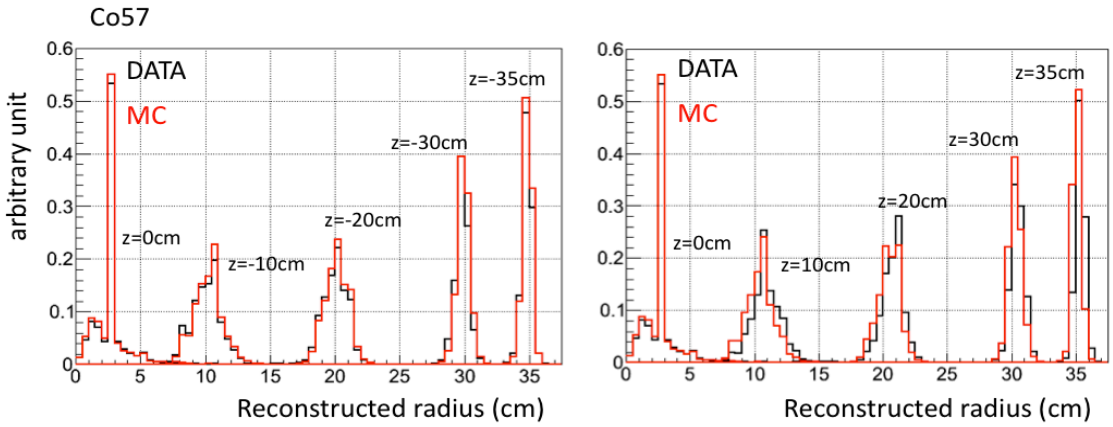

Figure 10.37: The comparison of reconstructed radius position distribution between the ^{57}Co data (black) and their MCs (red) at nine vertical positions in the detector; $Z = -35$ cm, -30 cm, -20 cm, -10 cm, 0 cm, $+10$ cm, $+20$ cm, $+30$ cm, $+35$ cm.

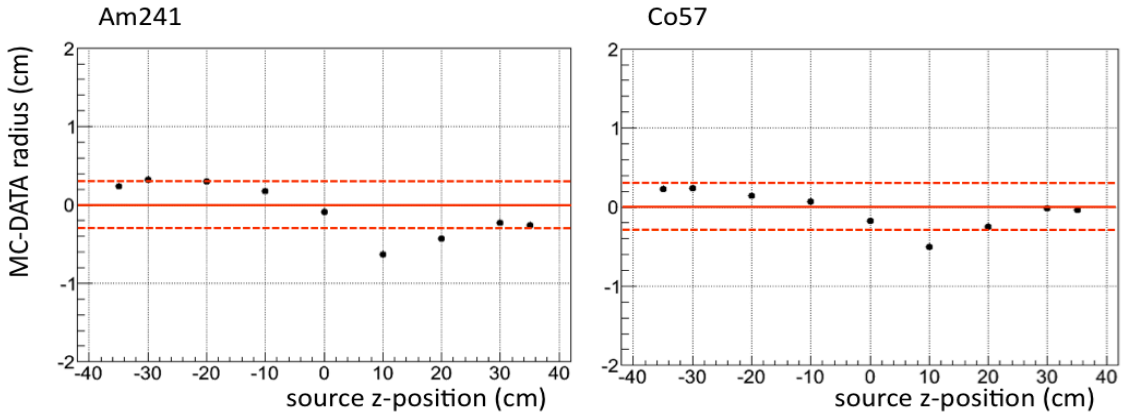

Figure 10.38: Difference of reconstructed radius position between data and MC for ^{241}Am (left) and ^{57}Co (right) .

10.6.3 Energy resolution

Absorption length change

The variation of the energy resolution of ^{57}Co peak is shown in Fig. 10.39. The maximum difference from the first taken calibration data ($+11\%, -14\%$) was considered as a systematic error conservatively.

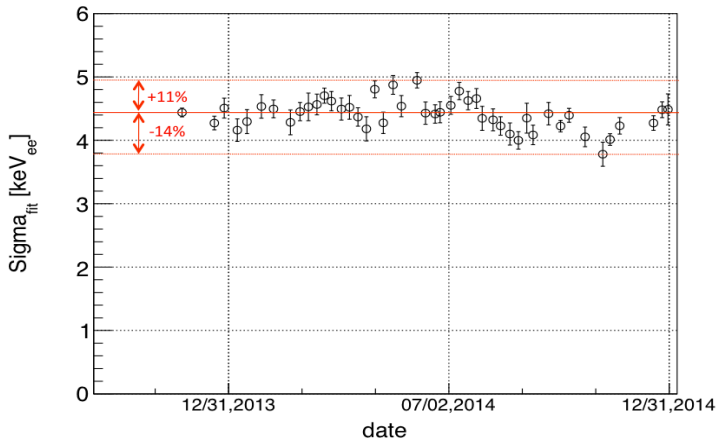

Figure 10.39: Time variation of the energy resolution of $z = 0$ cm ^{57}Co source.

Uncertainties of energy resolution

The uncertainties of the energy resolution are evaluated by comparing between the resolution of 59.5 keV peak in the ^{241}Am (122 keV peak in the ^{57}Co) calibration data and their MC as shown in Fig. 10.40. The peak of ^{241}Am have a tail at the side of lower energy as shown in Fig. 10.18. In order to take the tail into account, RMS of the distributions larger than 30 keV$_{ee}$ were used to define the resolution. On the other hand, the peak of ^{57}Co is almost symmetric but have other 136 keV$_{ee}$ peak on their right side as shown in Fig. 10.17. In order to avoid the effect of 136 keV$_{ee}$ peak, we fit a crystal ball function to the peak and derived a sigma as its energy resolution. The error is fitting error. In the case of ^{241}Am, the resolutions of the data are systematically worse than the MCs. We artificially smear the resolution of the MC (and also the signal model function) by +34% to fit with the real data at $z = 0$ cm. The remaining differences between the data and the MC weighted by the volume was considered as systematic errors (-4% for ^{241}Am and $+7\%$ for ^{57}Co).

The validity of the estimation of the energy resolution of the signal MC can be confirmed by using the peak of ^{131m}Xe in the real data. Figure 10.41 (right) shows the energy distribution of 163.9 keV/c^2 HPDM MC generated uniformly in the fiducial volume and fitting with gaussian function. The right figure shows the energy spectrum of the real data and fitting a sum of linear and gaussian function to the ^{131m}Xe peak. The derived resolution (sigma in gaussian fitting) is 5.0±0.4 and 4.8±0.0 for data and MC, respectively. This suggests that the MC is reproducing the energy resolution correctly and our estimation of the systematic error is sufficient.

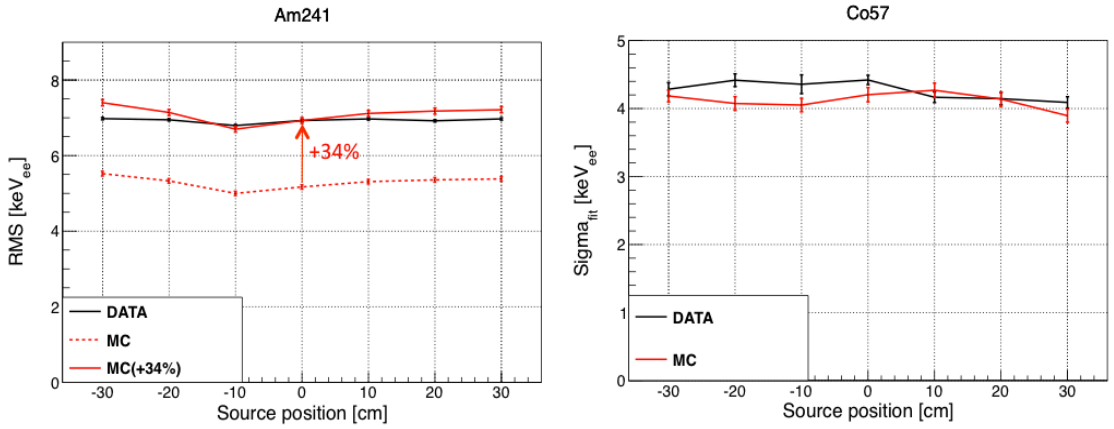

Figure 10.40: Position dependence of energy resolution of the data and the MC for ^{241}Am (left) and ^{57}Co (right), respectively.

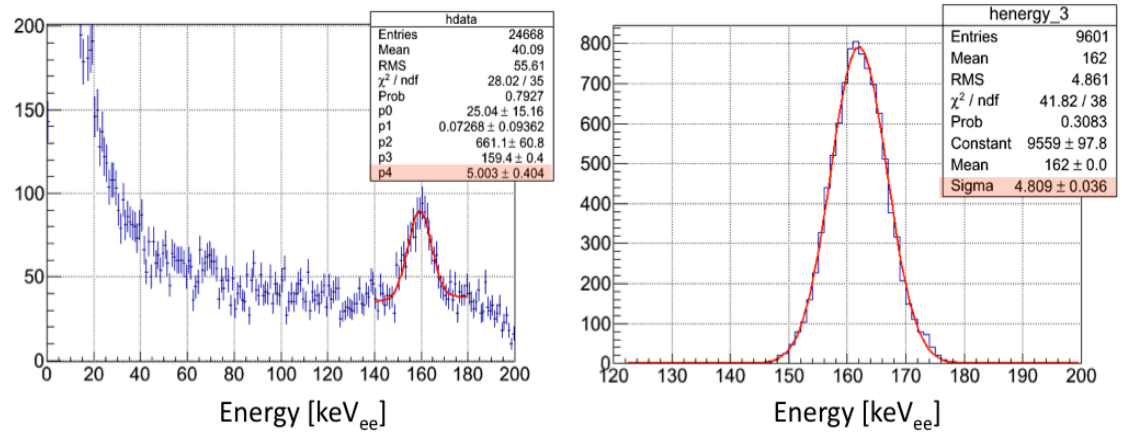

Figure 10.41: Energy resolution of m_V=163.9 keV/c^2 HPDM MC (left) and ^{131m}Xe peak (163.9 keV) in the real data (right).

10.6.4 BG modeling

We adopted Eqs. 10.2 as the BG model function. The critical value of the chi square distribution for the best fit with mass of 67.5 keV/c^2 is 13.6% and reasonably good. Besides, the fitting is better compared to the other elementary function: "polunomial" and "fractional" function. As mentioned earlier, We took 7 as the degree of freedom and drived upper limits in order to take an uncertainty of the best fit parameters of the BG model function into accout. We don't consider the additional systematic errors originated with the uncertainty of the BG modeling in this thesis.

10.6.5 Total systematic error

The systematic errors discussed in this section are summarized in Tab. 10.4. For ease of comprehension, the impacts of the systematic errors on a kinetic mixing parameter at 90% C.L. are summarized separately in Tab. 10.5. The total systematic error of energy scale was derived by the quadrature of each systematic errors and resulted in $^{+1.1}_{-2.0}$% for ^{241}Am and $^{+0.8}_{-1.1}$% for ^{57}Co. This error was taken into account as the uncertainty of the mass of the searched HPDM. We did not include these uncertainties for the final result because the uncertainties are relatively small compared to the step size of the mass of the searched HPDM (2.5 keV/c^2). The systematic uncertainties of the reconstructed position are added in quadrature and result in $^{+0.32}_{-0.35}$ cm. The errors result in changes of the signal efficiency η_{eff}. We defined the signal efficiency using the signal MC as the number of events remaining after the fiducial volume cut (R_{rec} <30 cm) divided by the total events generated in the fiducial volume (R_{gen} <30 cm). The signal efficiencies were re-calculated by estimating the number of events in the fiducial volume of $R_{rec} < 29.68$ cm. The systematic uncertainties of the energy resolution are added in quadrature and result in $^{+11}_{-15}$% for ^{241}Am and $^{+13}_{-14}$% for ^{57}Co. The effect of the systematic error of the energy resolution is taken into account by smearing the energy resolution of the signal part of the model function by +11% and +13% for the mass of 50 - 87.5 keV/c^2 and 90 - 120 keV/c^2, respectively at the time of peak finding.

We derived an upper limit on κ at 90% C.L. both for without systematic errors and with systematic errors in Tab. 10.5. The second column shows the upper limit with only statistic errors. The third column is including the systematic errors of the reconstructed position and the fourth column is including the systematic errors of the energy resolution.

Item	Error source	^{241}Am	^{57}Co
HPDM mass (keV/c^2)		50 - 87.5	90 - 120
Energy	Absorption length	+/−0.9%	
	Uncertainty of position dependence	$^{+0.8}/_{-1.8}$%	−0.7%
Position	Absorption length	$^{+0.12}/_{-0.18}$ cm	
	Uncertainty of radius cut position	+/−0.30 cm	
Energy resolution	Absorption length	$^{+11}/_{-14}$%	
	Uncertainty of position dependence	−4%	+7%

Table 10.4: Summary of the systematic errors. The systematic error of energy resolution for ^{241}Am is a value after +34% smearing of the MC. The impacts on the kinetic mixing parameter are summarized in Tab. 10.5.

mass(keV/c^2)	κ ($\times 10^{-14}$)		
	(1)	(2)	(3)
50	9.2	9.4	9.7
55	11.6	11.8	12.2
60	14.1	14.3	15.5
65	20.6	21.0	21.5
70	21.0	21.4	21.9
75	16.3	16.6	17.4
80	15.8	16.0	16.9
85	20.3	20.7	21.3
90	26.3	26.8	27.5
95	29.0	29.5	30.6
100	29.8	30.3	31.8
105	33.0	33.6	34.8
110	35.5	36.1	37.6
115	37.9	38.6	40.0
120	36.7	37.4	37.4

Table 10.5: The upper limits on kinetic mixing parameter.
(1)Statistical errors only.
(2)With the systematic errors of "Position".
(3)With the systematic errors of "Position" and "Energy resolution".

Chapter 11

Result and Discussion

11.1 New constraint on kinetic mixing parameter

In Chap. 10, we iteratively fitted a model function to the energy spectrum of the real data while changing the kinetic mixing parameter. As a result, no significant signal is observed and limits are set at 90% C.L. on the kinetic mixing parameter.

Although the significance is not large, a small bump structure around m_V=67.5 keV/c^2 was observed. Figure 10.27 also indicates the best fits have $\Delta\chi^2$ of 10.3 from a non-signal assumption ($\sim 1.36\sigma$). We explain an interpretation of the bump here. Our detector has gas xenon regions outside the active volume and which are partially exposed on the outside of the water shield. The volume is about 420 l. These regions can suffer from the activations by thermal neutron BG. Actually, ^{125}I which is daughter of ^{125}Xe activated by thermal neutron capture of ^{124}Xe (Natural abundance of 0.095%) deposits total energies of 67.3 keV$_{ee}$ by electron capture and the sequential γ-ray (or internal conversion). The decay scheme of ^{125}I is shown in Fig. 11.2. This energy deposit have possibility to generate a peak around 67.5 keV$_{ee}$. We briefly evaluate the expected number of events caused by the captures of thermal neutrons generated in the gas xenon phase. For the calculation, we applied four assumptions below.

- Thermal neutron flux outside the water shield [79] : 8.3e-6 [/sec/cm^2]
- Volume outside the water shield : 4.2e+5 [cm^3]
- Radiation equilibrium for ^{125}I ($T_{1/2}$=59.41 days) are satisfied.
- Majority of the RI generated in the gas phase are uniformly distributed in the liquid xenon region.

The expected number of events observed during 170.4 days data set is approximately 84 events. While, the observation value derived by the best fit by a signal MC of m_V=67.5 keV/c^2 is 83^{+80}_{-83} events (1σ error) as shown in Fig. 11.1. These values are of the same order of magnitude each other. The more detail studies are needed to conclude that the small peak around 67.5 keV$_{ee}$ is caused by these mechanism.

Finally, we obtained an upper limit on a kinetic mixing parameter at 90% C.L. The constraint curve on the kinetic mixing parameter is shown in Fig. 11.3. The red dotted (solid) line shows an upper limit including only statistical errors (all systematic errors discussed in context) assuming Eqs. 10.2 as the BG model function. This constraint

is about two times better than the previous result by the data taken by the XMASS commissioning phase and the most stringent in the direct detection experiments to date.

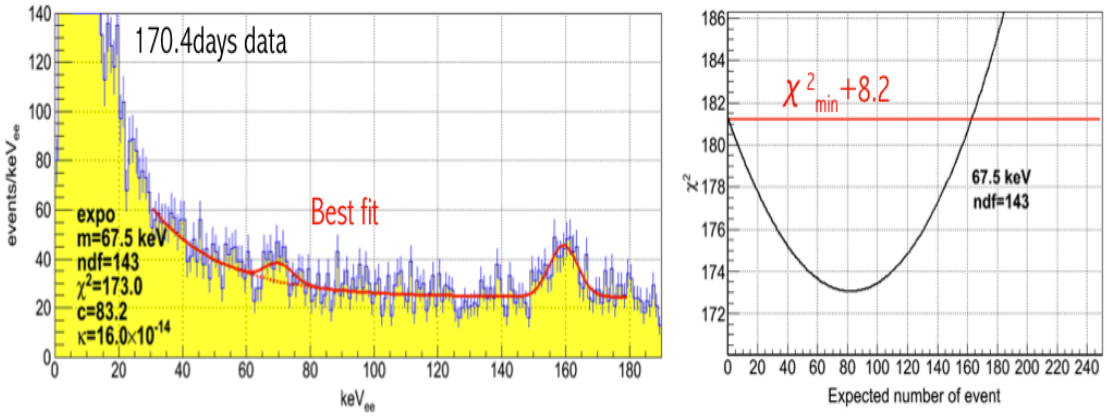

Figure 11.1: The best fit for the small peak around m_V=67.5 keV/c^2 (left), and the χ^2 shift depending on the number of event (right).

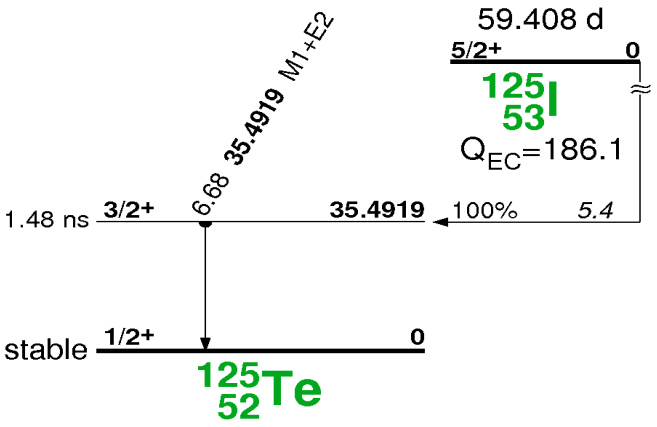

Figure 11.2: Decay scheme of ^{125}I.

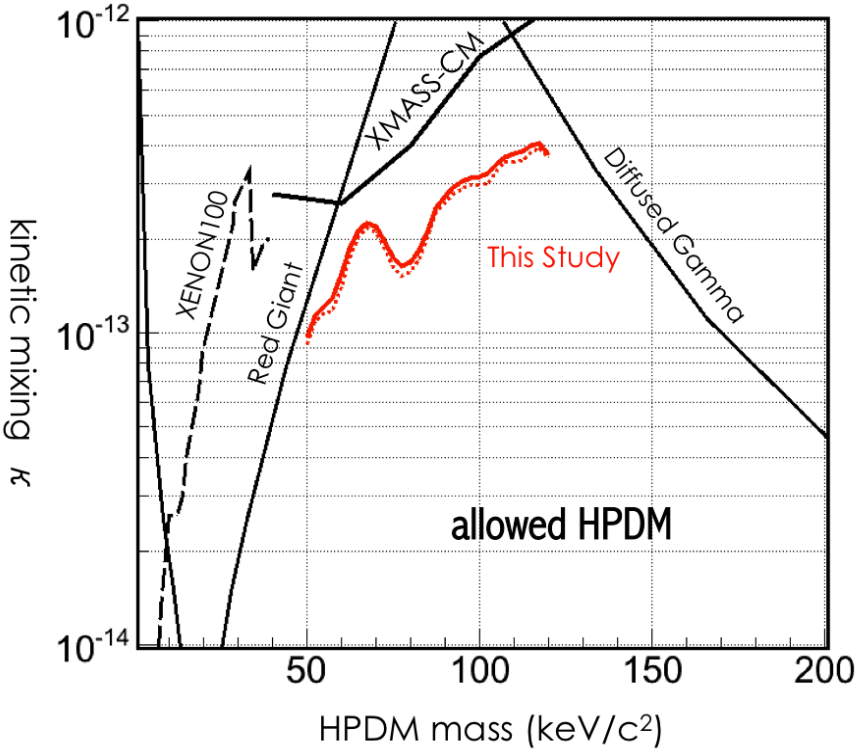

Figure 11.3: Upper limit on kinetic mixing parameter κ at 90% C.L. set by this study. The red dotted (solid) line shows an upper limit including only statistical errors (all systematic errors discussed in context) assuming Eqs. 10.2 as a BG model function. The bounds labelled "Red Giant", "XENON100", and "Diffused Gamma" are taken from Ref. [51]. "XMASS-CM" indicates the bound constrained from a search for the thermally produced HPDMs (i.e. superWIMPs) conducted during the XMASS commissioning run. The systematic errors of energy scale are relatively small and omitted in this figure.

11.2 Discussions

Figure 11.4 shows the energy spectra of the data (black) and that estimated by our BG MC (each color). The left figure shows stacked energy spectra and the right figure shows non-stacked energy spectra. The red line in the right figure indicates the sum of all the BG components.

Since the origin of generation of ^{131m}Xe is unknown, the amount of ^{131m}Xe was set in a way that is consistent with the size of the peak around 160 keV$_{ee}$. Actually, our known BG components can not completely explain the data spectrum. We have unknown BG components less than 100 keV$_{ee}$. We searched every possible RI candidates. From some hints for this component (a flat distribution in the R^3 distribution suggests an inner BG, the decay constant prefers β-ray events, the small time variation (<10%) indicates a long half-life (>10 years), and the expected spectrum shape is similar to the observed spectrum (The end point is 156 keV$_{ee}$)), we are suspecting ^{14}C as a candidate. Figure 11.5 shows the decay scheme and β-ray spectrum of ^{14}C. The amount of ^{14}C was set in a way that is consistent with the amount of the events between 40 keV$_{ee}$ and 100 keV$_{ee}$. The shape of the energy spectrum estimated by the MCs is similar to the data spectrum. However the model is not perfect. For instance, gaps are remaining larger than 100 keV$_{ee}$. We need to pursue studies for more understanding.

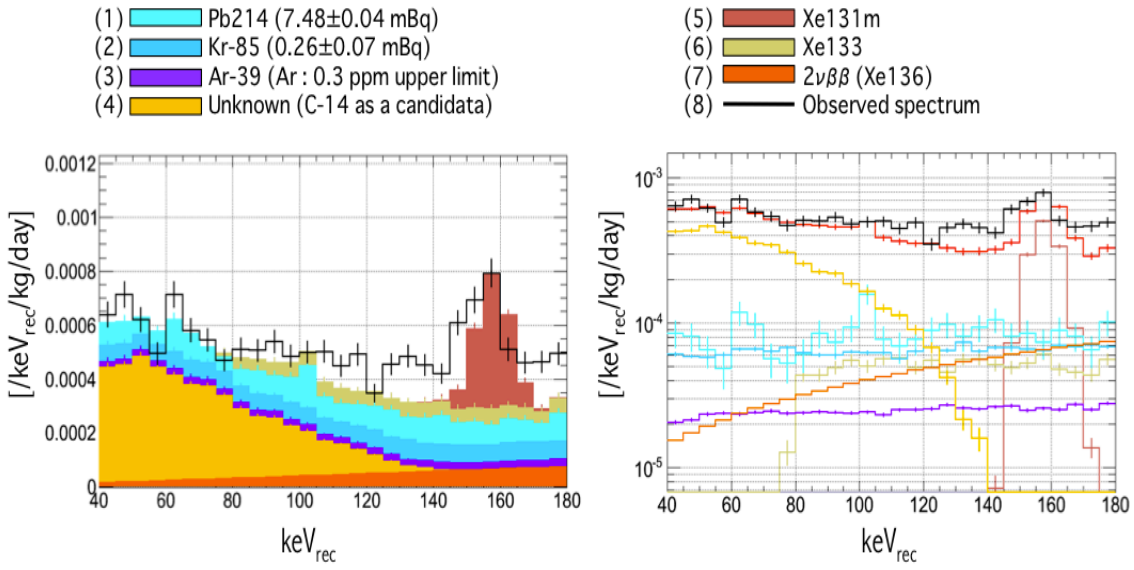

Figure 11.4: Energy spsctrum of the data and that expected from the BG MC.

Finally, we mention the possibilities for the future improvements of the sensitivity of the HPDM search. We evaluated that the main contribution of the BG components in the energy region between 40 keV$_{ee}$ and 140 keV$_{ee}$ came from the detector inner BGs. Our understanding of the BG components is progressing but not completed (The evidence of the contamination of ^{14}C, the origin of neutron BGs, and the remaining gaps between data and MC). For deeper understanding, we need to continue studies.

The finite value of the amount of ^{14}C contaminated in the liquid xenon can not be measured by our Gas Chromatography system due to their low concentration. Nonetheless, they might be reduced by an API getter (See Fig. 6.12) if the contamination or

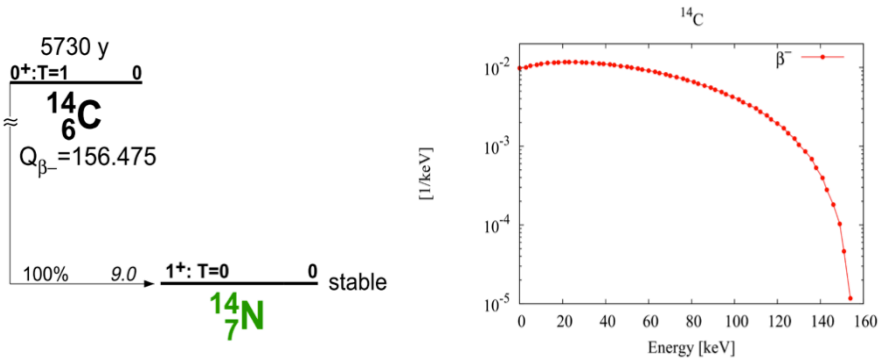

Figure 11.5: Decay scheme of ^{14}C (left) and β-ray spectrum of ^{14}C (right). The spectrum was adopted from [80].

diffusion happened after the previous gas circulation. We have a plan to temporarily stop the data taking and conduct gas circulation using the API getter. The contamination can be reduced down to 1 ppb level with the API getter.

We need to reduce the concentration of ^{222}Ra in the liquid xenon by one order of magnitude (< 1 μBq/kg) to achieve 10^{-5} /day/kg/keV$_{ee}$ BG level in the next phase of the XMASS project. The emanation through radon gas from the detector materials is the source of the contamination. We concluded that the emanation from a PMT quartz and an OFHC is low. However, the radon emanated from the outer detector materials, such as PMT basements and signal cables could diffuse into the active liquid xenon region of the detector through the gap between the PMTs and PMTs. In the next phase of the XMASS project, the main countermeasure is to select materials with low-emanation. We pursue the measurements of the radon emanation using an electrostatic collected radon detector. Additionally, the development of the improvement method of the sealability of the active volume against the outer part of the detector and the system to reduce the radon contamination in the gas xenon condition are under development.

Essentially, inner BGs can not be reduced by a fiducial volume cut. The difference between these BGs and HPDM signals is only the type of the particle; beta (electron) or gamma (photon). In the case of single phase liquid xenon scintillator, only pulse shapes of the events are discriminants of the particles. The decay constant of the scintillation light depends on the incident energy. By the difference of the elementary steps of the absorption between γ-ray and β-ray, they can have diferent decay constant. We have a possibility to perform the separation between the two particles in principle, if we understand the accurate energy dependences of the decay constant and keep the uncertainties at minimum. In contrast to the separation between nuclear recoil events and electron recoil events, the separation between gamma events and beta events is more challenging. The present understandings of the energy dependence of the decay constant in our detector can be found in [81]. This BG reduction method is a little bit challenging but interesting future possibility.

Chapter 12

Conclusion

We have searched for hidden-photon cold dark-matters (HPDMs) in the mass region between 50 keV$_{ee}$ and 120 keV$_{ee}$ using XMASS-I liquid xenon scintillation detector, which originally designed to search WIMP signals by nuclear recoils. The thermally produced hidden-photon dark matters (i.e. super-WIMPs) have been already rejected by the result of the XMASS commissioning phase. However, the possibilities of the HPDMs produced non-thermally are remained.

This study is the first results using the XMASS data after the detector refurbishment for this energy region. The enlargement of the fiducial volume from a 15-cm radius of the commissioning run to a 30-cm radius of this study allows us to search for HPDMs with large statistic and improve the sensitivity by using peak finding method. Since we can not find a HPDM signal for this energy region, we set an upper limit on the kinetic mixing at 90% confidence level. This limit is about two to three times better than the previous result by the data taken by the XMASS commissioning phase and the most stringent in the direct detection experiments in the world to date.

Reference

[1] http://www.esa.int/Our_Activities/Space_Science/Planck/Planck_reveals_an_almost_perfect_Universe

[2] K. Abe *et al.* (XMASS Collaboration) Phys. Rev. Lett. **113** (2014) 121301.

[3] Y. Suzuki, arXiv:hep-ph/0008296

[4] F. Zwicky. Helv. Phys. Acta **6** (1933) 110.

[5] Rubin, V. and Ford Jr., W.K. Astrophys. J. **159** (1970) 379.

[6] K.G. Begeman, A. H. Broeils and R.H. Sanders, MNRAS **249** (1991) 523.

[7] P. Ade, *et al.*, (Planck Collaboration), arXiv:1303.5076.

[8] R.P.Olling, MNRAS **311** (2000) 361.

[9] M. Kamionkowski and A. Kinkhabwala, Phys. Rev. D **57** (1998) 3256.

[10] R. Catena and P. Ullio, arXiv:0907.0018v2.

[11] F.S. Ling, E. Nezri, E. Athanassoul and R. Teyssier, J. of Cosmo. and Astropart. Phys. **02** (2010) 012.

[12] Chinese Physics C Vol. **38**, No. **9** (2014) 090001.

[13] C. Alcock *et al.* (MACHO Collaboration) Astrophys. J. **542** (2000) 257; (EROS Collaboration) AA **469** (2007) 387; (OGLE Collaboration) MNRAS **416** (2011) 2949.

[14] https://ned.ipac.caltech.edu/level5/Kolb/Kolb5_1.html

[15] DMTOOLS http://dmtools.brown.edu:8080/session/new

[16] R. Bernabei *et al.*, Eur. Phys. J. C **67** (2010) 39.

[17] Z. Ahmed, *et al.*, Phys. Rev. Lett. **106** (2011) 131302.

[18] R. Agnese *et al.* (SuperCDMS Collaboration) Phys. Rev. Lett. **112** no. 24 (2014) 241302

[19] P. Beltrame *et al.* (XENON Collaboration) arXiv:1305.2719

[20] J. Angle, *et al.*, Phys. Rev. Lett. **100** (2008) 021303.

[21] E. Aprile *et al.*, Phys. Rev. Lett. **109** (2012) 181301.

[22] D. S. Akerib *et al.*, arXiv:1310.8214.

[23] K. Abe *et al.* (XMASS Collaboration) Phys. Lett. B **719** (2013) 78-82.

[24] K. Abe *et al.* (XMASS Collaboration) Phys. Lett. B **724** (2013) 46-50.

[25] H. Uchida *et al.* (XMASS collaboration) Prog. Theor. Exp. Phys. (2014) 063C01.

[26] K. Abe *et al.* (XMASS Collaboration), arXiv:1510.00754.

[27] R.D. Peccei and H. Quinn, Phys. Rev. Lett. **38** (1977) 1440, Phys. Rev.D **16** (1977) 1791.

[28] Astalos *et al.*, Phys. Rev. D **69** (2004) 011101.

[29] P. Sikivie Phys. Rev. Lett. **51** (1983) 1415.

[30] S. Andriamonje *et al.*, JCAP **04** (2007) 010.

[31] Y.Inoue *et al.*, Phys. Lett. B **68** (2008) 93.

[32] arXiv:1310.8642v1 [hep-ph].

[33] Y. Hochberg *et al.* Phys. Rev. Lett. **115** (2015) 021301.

[34] L. B. Okun, Sov. Phys. JETP **56** (1982) 502 [Zh. Eksp. Teor. Fiz. **83** (1982) 892].

[35] B. Holdom, Phys. Lett. B **166** (1986) 196.

[36] R.Andreas Phys.Dark Univ. **1** (2012) 116.

[37] R. Bähre, B. Döbrich, J. Dreyling-Eschweiler, S. Ghazaryan, R. Hodajerdi, D. Horns, F. Januschek and E. -A. Knabbe et al., JINST **1309** (2013) T09001.

[38] J. Redondo JCAP **0807** (2008) 008.

[39] Mizumoto, T. *et al.* JCAP **1307** (2013) 013.

[40] Horns, J. Jaeckel, A. Lindner, A. Lobanov, J. Redondo, and A. Ringwald, JCAP **04** (2013) 016.

[41] Suzuki, J. *et al.* JCAP **1509** (2015) 09, 042.

[42] M. Pospelov, A. Ritz and M. B. Voloshin, Phys. Rev. D **78** (2008) 115012.

[43] J. Redondo, M. Postma, J. Cosm. Astropart. Phys. **02** (2009) 005.

[44] K.MarkovičandM.Viel, Pub.Astron.Soc.Aust.31, e006(2014).

[45] R.Horvat, D.Kekez, M.Krčmar, Z.Krečak, andA.Ljubičić, Phys.Lett.B721, 220(2013).

[46] J. Preskill, M. B. Wise and F. Wilczek, Phys. Lett. B **120** (1983) 127.

[47] L. F. Abbott and P. Sikivie, Phys. Lett. B **120** (1983) 133.

[48] A. E. Nelson and J. Scholtz, Phys. Rev. D **84** (2011) 103501.

[49] P, Arias *et al*. JCAP **1206** (2012) 013.

[50] Jaeckel, J Frascati Phys.Ser. **56** (2012) 172.

[51] An, Haipeng *et al*. Phys.Lett. B **747** (2015) 331.

[52] XCOM: Photon Cross Sections Database http://www.nist.gov/pml/data/xcom/index.cfm

[53] Y. Fukuda et. al. (Super-Kamiokande Collaboration), Nucl. Instr. Meth. A **501** (2003) 418.

[54] K. Ueshima, 2010, "Study of pulse shape discrimination and low back-ground techniques for liquid xenon dark matter detectors", PhD dissertation, University of Tokyo, Japan.

[55] K. Abe *et al*., (XMASS Collaboration), Nucl. Instr. Meth. A **716** (2013) 78.

[56] A. C. Hollis Hallett, in Argon, Helium and the Rare Gases, Ed. G.A. Cook (Interscience Publishers, New York, 1961), pp. 322-335.

[57] National Institute of Standards and Technology, http://www.nist.gov/srd/nist12.html

[58] Handbook of Chemistry & Physics, The Chemical Rubber Company.

[59] A. C. Sinnock and B. L. Smith Phys. Rev. **181** (1969) 1297.

[60] S. Eidelman *et al*., (Particle Data Group), Phy. Lett. B **592** (2004) 1.

[61] S. Nakamura KEK workshop " Radiation detector and its application " (2004).

[62] MEG proposal to PSI, Proposal to INFN, http://meg.web.psi.ch/docs/index.html

[63] E. Aprile and T. Doke. Liquid xenon detectors for particle physics and astrophysics. Rev. Mod. Phys. **82** (2010) 2053.

[64] A. Baldini *et al*., IEEE Trans. Dielectr. Electr. Insul. **13** (2006) 547.

[65] S. Kubota, M. Hishida, M. Suzuki, and J. Z. Ruan. Dynamical behavior of free electrons in the recombination process in liquid argon, krypton, and xenon.Phys. Rev. B **20** (1979) 3486.

[66] I.Onsager, Phys.Rev. **54** (1938) 554.

[67] T.Doke, *et al*., J.Appl.Phys **41** (2002) 1538.

[68] A.Hitachi and T. Takahashi, Phys.Rev.B **27** (1983) 5279.

[69] M.Jeremy *et al*. JINST **9** (2014) T04002.

[70] S. Agostinelli *et al*., Nucl. Instr. Meth. A **506** (2003) 250.

[71] K. Amako *et al.*, IEEE Trans. Nucl. Sci. **53** (2006) 270.

[72] N. Y. Kim *et al.*, Nucl. Instr. Meth. A **784** (2015) 499.

[73] D.C.Malling, 2013, "Measurement and Analysis of WIMP Detection Backgrounds, and Characterization and Performance of the Large Underground Xenon Dark Matter Search Experiment", PhD dissertation, Brown University.

[74] The Super-Kamiokande Collaboration, Phys. Lett. **452** (1999) 418.

[75] Abe K. *et al.*, (XMASS Collaboration) J. Phys. Conf. Ser. **120** (2008) 042022.

[76] 日本アイソトープ協会 (編)：アイソトープ手帳、丸善 (2002).

[77] A. Gando *et al.* (KAMLAND-ZEN collaboration) Phys. Rev. C **85** (2012) 045504.

[78] K. Abe *et al.* (XMASS collaboration), arXiv:1511.04807.

[79] A. Minamino Master thesis (2004).

[80] Aleksankin V.G. *et al.* Handbook, "Beta and Antineutrino Radiation of Radioactive Nuclei" Edited by Rubzov P.M., Moscow, Energoatomizdat, (1989) ISBN5-283-03727-4.

[81] H.Takiya *et al.* (XMASS Collaboration), arXiv:1604.01503.